

---

---

# Consolidating Gauge, Weather Radar and GPM DPR Level 2A Observations of High-intensity Rainfall Events in the Netherlands

---

---

By Liselotte Wisman

To obtain the degree of Master of Science at Delft University of Technology

Thesis committee:

Prof. dr. ir. Nick van de Giesen TU Delft, chair

Prof. dr. ir. Remko Uijlenhoet TU Delft

Dr. Marc Schleiss TU Delft

July 7<sup>th</sup> 2022

Delft University of Technology, Faculty of Civil Engineering and Geosciences  
Stevinweg 1, 2628 CN Delft, The Netherlands

# Contents

<b>Preface</b>	<b>3</b>
<b>List of Acronyms</b>	<b>4</b>
<b>Abstract</b>	<b>5</b>
<b>1 Introduction</b>	<b>6</b>
1.1 Relevance . . . . .	6
1.1.1 Societal Relevance . . . . .	6
1.1.2 Scientific Relevance . . . . .	6
1.2 Precipitation Estimation Challenges . . . . .	7
1.3 Research Problem . . . . .	8
1.4 Research Objective . . . . .	9
1.5 Research Questions . . . . .	9
1.6 Thesis Outline . . . . .	9
<b>2 Theoretical Background</b>	<b>10</b>
2.1 Precipitation . . . . .	10
2.1.1 Dynamics . . . . .	10
2.1.2 Precipitation Types . . . . .	10
2.2 Precipitation Measuring Techniques . . . . .	11
2.2.1 Electronic Rain Gauge . . . . .	11
2.2.2 Radar . . . . .	12
<b>3 Literature Study</b>	<b>16</b>
3.1 Comparing Precipitation Estimates . . . . .	16
3.1.1 Challenges . . . . .	16
3.1.2 State-of-the-art . . . . .	16
3.2 Small-scale spatial rainfall variability . . . . .	17
3.2.1 Magnitude of variability . . . . .	18
3.2.2 Factors affecting spatial variability . . . . .	19
<b>4 Data</b>	<b>20</b>
4.1 Study Area . . . . .	20
4.1.1 Requirements . . . . .	20
4.1.2 Area description . . . . .	20
4.2 Data Acquisition . . . . .	20
4.2.1 KNMI Automatic Gauge Network . . . . .	21
4.2.2 KNMI C-band Weather Radar Network . . . . .	21
4.2.3 GPM Dual-frequency Precipitation Radar . . . . .	22
4.2.4 Wind Data . . . . .	23
4.3 Data Selection . . . . .	23
<b>5 Methodology</b>	<b>25</b>
5.1 Software . . . . .	25
5.2 Data Processing . . . . .	25
5.2.1 Pre-processing . . . . .	25
5.2.2 Filtering HI-Precipitation Data . . . . .	27
5.2.3 Coupling WR and DPR . . . . .	28
5.3 Data Comparisons . . . . .	29

5.3.1	Gauge and Radar Relations . . . . .	29
5.3.2	Reflectivity Relations . . . . .	31
<b>6</b>	<b>Assessing Coupled Observations</b>	<b>34</b>
6.1	Metrics . . . . .	34
6.2	Comparison Gauge and Radar Observations . . . . .	34
6.2.1	Visual Analysis Events . . . . .	34
6.2.2	Wind Speed Influence . . . . .	38
6.3	Reflectivity Relations . . . . .	40
6.3.1	Direct Reflectivity Comparisons . . . . .	40
6.3.2	Deviations . . . . .	41
6.3.3	Correlations . . . . .	45
<b>7</b>	<b>Discussion</b>	<b>47</b>
7.1	Gauge and DPR Relations . . . . .	47
7.1.1	Deviating Observations . . . . .	48
7.2	WR and DPR Relations . . . . .	49
7.2.1	Deviating Observations . . . . .	50
7.3	Reflection . . . . .	51
<b>8</b>	<b>Conclusions and Recommendations</b>	<b>52</b>
8.1	Key Findings . . . . .	52
8.2	Limitations . . . . .	53
8.3	Outlook . . . . .	53
8.4	Future Research . . . . .	53
	<b>Bibliography</b>	<b>54</b>
<b>A</b>	<b>Data Details</b>	<b>56</b>
<b>B</b>	<b>Case Study Data</b>	<b>59</b>
<b>C</b>	<b>Figures Quantitative Analysis</b>	<b>104</b>

## Preface

This research was conducted as the final part to obtain my Master of Science degree in Civil Engineering at Delft University of Technology, with a specialization in Water Management and Environmental Engineering. My interest in this field of study arose during my six months abroad in Stellenbosch, South-Africa, where I studied courses related to hydrology and atmospheric processes. This resulted in my leaving the field focused on processes that occur under the surface, which I covered intensely during my BSc. in Applied Earth Sciences, for the field that studies all that occurs above it. Although probably hard to believe, my time in Stellenbosch didn't just focus on my studies: along with my interest in water and the environment, came my love for Africa. As my mother spent most of her childhood in Kenya, I grew up with enchanting stories that sparked my interest for the African landscape and cultures. Giraffes in the garden and eating cow tongue for dinner: naturally, this all sounded quite surreal to a borne-and-bred Dutch girl who was already excited when a dog happened to walk by or agitated when Brussels sprouts arrived at the dinner table. Growing up with Africa and having lived there for several months, resulted in the logical next step of wanting to focus my MSc. thesis on Africa.

Naturally, this led me to Nick van de Giesen, who was notorious at the TU Delft for his interests and projects in Africa, and presented me the opportunity to do research in Ghana for my MSc thesis and subsequently became the chairman of my thesis committee. Eventually, I didn't end up going to Ghana, due to our friend Covid-19 outstaying its welcome, and the initial project thus had to be reshaped. I would like to thank Nick for thinking along with me to try and find another, suitable project to finalize my studies at the TU Delft and for providing guidance throughout the length of my research period. I've really enjoyed our chats, which fortunately could take place face to face during the final months of my research. Furthermore, I'd like to express my gratitude to the other two members of my thesis committee, Remko Uijlenhoet and Marc Schleiss, for all the time and effort you've put in giving tips and feedback on my project. Also, I'd like to thank Pierre Kirstetter and Linda Bogerd, who were so kind to virtually meet with me and provide their own insights on improving my project.

Lastly, I would like to say thanks to the people close to me for always supporting me throughout the entire 7 years of my studies at the TU Delft, and especially during the last eight months. To my dear family, for always believing that everything would work out just right, even when I believed it wouldn't (even though you probably had no idea what I was talking about exactly). For providing a safe haven to run home to, when I needed it the most, and for having given me the opportunity and time to both fail and thrive during my entire life. And thank you to my partner and long time study buddy, Wytse Petrie, for supporting me through the ups and downs of this project and for always being so interested in everything that I do.

*By Liselotte Wisman  
The Hague, July 2022*

## List of Acronyms

<b>DPR</b>	Dual-frequency Precipitation Radar
<b>G</b>	electronic rain gauge
<b>GPM</b>	Global Precipitation Measurement mission
<b>HI</b>	high intensity, indicating precipitation intensity $\geq 15$ mm/h
<b>HR</b>	high reflectivity, indicating reflectivity factor values $\geq 35$ dB
<b>IFOV</b>	Instantaneous Field Of View, in this study referring to the centre of a radar footprint
<b>WR</b>	weather radar
<b>WS</b>	weather station

## Abstract

The Dual-Frequency Precipitation Radar on board the Global Precipitation Measurement (GPM) mission core satellite has been providing precipitation products across the globe for over 6 years, thereby even supplying precipitation estimates for areas on Earth where surface-based precipitation measurements are not possible, like in remote regions, as well as seas and oceans. In this study, the GPM DPR Ku-band Level 2A instantaneous observations are compared with continuous measurements from a surface network in the Netherlands for high-intensity precipitation events during summer months. The aim of the research is to gain more insights in the temporal and spatial correspondence of the DPR's measurements with precipitation occurring on the surface. The surface network consists of 2 C-band weather radars and an automatic gauge network of 33 gauges (approximately 50 km apart). Radar reflectivity factor is one of the prime parameters used for precipitation retrievals from radars and is thus the parameter used for analysis of both the DPR and the weather radar network. Precipitation intensity is the parameter retrieved from the automatic gauge network. Space-borne and surface measurements have varying characteristics, for instance in spatial and temporal resolution, and thus many challenges arise to perform an accurate and qualitative comparison. In this research, data is funneled by selecting high-intensity gauge data with a threshold of 15 mm/h within 40 minutes from GPM scan time within a 2.5 km range from the nearest DPR footprint. Ultimately, 26 high-intensity gauge measurements spread over 18 dates were used in the comparison analyses, selected out of data ranging from May - October for the years 2018 - 2021. The analyses showed that DPR and WR data correspond best in time (average correlation of 0.785) when DPR scantime is within 3 minutes of WR scantime. Also, results showed that instantaneous DPR data can be related to high-intensity gauge observations within a 40 minute time range by use of wind direction and wind speed. Furthermore, it was observed that precipitation performance of DPR is found satisfactory for intensity  $\geq 0.5$  mm/h (POD between 0.7 - 0.9 based on distance WS-IFOV), but unsatisfactory for intensities  $\geq 15$  mm/h (POD of 0.18 - 0.25). The results imply that DPR measurements don't have an obvious temporal and spatial lag with respect to the observations made from the surface and thus form a prospect for global usage, if more follow-up research is conducted.

# 1 Introduction

In this chapter, the relevance of this study will be explained, the research problem and objective will be discussed and the study's research questions will be presented. Lastly, the outline of the thesis will be presented.

## 1.1 Relevance

The relevance of this research, from both a societal and scientific perspective, will be discussed below.

### 1.1.1 Societal Relevance

Due to the strong effects of precipitation on human welfare, the interest in this phenomenon dates to several centuries ago. These effects are known to be both positive and negative: positive being that the occurrence of precipitation supplies the Earth with fresh water, but the negative being that extreme variations in its occurrence can cause natural disasters, like droughts or flooding. These extreme variations have shown to be increasing in the near past and are predicted to keep increasing in the future, as the frequency and intensity of heavy precipitation events and the occurrence of droughts are expected to become more frequent due to the effects of climate change (IPCC, 2021). Accurate precipitation measurements are crucial for society, as inaccurate measurements and forecasts can damage agriculture, infrastructure, livestock and even human lives (Beek, 2013). Surface rainfall observations can for instance be used as input variables for weather and climate research. Vital examples of such research are flood and drought monitoring and agricultural water management (Coz and van de Giesen, 2020). Also, precipitation data have played, and still play, an important role in modelling and determining climate change (IPCC, 2021).

To improve the resilience against the predicted changes in precipitation patterns, it is now even more important than ever to have accurate information on surface rainfall, and in particular on severe surface rainfall (of possibly convective nature). Convective rainstorms are characterized by short-lived and intense rainfall cells, which are localized in time and space (Coz and van de Giesen, 2020). These high-intensity storms can be highly variable in both the temporal and spatial domain and are expected to fluctuate even more in the future due to the effects of global warming. The varying character of these storms can cause great damages, for instance, due to sudden local high-intensity events which increase runoff and the chance of flood events. Or, for example, due to local rainfall deficits caused by the spatially variable nature of convective storms, which could damage crop yield in regions that are dependent on rain-fed agriculture (Coz and van de Giesen, 2020). If rainfall information were to improve, this will aid regions that are most vulnerable to the effects of current rainfall extremes and future predictions.

### 1.1.2 Scientific Relevance

Although the process of precipitation is one of the most studied subjects in both hydrology and meteorology, the estimation of precipitation on the surface is still one of the biggest challenges in both scientific fields. Multiple factors are to blame, among which are the spatiotemporal variability of precipitation, its intermittent nature and its sensitivity to meteorological conditions (Sokol et al., 2021). The oldest, most direct, and widely used technique to measure precipitation is by use of rain gauges. However, rain-gauge networks are sparse and the ones that are continuously operating are estimated to have a combined funnel surface area of no more than 3000 m<sup>2</sup> globally (Kidd et al., 2017), which is negligible compared to the size of the Earth's surface (namely, nearly a factor 10<sup>11</sup> larger). As a single gauge measures rainfall in-situ at a

specific location point, its observations are representative for local circumstances and not areal quantities (Gabella et al., 2017). The highly spatial variability of rainfall thus is hard to capture by a gauge network, especially in case of convective rainfall, as there are simply not enough observations to describe the variability of a specific field. Remote sensing techniques form a possible solution for this issue.

During the last few decades, attempts have been made to accurately measure precipitation using satellites. Satellite measurements are based on remote sensing techniques and don't have the ability to measure precipitation directly, like rain gauges do. However, contrarily to rain gauges, they have the advantage of being able to cover the Earth globally, instead of being restricted to the centimetre-scale like the in-situ measurements by rain gauges are (Coz and van de Giesen, 2020). Remote sensing techniques are especially valuable in regions with localized, high-intensity storm events of convective nature and sparse gauge networks, that are not dense enough to accurately measure the highly variable behaviour of such events (Coz et al., 2021). Until date, it has been shown that precipitation estimates from space-borne remote sensing devices do not naturally agree with the measurements made at the surface and thus cannot be used as a direct representative of the precipitation that occurs at the ground (Gabella et al., 2017). This is the result of multiple factors, such as differences in measurement method and altitude, but also has to do with human-based choices, such as the ones implemented in precipitation estimation algorithms applied to remotely sensed data. An increased understanding of the relationship between space-borne and surface precipitation techniques and their subsequent estimates would improve the potential of using satellite observations globally to determine the precipitation that occurs on the surface.

## 1.2 Precipitation Estimation Challenges

Precipitation is highly variable in both space and time, which creates many difficulties for measuring the phenomenon. There are many instruments that produce rainfall estimates and all have their own sources of error and uncertainty. As mentioned in the previous section, the rain gauge is the oldest and most basic method to measure precipitation at a small scale. As it directly measures precipitation at the surface, gauge observations can be considered as accurate point measurements of precipitation (Beek, 2013). The performance of the instrument is highly dependable on its location, as high objects like buildings and trees can affect the measurement. Furthermore, wind can affect the accuracy of the measurement. Errors also arise due to human-induced errors, such as the influence related to calibration errors.

Weather radars have been in use for meteorological activities since World War II. Weather radars produce precipitation measurements over large areas, thereby providing more insights into the space-time variability over a large scale. Ultimately, a precipitation estimate is derived from the signal received by the radar and the product is thus an indirect representation of the actual rainfall. Many sources of error exist that usually lead to underestimation of precipitation, such as influence of attenuation (along the radar beam in case of extreme precipitation or when precipitation hits the radome) and of clutter (when the radar's signal encounters non-meteorological objects, such as birds or buildings) (Beek, 2013). Another problem affecting the accuracy of weather radar results is the phenomenon of overshooting. Overshooting occurs at longer distances from the radar, when, due to the curvature of the Earth, the lowest scan angle of the radar is at a height above precipitation such that the precipitation below is not measured (Beek, 2013). Furthermore, it should be taken into account that the precipitation estimate is of indirect nature, and thus prone to human-induced errors. Also, the estimate is representative of surface precipitation, whereas the actual measurement is made at higher altitude.

Measurements by space-borne radars such as the DPR are valuable for gaining rainfall information on a quasi-global scale. Like weather radars, space-borne radars employ remote sensing techniques and thus estimate precipitation in an indirect manner. The measurements are made at an altitude of several hundreds of kilometers and produce precipitation products for different altitudes. Possible inaccuracies and errors in these products arise from attenuation in the vertical dimension. Again, attenuation can be caused by precipitation, but also by interference of the signal with clouds and atmospheric gases (also known as hydrometeor attenuation, which is especially of influence for deep convective clouds (Battaglia et al., 2020)). Another source of error for surface precipitation determination is the influence of clutter from the surface on the measurement. Furthermore, limitations for complete rainfall information by space-borne radar is the temporal and spatial resolution. The spatial resolution is relatively coarse, in the kilometer-scale, and thus cannot be used for identifying small-scale rainfall variability. Furthermore, a satellite such as the GPM-Co makes global overpasses at a daily frequency, and thus provides one instantaneous measurement for each specific location (approximately) once a day. Due to this low temporal resolution, the behaviour of precipitation events cannot be captured adequately.

### 1.3 Research Problem

High-intensity precipitation events can vary enormously on a small temporal and small spatial scale. Due to their highly dynamic nature, it has been found that precipitation intensities can vary within hundreds of meters and can initiate and dissipate within minutes from a certain location ((Syed et al., 2003), (Krajewski et al., 2003), (Peleg et al., 2013), (Fiener and Auerswald, 2009)). Therefore, the behaviour as captured by a specific rain gauge may vary already within a few hundred meters, let alone kilometers. Space-borne observations form a possible solution for this problem and a prospect for rainfall measurements all over the world, especially in regions where surface measurements are limited, as they provide quasi-global rainfall information at a relatively high temporal and spatial resolution. However, previous inter-comparison research has shown that satellite observations do not always correspond well with observations from the surface ((Gabella et al., 2017), (Kidd et al., 2017), (Lasser and Foelsche, 2018), (Petracca et al., 2018)). All precipitation products have different characteristics, such as spatial and temporal resolution or varying parameters, and are therefore difficult to compare directly with one another. Therefore, it still provides a challenge to credit one precipitation estimate as better with respect to another precipitation estimate, despite the large amount of precipitation-related products that are available (Kidd et al., 2017). To ultimately be able to use space-borne observations as "true" precipitation estimates, more insights have to be gained on how satellite measurements relate to the precipitation that is observed at the surface. Most research up until now has been based on processed satellite products (like precipitation intensity products), which are the result of the incorporation of multiple assumptions and choices in the processing algorithm. By making use of rawer products, such as the effective reflectivity factor, a more direct understanding can be gained on characteristics of space-borne observations of rainfall through comparison with surface measurements from weather radar and rain gauges.

## 1.4 Research Objective

The objective of this research is to obtain more insights of how reflectivity observations from the Dual-frequency Precipitation Radar of the GPM mission relate to measurements retrieved at the surface, namely from an automatic electronic gauge network and a weather radar network. The main focus will be on analyzing reflectivity estimates from instantaneous DPR observations with respect to temporally corresponding precipitation estimates from gauges and weather radar, in both time and space. Furthermore, the aim of the research is to study how such DPR observations can be linked to high-intensity precipitation occurring at the surface, while taking into account factors like wind and the dynamic nature of severe precipitation storm systems. Weather radar reflectivity measurements will also be used to support these findings.

## 1.5 Research Questions

The objective of this research will be met by answering the following research question:

*How do rainfall estimates from the GPM Dual-frequency Precipitation Radar relate to estimates from rain gauges and weather radar for high-intensity rainfall events?*

The following sub-questions will be answered to substantiate the research question:

- i. *How do instantaneous DPR reflectivity products relate to surface reflectivity products by weather radars in time and space?*
- ii. *What are the temporal and spatial scales for which a relation can be expected between DPR estimates and surface measurements by weather radar?*
- iii. *How do instantaneous DPR precipitation and reflectivity products relate to surface precipitation measurements by rain gauges in time and space?*
- iv. *What are the temporal and spatial scales for which a relation can be expected between DPR estimates and surface measurements by gauges?*

## 1.6 Thesis Outline

The structure of this paper is as follows. First, in chapter 2, information will be given on the dynamics of precipitation and on the different types of precipitation measurement techniques used in this study. Next, chapter 3 will discuss literature related to the focus of this study, as well as prior research within the scope of this study. Chapter 4.2 will describe the case study area and provide information on the data. In chapter 5, the methods of this research will be discussed, of which the results will be given in chapter 6. Subsequently, the results will be analyzed and discussed in chapter 7. Lastly, conclusions and recommendations for further research will be given in chapter 8. Appendices are attached at the end of this thesis, to provide further information and illustrations.

## 2 Theoretical Background

The theoretical background required to grasp the main concepts of this study will be given in this chapter, with a focus on precipitation dynamics in section 2.1 and in 2.2 on the three different precipitation estimation techniques that were used in this study.

### 2.1 Precipitation

Below, the dynamics of precipitation will be discussed as well as a description of the two main different precipitation types.

#### 2.1.1 Dynamics

As stated by the KNMI: *"Precipitation is defined as the liquid or solid product of condensation or sublimation of water vapour that falls down out of clouds or groups of clouds and reaches the earth's surface"* (KNMI, 2000). As the definition entails, before precipitation can occur, clouds have to be present. Most clouds occur in the troposphere, which is the lowest layer of the atmosphere and contains nearly all water particles of the atmosphere (Houze, 2014). In the troposphere, the mean temperature decreases with height. Thus, when air rises from the surface, temperature decreases and the water particles present in the rising air column condense to ultimately form liquid water droplets or ice particles. Actual cloud droplets are formed by a process called heterogeneous nucleation. In this process, water molecules collect onto the surface of small aerosol particles (referred to as cloud condensation nuclei (CCN) in this process), which are abundantly present in the atmosphere. As such, water molecules go from a less ordered to a more ordered state. Once droplets are formed, they continue to grow as more water vapour diffuses towards them (Houze, 2014). Until they reach a size of about 50 to several 100's of micrometres in diameter and small precipitation particles are formed, the growth continues. Their growth continues until they form precipitation particles, which can range from about 50 to a few 100 micrometres (drizzle) up to a few 1000 micrometres (raindrops) in diameter. When particles of such sizes are formed, they start to fall down towards the surface due to a downward gravitational force. As such, the precipitation process occurs, as the definition above implied. The final speed of raindrops is called the terminal fall speed and is a function of the raindrop's radius.

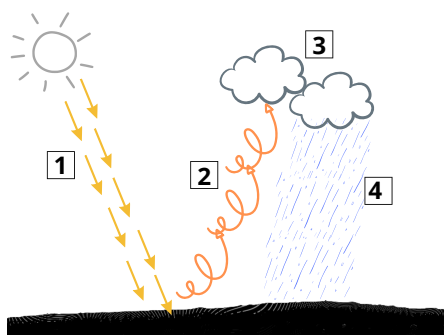


Figure 1: Schematic of convective rainfall process

#### 2.1.2 Precipitation Types

Precipitation can be subdivided into two types: convective and stratiform. Stratiform rainfall is relatively continuous and uniform in intensity and shows little vertical development. Convective rainfall, on the other hand, shows great vertical development and is caused by unequal heating of

the Earth's surface by the Sun (see figure 1, indicated by step 1). The heated air, warmer than its cooler surroundings, naturally starts to rise (step 2 figure 1) and, when the condensation point is reached, condensation occurs and large cumulus or cumulonimbus clouds are formed (step 3 figure 1). As this process continues, the condensed particles grow in size and will eventually precipitate (step 4 figure 1). Convective precipitation occurs as high-intensity showers over certain areas for a short amount of time, as the rise of heated air causing the unstable conditions occurs very locally and thus limits the extent of the convective system. The process is displayed schematically in figure 1.

## 2.2 Precipitation Measuring Techniques

Rain gauge, C-band weather radar and GPM Dual-frequency Precipitation Radar data are used in this research. Below in figure 2, a schematic is shown displaying the varying geometries in a simplified manner (not true to size) of the different precipitation estimation techniques. Each technique and its characteristics will be discussed in the following sections.

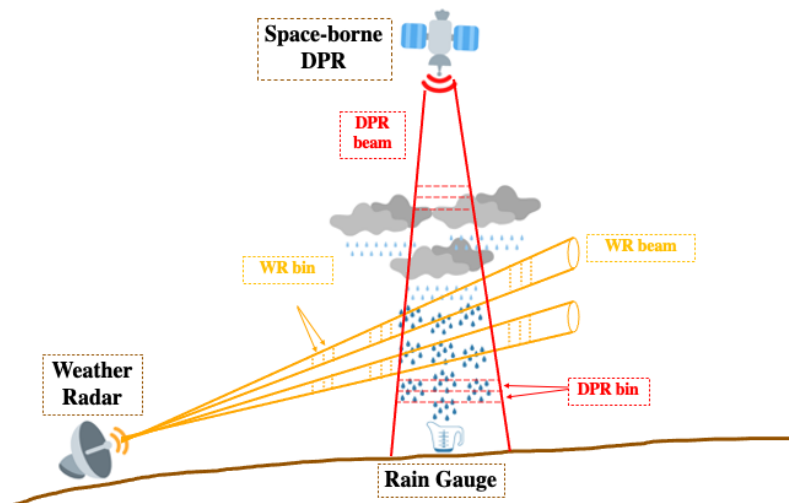


Figure 2: Schematic displaying the different geometries of weather radar, DPR and gauges

### 2.2.1 Electronic Rain Gauge

In this research, precipitation intensity data is used that's provided by the automatic weather station from the Koninklijk Nederlands Meteorologisch Instituut (KNMI). The weather stations register precipitation by use of an electronic rain gauge system, consisting of o.a. a funnel (A), a float (D) in a measuring container (C) and a potentiometer (B) (see figure 3a). Nowadays, most KNMI rain gauges are situated in an Ott screen, which has a height and diameter of ca. 1 meter (as pictured in figure 3b) (Brandsma, 2014).

The rainfall detection principle is based on the measure of the displacement of a float placed in the measuring cell where the precipitation is collected (KNMI, 2000). When temperatures are below 4 °, the funnel and reservoir are heated in order to melt solid precipitation (Brandsma, 2014). When precipitation occurs, the raindrops will first travel through a funnel, before reaching the measuring cell. The arrival of raindrops will displace the floater, and the difference in the position of the floater at the start and end of each averaging period ultimately determines the precipitation intensity. The potentiometer registers each second whether there is precipitation falling or not and hence determines the precipitation duration. It's equipped with a heating element that dries the detection electrodes to be dry again within 1 second, such that newly

incoming precipitation can be detected accurately. The activation threshold of the precipitation detector is 0.02 mm/h.

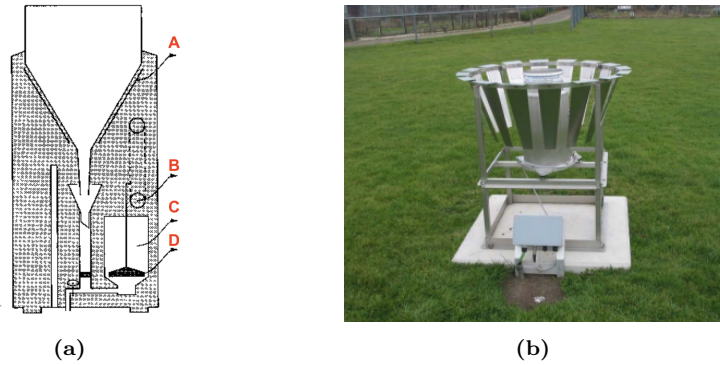
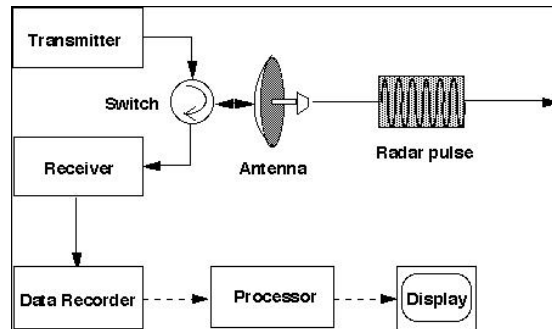


**Figure 3:** Automatic rain gauge used by the KNMI displayed in a schematic (left, by (KNMI, 2000)) and pictured in an Ott screen (right, (Brandsma, 2014))

The gauge averaging period is 12 seconds (i.e.  $1/12$  Hz), hence every 12 seconds the measuring cell is emptied and the average precipitation intensity over those 12 seconds is registered by dividing the amount of precipitation by 12 seconds (KNMI, 2000). By taking the arithmetic mean of the precipitation intensity values over the last fifty 12-second samples, the average precipitation intensity over the last 10 minutes is registered in the KNMI database in units of mm/h at the end of those respective 10 minutes (i.e. the average precipitation intensity registered from 00:00 UTC to 00:10 UTC is registered at 00:10 UTC). The measurement range is 0 - 0.7 mm per 12 seconds.

### 2.2.2 Radar

Remote sensors are instruments that measure electromagnetic radiation emitted by objects and use that measurement to determine the characteristics and location of that particular object. Two types of remote sensors are used in precipitation research, namely passive and active sensors. The former's principle is based on detecting radiation naturally emitted or scattered by hydrometeors. Active sensors, of which the most common type is the radar, operate in the microwave part of the electromagnetic spectrum. The basic components of a precipitation radar are a transmitter, a receiver, an antenna and a radar processor, as displayed schematically in figure 4a below.



(a) Schematic of radar instrumental details (University of Texas Institute for Geophysics, 2022)

The transmitter's function is to create electromagnetic signals in rapidly sequenced pulses at the speed of light (Houze, 2014), which are sent out by the antenna. When a particle is encountered in the path of the beam, the signal is reflected back towards the antenna, where it is detected and magnified by the receiver of the radar. The radar processor then gathers and analyzes the received data. The time in between the transmitted and received signal is recorded and used to determine the exact distance (i.e. range  $r$ ) from the radar to the target. After the reflected signal (known as the average returned power  $\bar{P}_r$ , which is the average of a few dozen pulses) is received back by the radar, the signal can be converted to physical quantities. The signal reflected back from the target towards the radar's receiver is the average returned power, as depicted in the radar equation by Battan (1973):

$$\bar{P}_r = \frac{P_t G^2 \lambda^2 \theta_H \theta_V \tau_p c_o \eta_r}{512 (2 \ln 2) \pi^2 r^2} \quad (1)$$

, where  $P_t$  is the transmitted power,  $G$  the antenna gain,  $\tau_p$  the duration of the emitted radar pulse,  $c_o$  the speed of light,  $\theta_H$  and  $\theta_V$  the horizontal and vertical beamwidth angles, respectively,  $\eta_r$  is the radar reflectivity per unit volume of air and  $\lambda$  is the wavelength. The wavelength of the transmitted signal is of importance, as the magnitude of the returned signal depends on the wavelength and the size of the droplets (Beek, 2013). Longer wavelengths (larger than 5 centimetres, such as C-band) are less influenced by attenuation and are therefore generally used for large-scale rainfall monitoring (Beek, 2013).  $\eta_r$  represents the sum of the scattering cross-sections of all particles reflecting the signal back within the resolution volume and is thus represented by:

$$\eta_r = \sum \sigma_\lambda \quad (2)$$

, where the backscatter cross-section of a certain particle at radar wavelength  $\lambda$  is indicated by  $\sigma$ . For Rayleigh scattering, the scattering cross-section for a single particle of diameter  $D$  is equal to:

$$\sigma_\lambda = \pi^5 |K|^2 D^6 \lambda^{-4} \quad (3)$$

By substituting equation (2) and (3) in equation (1), a formula for the radar reflectivity factor  $Z$  is derived:

$$Z \equiv \frac{1}{V_{res}} \sum D^6 = \frac{r^2 \bar{P}_r C_R}{|K|^2} \quad (4)$$

, where  $C_r$  is the radar constant given by equation (5) and combines all constants for the system as follows:

$$C_R = \frac{64 \lambda^2 r^2}{P_t G^2 \pi^2 V_{res}} \quad (5)$$

, where  $V_{res}$  is the resolution volume, which is the volume containing the radar's target particles and determined by the beamwidth and duration of the transmitted radar pulse and can be rewritten to:

$$V_{res} = \pi \theta_H \theta_V \left(\frac{r}{2}\right)^2 \frac{c_o \tau_p}{2} \quad (6)$$

Due to the composition of scattered particles normally not being known with certainty, radar data is often expressed as  $Z_e$  (in units of  $mm^6 m^{-3}$ , indicating the particle size to the sixth power per unit volume of air). The equivalent radar reflectivity factor  $Z_e$  is representative of the reflectivity factor that particles would have if they consisted purely of liquid water (Houze, 2014). In table 1, an overview of expected reflectivity values for certain precipitation types is shown. Often,  $Z_e$  values are expressed in decibel units with respect to  $mm^6 m^{-3}$ :

$$dBZ_e \equiv 10 \log_{10} Z_e \quad (7)$$

This research makes use of reflectivity products of two types of active remote sensors, namely the KNMI weather radar and the GPM Dual-frequency Precipitation Radar. The specific properties of each instrument will be discussed below in sections 2.2.2.1 and 2.2.2.2, respectively.

Reflectivity Factor	Particle Type
-50 to 0 dBZ	Nonprecipitating cloud Marginally detectable precipitation
0 to 10 dBZ	Drizzle Very light rain Light Snow
10 to 30 dBZ	Moderate rain Heavier snow
30 to 45 dBZ	Melting snow
30 to 60 dBZ	Moderate to heavy rain
60 to > 70 dBZ	Hail

**Table 1:** Reflectivity factor representative for different types of precipitation (Houze, 2014)

### 2.2.2.1 KNMI Weather Radar

The KNMI operates two identical C-band 5.6 GHz Doppler weather radars, produced by Gematronik. Currently, the radars are located in Den Helder (51.8369 N, 5.1381 E) and Herwijnen (52.9533 N, 4.7900 E), both in the Netherlands. In figure 5, the weather radar situated in Herwijnen is displayed. Both radars create volume scans with a resolution of 5 minutes. The radars transmit pulses by use of a magnetron. The pulse duration is 2  $\mu$ s and the peak power is equal to 250 kW. Each radar consists of a parabolic reflector with a diameter of 4.2 meters, which produces a beam of 1-degree width (Holleman, 2001). The radar antenna sends these pulses around the radar site at a fixed angle, while rotating 360  $^{\circ}$ . The quality of the radar's observations is known to decrease with distances over approximately 120 km, due to overshooting of precipitation (caused by the height of the radar beam increasing with distance due to the curvature of the Earth) (Overeem, 2009). The radar reflectivity composite products from the KNMI are generated from scans of elevation angles of 0.3, 1.1, 2.0, and 3.0 degrees. Linear interpolation of the radar reflectivities in altitude is executed to produce a single image for each radar at 1500 m. By taking a weighted average of the radar reflectivity measurements (in which the weight is determined by the distance from the radar to the respective measurement location), radar images from both radars are combined to form a composite reflectivity product (Wessels, 2006).



**Figure 5:** Weather radar in Herwijnen, the Netherlands (Wessels, 2006)

### 2.2.2.2 GPM Dual-frequency Precipitation Radar

The Global Precipitation Measurement (GPM) mission, initiated by NASA and the Japan Aerospace Exploration Agency (JAXA) in 2014, forms an international network of satellites aiming to provide precipitation measurements globally (NASA, 2017). The GPM Core Observatory satellite (GPM-CO) is the central device of the mission and its measurements serve as a reference standard for the precipitation measurements from the other satellites active in the constellation. The GPM-CO operates at Low Earth Orbit (LEO) at approximately 407 km altitude and has an inclination orbit of  $65^\circ$  (Battaglia et al., 2020).

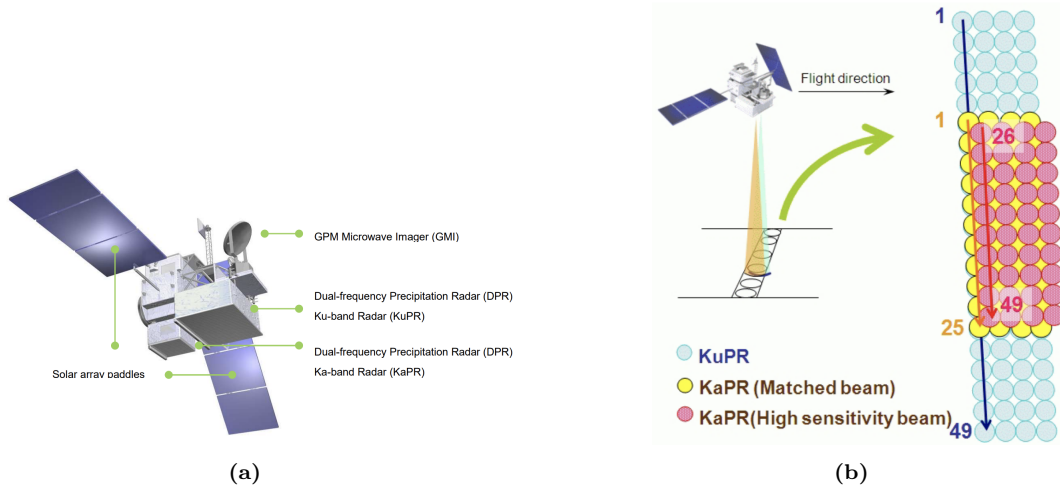


**Figure 6:** Schematic of the GPM Core Observatory satellite and its main components (left) and a visualization of its scanning method and width (right)

All GPM constellation satellites carry a radiometer, but the GPM-CO is the only one that carries a radar as well (JAXA, 2018) (see figure 6). The radar on the Core Observatory is called the Dual-frequency Precipitation Radar (DPR) and is the successor of the precipitation radar on the Tropical Rainfall Measuring Mission (TRMM) that was operative between 1997 and 2015 (Kidd et al., 2018). The DPR consists of a Ka-band precipitation radar (KaPR) operating at 35.5 GHz and a Ku-band precipitation radar (KuPR) operating at 13.6 GHz. The KuPR detects heavier rainfall, while the KaPR instruments can detect weak rainfall and snowfall. The DPR provides three different radar rain rate estimates for the GPM core satel-5lite: Ku-band-only, Ka-band-only and a product combining the two frequencies (Lasser and Foelsche, 2018). As this paper studies heavy precipitation, the KuPR will be the focus of this research and is thus further elaborated on below. The KuPR scan has 49 footprints in one scan with a spatial resolution of approximately 5.2 km nadir (see figure 6b). Each scan has a swath width of 245 km and a vertical range resolution of 250 m (Iguchi et al., 2010). See table A in Appendix A for all DPR Ku-band properties.

### 3 Literature Study

Below, prior research on comparing precipitation estimation techniques like the ones used in this research is discussed. Also, prior research on small-scale spatial rainfall variability will be addressed.

#### 3.1 Comparing Precipitation Estimates

Direct comparisons between the precipitation estimation techniques used in this research are challenging, as the three measuring devices and their subsequent products have different characteristics and are affected by varying factors.

##### 3.1.1 Challenges

Although the remote sensing technique of the two relies on the same principle, DPR and weather radar have different viewing geometries. The ground-based weather radar scans the surrounding area with a rotation angle of  $360^\circ$  at different elevation angles, whereas the space-based DPR looks downward and thus provides products in the vertical dimension at varying altitudes (Biswas and Chandrasekar, 2018). For direct comparisons between the two radars, attention has to be paid to differences in attenuation, spatial alignment, temporal resolution, measurement height, and many more factors (Overeem, 2009). In previous research, various methods have been used for matching and aligning space-borne and ground-based radar observations. Liao et al. (2001) resampled the data from ground-based radar and spaceborne radar (Precipitation Radar (PR) from the TRMM, the predecessor of the GPM DPR) datasets to a common grid, such that the reflectivity observations from the ground-based radar could be compared with the PR observations at varying altitudes. A way to minimize the errors due to resampling and interpolation of data to different grids, is by instead making use of volume sampling (Biswas and Chandrasekar, 2018). Biswan et al. (2018) performed volume matching at each geometric intersection of the ground-based radar and space radar beams. The reflectivity samples within each intersected volume were thus averaged, instead of resampled.

Speirs et al. (2017) assumed the measurement of a certain DPR footprint to represent the average rainfall rate across its respective  $20 \text{ km}^2$  footprint. To compare with the less coarse weather radar pixels, weather radar observations which had the respective GPM footprint centre as their nearest neighbour were averaged for every footprint. Gabella et al. (2017) approached the differences in temporal resolution between gauge, weather radar and DPR observations by performing temporal integration. Regarding spatial alignment, solely GPM footprints were considered within which a gauge was located (Speirs et al., 2017). Research by Tan et al. (2018) made use of a gauge network (PCMK) with very fine time intervals (1s, 1 min, 5 min), which allowed for exact comparisons with the instantaneous DPR estimates. The DPR data was used for overpasses where gauges were situated within 2.5 km (equal to the DPR radius) of the DPR footprint's centre. The PCMK gauge network was very dense, and thus only pixels were selected in which a minimum of 6 gauges were present.

##### 3.1.2 State-of-the-art

Prior to this research, multiple studies have been done on the comparison of surface precipitation products with the GPM DPR products. Research by Liao et al. (2001) compared reflectivity products from the TRMM Precipitation Radar (the predecessor of the GPM DPR) to a ground validation (GV) network of Doppler weather radars in Melbourne, Florida. The research showed that reflectivity products without attenuation correction showed higher correlations with the GV datasets at an altitude of 3000m (0.87) than at a lower altitude of 1500 m (0.84). Furthermore,

the correlation between the GV network and the attenuation corrected PR was considerably higher for stratiform rain than for convective rain, equal to 0.89 and 0.74 respectively. Speirs et al. (2017) researched the performance of the GPM DPR on complex terraneous areas in Switzerland. In their study, GPM DPR rainfall rate products of the DPR's first two operational years were evaluated against a network of four dual-polarization C-band weather radars and a dense gauge network. The research showed that POD for the radar product and DPR increases for an increased precipitation intensity threshold: a threshold of  $1 \text{ mm h}^{-1}$  and  $6 \text{ mm h}^{-1}$  resulted in a POD of 0.827 and 0.959, respectively. Consistently, the DPR product was found to underestimate rainfall rates, especially in winter. It was suggested that the quality of the GPM's performance is determined by whether the measurements take place in the solid phase or not. Furthermore, better performance of DPR in terms of POD was observed for convective rain than for stratiform rain (Gabella et al., 2017). Kidd et al. (2017) compared GPM Level 2 products with surface radar and dense gauge datasets over the Unites States and western Europe (Kidd et al., 2017). The focus of their study was to assess the general differences and/or similarities between the different precipitation products. The research showed that overall, the satellite products and surface datasets agree well with one another. The research showed that correlations between DPR and surface radar were generally good, namely 0.49 over Europe and 0.61 over the USA. Furthermore, their research suggested systematic differences between the seasonal performance of products between the US and Europe, which they presumed to be related to underlying satellite issues for differing meteorological regimes. Research by Petracca et al. (2018) aimed to validate the GPM DPR precipitation rate product over an 18-month period for surface radar and rain gauge data in mountainous area over the Italian Peninsula. It was again found that the DPR product performs better in warmer months. The POD for the Ku-product was found to be 0.66 and 0.44 for evaluations with radar and rain gauge data, respectively. Furthermore, it was found that increasing altitude results in an increased underestimation of the DPR product with respect to gauge and radar (Petracca et al., 2018). Research by Lasser et al. (2018) showed well resemblances of GPM-DPR rainfall rate estimates and a dense gauge network (the Wegenernet) in Austria, with a POD of 0.75 and FAR of 0.32 for the DPR Ku-band. A total of 22 rainfall events were considered in the analysis, and it showed that DPR Ka-band precipitation products matched best with the gauge observations. This was assumed to be caused by the high number of shallow rainfall events (Lasser and Foelsche, 2018). Research by Biswas and Chandrasekar (2018) comprised of a comparison of volume matched samples of weather radar and 250 overpasses of DPR, using Ku -and Ka-Band reflectivity observations over the southeastern plains of the U.S.A. The research showed good correspondence of DPR and GR reflectivity with correlations up to 0.9 and 0.85 for Ku -and Ka-band respectively (Biswas and Chandrasekar, 2018). Furthermore, it was observed that DPR underestimates heavy convective rainfall by a margin of 5 to 6 mm/h. Research by Tan et al. (2018) compared DPR Ku-band precipitation products against multiple gauge networks with precipitation intensities averaged over 5 minutes. They found the POD to be higher for a +5 min time lag (ranging from 0.61 to 0.82, varying per gauge network) to be higher than for a +0 min time lag, as well as the correlation factor (ranging from 0.57 - 0.8, varying per gauge network) (Tan et al., 2018). The Wegener network, located in Austria, showed the highest results for both POD and correlation with respect to the other networks, located in the mid-Atlantic coast and in Arizona, USA.

### 3.2 Small-scale spatial rainfall variability

There is still little knowledge on the variability of rainfall depth and rainfall intensity on a relatively small spatial scale ( $< 10 \text{ km}^2$ ) (Fiener and Auerswald, 2009). Consequently, even fewer insights are available on rainfall variability within the even smaller spatial scale of that of a satellite pixel ( $\pm 1 \text{ km}^2$ ). However, it is known that rainfall is a dynamic process and constantly changes in form and intensity in both time and space (Jensen and Pedersen, 2005). A conventional method to measure rainfall is by the use of a rain gauge, a point measurement

instrument that directly measures the rainfall depth over a relatively small area (approximately 3-400 cm<sup>2</sup>) (Jensen and Pedersen, 2005). Presently, multiple methods are being used that produce rainfall estimates over larger areas (kilometre-scale), like the well-known weather radar and satellite products. Also, more unconventional methods have emerged, like measuring rainfall by the use of microwave links from existing cellular communication networks (Overeem et al., 2011). Data from remote sensing devices, like satellites and weather radar, relate a certain measured property, like the reflection of electromagnetic waves from descending precipitation droplets, to rain rate (Jensen and Pedersen, 2005). Due to their coarser spatial resolution, remote sensing devices provide a spatially averaged rainfall estimate that represents a specific volume (the size based on its respective footprint and bin) (Peleg et al., 2013). These estimates are however not linearly averaged, due to the typical antenna patterns. Such a spatial average can be interpreted as uniform rainfall distribution. However, if that same area were to be filled with individual point measurement devices, the remotely sensed average output might not be an accurate representation of each individual point within that area. The human-made assumption in the interpretation of remotely sensed data of spatially uniform rainfall is invalid on the sub-kilometre scale, as processes in a rainstorm are variable and thus result in different rainfall amounts between neighbouring locations on the ground. Thus, in the case of full areal coverage of point measurement devices within the scale of a satellite pixel, there is still variation in rainfall measurements between one side of the pixel and the other. Knowledge of small-scale rainfall variability is important, for instance for improving rainfall-runoff relationships, knowledge of small-scale variability in soil moisture and thus on soil properties (Fiener and Auerwald, 2009) and for calibration purposes (Jensen and Pedersen, 2005). Below, previous studies on (small-scale) rainfall variability are reviewed.

### 3.2.1 Magnitude of variability

The precipitation as observed on the surface at a certain location is the final phase of various processes occurring at different scales (Berndtsson and Niemczynowicz, 1988) and therefore, spatially varying rainfall observations on small scales should be regarded as the product of multiple factors. The most obvious factor leading to differences in neighbouring measurement points is the occurrence of measurement errors, for example, caused by equipment defects or miscalculations. However, even in the case of a perfect areal measurement, i.e. point measurement devices covering the entire area of interest without any type of errors, spatial rainfall variability would still be expected. Although they used a sparser network of measurement devices than in the before-mentioned "perfect" measurement situation, the occurrence of spatial rainfall variability while excluding measurement errors was shown by Fiener & Auerwald (2009). They found a mean gradient of 4.2 mm km<sup>-1</sup> and a maximum of 15.7 mm km<sup>-1</sup>, using 13 measurement stations in a study area of 1.4 km<sup>2</sup>. They used continuous measurements from tipping buckets aggregated to minutes, for the time period of April 1994 - March 1998 (using only data from May - October). They reviewed results from previous work by Niemczynowicz et al. (1982) and Goodricht et al. (1995), which showed a maximum gradient of 5.5 mm km<sup>-2</sup> and 23.8 mm km<sup>-2</sup> for measurements aggregated to 1 minute intervals, respectively. This difference can be blamed on multiple factors, like climate and local geography. Another paper that displayed the occurrence of spatial variability on a small spatial scale is by Jensen & Pedersen (2005), who analyzed the coefficient of variation of a dozen closely aligned rain gauges (placed within several tens of squared metres) throughout multiple storm events for a period of 65 days. They found a significant rainfall variability between the measurement points, often with a factor of two between the lowest and highest observation (Jensen and Pedersen, 2005), and also took into account the effect of possible measurement errors. In a study by Pedersen et al. (2010), the spatial variability in rainfall events was defined by the use of a coefficient of variation, which was determined based on a precipitation data-set of 2 years from summer to fall using a total of 9 rain gauges over an area of 0.25 km<sup>2</sup> with a temporal aggregation interval of 1 minute (no

other aggregation intervals were used, but were recommended for future studies). The coefficient of variation is estimated as the ratio of the standard deviation to the arithmetic mean depth (Pedersen et al., 2010). It was found that the coefficient of variation ranges from 1 to 26 %, with a mean of 10% (Pedersen et al., 2010). However, if extreme events are taken into account, the coefficient of variation could even range from 1 to 47 %. Furthermore, they found the CV to decrease with increasing rainfall depth. These numbers were determined for the duration of each specific rainfall event, which was used when there were at least two registrations of rainfall with a time span of fewer than 60 minutes between these registrations (Pedersen et al., 2010).

Also, it was found that spatial differences develop during very short periods of time (Fiener and Auerswald, 2009), which can be related to the highly fluctuating nature of convective storm events (Syed et al., 2003). Therefore, spatial rainfall variability is most important when considering small temporal scales. Additionally, due to the aforementioned random orientation of the spatial trends, it might be suggested that there is no spatial variability in rainfall depth on larger temporal scales. This could imply that when using larger temporal scales, spatial variability can be neglected.

### **3.2.2 Factors affecting spatial variability**

The above-mentioned studies give way to the observation that small-scale spatial rainfall variability are the result of the physical aspects of precipitation processes. One of these aspects is the type of precipitation. Convective storms causing spatial rainfall variability are supported by the findings of Syed et al. (2003), who found that, generally, not the entire research area was under rain during a storm event. They related the rainfall differences between neighbouring points to either storm movement within a single storm event or to the presence of multiple storm cells within an event, covering the same sub-kilometre scale during a 17-year time period. Krawejski et al. (2003) analysed the spatial variance by use of dense networks of tipping-bucket rain gauges in five different climatic regions (Brazil, Florida, Iowa, Oklahoma and Guam, respectively). They made use of the Pearson correlation and the conditional probability of detection (CPD), defined as the probability of rainfall at one point given that it rains at another point during the same time interval (Krajewski et al., 2003), to indicate spatial variability. They found that the spatial correlation at short distances ( $< 0.5$  kilometre) is highly climate-dependent, as the values differ for the different regions. The lowest correlation was found in the areas that are dominated by local short-lived convective cells (Guam, Florida, Brazil). Furthermore, the CPD was found to be  $\pm 80$  % for all 15 min intervals at 1-kilometre intra-distance. This supports the fact that variability occurs frequently at the sub-kilometre scale. Fiener & Auerswald (2009) found that the spatial trends can be related to convective storm events, mainly due to the short periods during which the trends develop, the random orientation of the trend, the short time intervals and the nearly linear trend. The difference in spatial variation between convective and non-convective storm events is also supported by Peleg et al. (2013), who found that the spatial correlation (using Pearson's relation) for convective storm events decreases much more rapidly than for non-convective storm events. At the same distance of 1.8 km, it was found that the correlation coefficient for non-convective storms was equal to 0.7, whereas a much lower value of 0.4 was found for convective storms (Peleg et al., 2013). The study made use of 1-minute aggregated time intervals, accumulated from 1-second temporal resolution.

Apart from the physical aspects of precipitation processes, the spatial variability of rainfall is also location-dependent. It has for instance been shown that altitude plays a significant role in the amount of observed rainfall. This causes high spatial variability in mountainous areas, along with other factors such as windward or leeward exposure, buildings in urban areas and local wind effects (Berndtsson and Niemczynowicz, 1988).

## 4 Data

This research made use of three types of precipitation measuring devices: electronic gauges, weather radar and satellite radar. Details of the exact datasets used in this study, and their respective properties, will be given in section 4.2, after information on the study area has been given in section 4.1. Furthermore, information on the types of software that were used will be given in section 5.1.

### 4.1 Study Area

A study area needed to be selected based on several requirements to fulfil the criteria of the research problem. These requirements are laid out in the paragraph below. In the second paragraph, a description is given of the chosen study area.

#### 4.1.1 Requirements

The selection of an appropriate case study area was based on a few criteria. The case study area must:

1. Have climatic conditions in which precipitation events occur with an intensity of  $> 20$  *mm/h* (from hereon referred to as a high-intensity (HI) precipitation event);
2. Contain a relatively dense network of automatic weather stations with gauges that produce precipitation products at a high temporal resolution ( $= < 10$  minutes) and provide access to its respective (historic) data sets;
3. Be located in a region nearby a weather radar of which historic data sets of relatively raw precipitation products (namely: reflectivity factor) are available;
4. Be located in a region over which the GPM Core Observatory satellite passes (approximately) daily and of which are, subsequently, GPM-DPR Ku Level 2A data sets available.

Based on these criteria, the Netherlands was selected as an appropriate study area. In the following subsections, a brief description of the area and its respective climate will be given.

#### 4.1.2 Area description

Based on the above-listed criteria, the Netherlands was selected as an appropriate case study area (located 50.7 - 53.6 N, 3.3 - 7.2 E). The Netherlands has a temperate climate, with mean winter temperatures of about 3 degrees Celsius and mean summer temperatures of approximately 17 degrees Celsius. Precipitation occurs all year long, with an annual average of approximately 800-900 mm precipitation, and most daily annual maxima occurring from May - December. Most heavy precipitation events occur during the summer months when temperatures increase and the air becomes capable of containing more water vapour.

## 4.2 Data Acquisition

In this study, data is used from three different types of precipitation measuring techniques, namely electronic rain gauges, weather radar and space-borne radar. The characteristics of the data sets will be described below in sections 4.2.1, 4.2.2 and 4.2.3, respectively. An overview of the main characteristics is found in table 2 below. Furthermore, wind data used for the analysis is described in section 4.2.4.

	Rain Gauge	Weather Radar	Satellite
<b>Technique</b>	Electronic gauge	Dual-polarization C-band radar	Dual-frequency precipitation radar
<b>File format</b>	.txt	HDF5	HDF5
<b>Temporal resolution</b>	10 min	5 min	Instant
<b>Pixel size</b>	Point	1000 m x 1000 m	21.24 km <sup>2</sup>
<b>Pixels/file</b>	1	700 x 765	Varying
<b>Parameter</b>	Intensity [mm/h]	Reflectivity factor [dBZ]	Reflectivity factor [dBZ]
<b>Reference system</b>	EPSG4326	Stereographic	EPSG4326

**Table 2:** Characteristics of the three precipitation measuring techniques that are analyzed in this study: gauge, weather radar and satellite

#### 4.2.1 KNMI Automatic Gauge Network

The Royal Dutch Meteorology Institute (KNMI) maintains a network of 49 automatic weather stations (located at an average of 50 kilometres from another), of which the ones over land and within the study area boundaries ( $\pm 50.7 - 53.6$  N,  $3.3 - 7.2$  E) are used in this study. An overview of the resulting 33 weather stations is given in table A and the locations are displayed in figure 7 above. All stations operate electronic rain gauges (see section 2.2.1 for instrumental details).

Precipitation products of 10-minute time intervals were publicly available from the KNMI website and archived as *neerslaggegevens*, as monthly data containing all weather station data per year. The precipitation intensity products *ER\_intensity* and *ER\_duration* were used in this study, denoting the precipitation intensity in units of *mm/h* and the precipitation duration in seconds per 10-minute interval, respectively.

#### 4.2.2 KNMI C-band Weather Radar Network

The KNMI currently operates two dual-polarization C-band weather radars (see section 2.2.2.1 for instrumental details), in Herwijnen (51.8369 N, 5.1381 E) and Den Helder (52.9533 N, 4.7900 E), situated in the Netherlands (see figure 7). Prior to 2016, the radars were situated in De Bilt (52.10168 N, 5.17834 E) and Den Helder. Radar reflectivities are measured by both radars. These scans are used to generate a single image per radar at 1500 m altitude by linearly interpolating radar reflectivities in altitude. These two radar images are then combined to a single image by taking a weighted average of the radar reflectivities. The weights are a function of the distance of a given point to the radar.

The radar data was publicly available from the KNMI archive and was stored under *radar\_reflectivity\_composites* in HDF5 format. The timestamp in the file name corresponds to the start time of the lowest radar scan and the temporal resolution is 5 minutes.

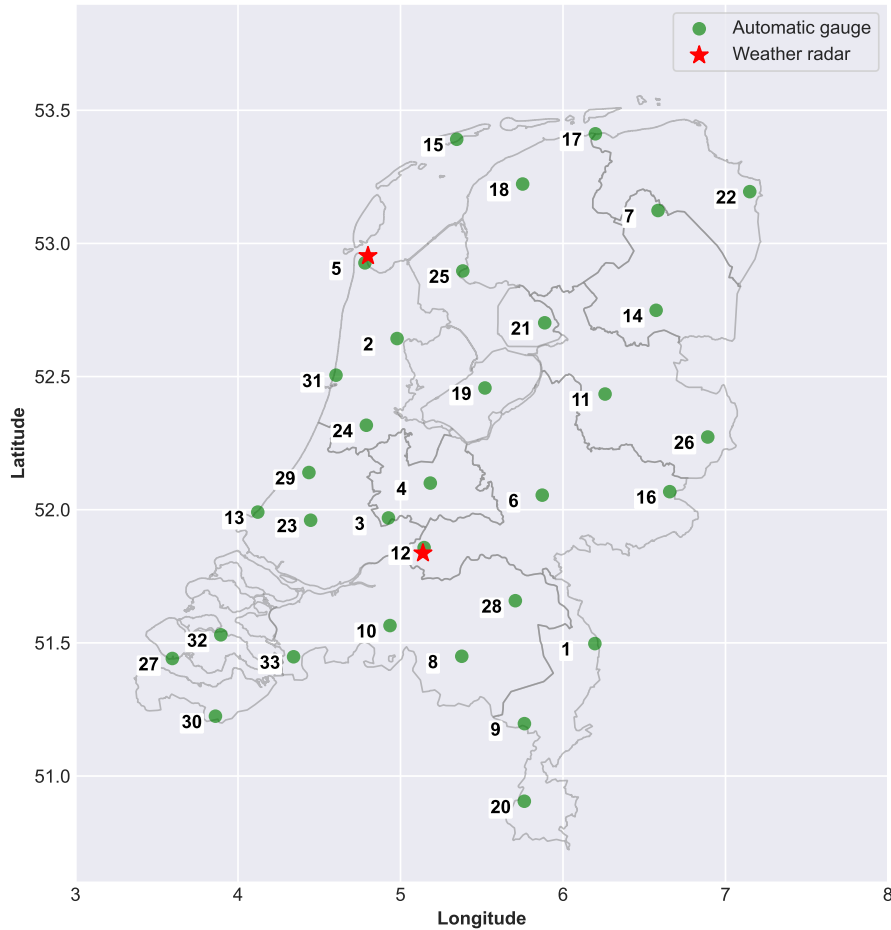


**Figure 7:** Map of the study area and the locations of the automatic rain gauges and weather stations that were used in this study. The annotation number refers to the station name, as presented in Appendix A in table A

### 4.2.3 GPM Dual-frequency Precipitation Radar

The GPM Dual-frequency Precipitation Radar (see section 2.2.2.2 for instrumental details) is selected to provide the space-borne observations used in this study. Multiple GPM DPR products are available: Level 1, Level 2 and Level 3, of which the key parameters are received power, reflectivity and precipitation, respectively (JAXA, 2018). In this research, Ku-band Level 2A products are used. A detailed description of the algorithm of this product can be found in the GPM/DPR Level-2 Algorithm Theoretical Basis Document (Iguchi et al., 2010).

The L2A products were publicly available in HDF5 format and downloaded from the Data Products Ordering Interface (STORM) of Precipitation Processing System (PPS) (<https://storm.pps.eosdis.nasa.gov>), a publicly available web-based data access interface for the GPM Mission’s products. After registration and selection of the required prerequisites (data type, satellite, instrument, spatial area of interest and the time range, see table A in Appendix A for specifics), the data sets were downloaded via a python script forwarded by STORM (see Appendix C). Using the GPM/DPR Level-2 Algorithm Theoretical Basis Document (Iguchi et al., 2010) and HDFView (see section 5.1 for details), the contents of the product were specified. One of the selected data-set products for analysis was  $Z_{factor\ measured}$  from the Preparation (PRE) Module,

which stored the vertical profile of the reflectivity factor without attenuation correction in dBZ.  $Z_{factor\ measured}$  is from hereon referred to as DPR reflectivity. As stated in the GPM/DPR Level-2A Algorithm Theoretical Basis Document,  $Z_{factor\ measured}$  is calculated using a radar equation at all range bins above the  $binClutterFreeBottom$ . The  $binClutterFreeBottom$  is the bin above which the signal is not affected by ground clutter and was found to vary per footprint from around 1400 m to 2100 m altitude. To assure uniform comparison results, data from an altitude of approximately 2000 m (i.e. bin number 158) was used, such that the used radar signals were not affected by ground clutter. Besides the reflectivity product,  $heightStormTop$ ,  $typePrecip$ ,  $precipRateNearSurface$ ,  $Latitude$ ,  $Longitude$  and  $Scantime$  were selected, referring to the height of the storm top in meters, the type of precipitation (given by number 1, 2 or 3, referring to stratiform, convective or other precipitation, respectively), the precipitation intensity at the surface in mm/h (estimated at the first DPR bin free from ground clutter, the latitude and longitude (representing the instantaneous field of view (i.e. IFOV)) and the time at which the GPM-CO passes and produces its scan, respectively (Iguchi et al., 2010).

#### 4.2.4 Wind Data

Winddata was extracted from Ventusky, a meteorological data visualization platform. This platform was used instead of for instance using KNMI data, as the platform provided wind data for various altitudes. The selected winddata was created based on a global ICON model, using data provided by DWD. 10-minute average measurements were used to compute wind orientation and wind speed at a 7 km resolution. The data was available for the entire case study area. Also, data was available for various altitudes up to 9000 meters, starting from the year 2018, such that the winddata could be matched with the respective DPR and WR data. In this study, winddata at 2500 m altitude was used, as it was the closest altitude to the clutter-free bins from the DPR. Wind maps were manually analyzed for all studies and a uniform wind direction and speed were used for a respective location if it was observed that there was little variation in horizontal distance.

### 4.3 Data Selection

To compare the three measuring techniques, multiple requirements must be met:

- First, the WR and DPR data sets must cover the research area. This requirement was met for the weather radar data, as the reflectivity composite product consequently covers the entirety of the Netherlands. However, the DPR overpass is irregular with respect to location. Although the GPM-CO passes the case study area approximately daily (i.e. occasionally twice a day, sometimes every other day), it showed that frequently only part of the entire case study area was covered in each overpass. Therefore, DPR data was not available for all high-intensity measurements close to DPR scan time, thus limiting the possibility of a comparison with a specific time range;
- A second condition was that WR and DPR data sets must cover the area during a significant number of high-intensity precipitation event recordings at one or multiple weather stations within the research area. This criterium was ultimately met;
- Thirdly, high-intensity precipitation events must occur with a (semi-)convective nature. Regarding the climate of the study area, this limited the data period to the months of May - October, when temperatures are highest.
- Fourthly and lastly, winddata at different altitudes had to be available. Therefore, the analysis consisted of data from the years 2018 - 2021.

In total, 396 DPR overpasses were available for that period and used in this analysis. Continuous gauge data was used from the months May, June, July, August, September and October for those respective years, except for 2020, from which only data from May and June is used due to processing difficulties. The weather radar data was used from the same time period.

## 5 Methodology

This chapter discusses the methodology of this study. First, a description of the software used in this research will be given. The methodology of this research can be subdivided into two main sections: processing of data and analysis of the processed data, which is done in sections 5.2 and 5.3. Ultimately, the three different types of data-sets ought to have the same format, such that they can be compared correctly. This is achieved in section 5.2.1. As the focus of this study is high-intensity precipitation, the data had to be filtered to temporally correspond to the occurrence of such events, which is explained in section 5.2.2. To make a fair comparison between the reflectivity data of weather radar and DPR, reflectivity data had to be converted to represent the same geographical coordinates, which is explained in section 5.2.3. After all data-sets were processed, multiple analyses were performed as explained in section 5.3. The relation between DPR and gauge observations was studied in section 5.3.1. In subsection 5.3.1.1, the performance of precipitation products was tested. Furthermore, in subsections 5.3.1.2 and 5.3.1.3 the relation between instantaneous reflectivity measurements and prior/later occurring HI-events was researched in both a visual and quantitative manner. Lastly, reflectivity observations from both DPR and weather radar were analyzed in section 5.3.2.

### 5.1 Software

This study uses programs HDFView and Python 2.7. HDFView is used for the visualization of the satellite data. The data processing is performed with Python 2.7, using the following packages: *os*, *numpy*, *matplotlib (pyplot)*, *pandas*, *math*, *numpy.ma*, *shapely.geometry (Point, MultiPoint)*, *geopandas*, *datetime*, *glob*, *geopy.distance*, *h5py*, *pyproj (Transformer, Geod)* *skimage.draw (polygon)*, *matplotlib.colors*, *scipy.interpolate*, *seaborn*, *matplotlib.cm*, *math*, *windrose*, *scipy stats (gaussiankde)*, *sklearn (pre-processing)*.

### 5.2 Data Processing

This section describes the steps taken prior to the data analysis, namely the pre-processing steps of gauge, weather radar and DPR data, the selection of high-intensity precipitation events and the temporal and geographical matching of all data sets.

#### 5.2.1 Pre-processing

The gauge (G), weather radar (WR) and satellite data (DPR) needed to be converted to the same format while containing the desired parameters, as well as temporal and geographical specifications. In the paragraphs below, a short description is given of how each data set was converted to pandas data frames format in Python 2.7.

##### 5.2.1.1 Gauge Data

The data sets were downloaded as text files. A few manual steps were performed before the data could be read as csv files in *Python*, as visualized in the flowchart in figure 8. The data for all weather stations were stored in one monthly file, with the geographical coordinates denoting the exact point location of each respective weather station. The data was already in the coordinate reference system EPSG4326 and thus needed no conversion.

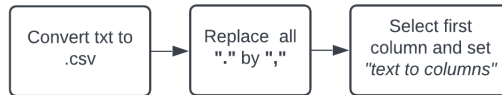


**Figure 8:** Gauge data-set conversion steps

### 5.2.1.2 Weather Radar Data

The weather radar data sets were downloaded as hdf5 files. Using HDFView, the exact contents of the data were viewed, which were stored in different subgroups. The reflectivity data were stored in the *image1* subgroup as *image\_data*, as an image with pixel values according to an RGB colour palette model. In the *Calibration* subgroup, *calibration\_formulas* was given as:

$$\text{GEO} = 0.500000 * \text{PV} + -31.500000 \quad (8)$$

, which was used to convert the pixel values (PV) extracted from *image\_data* to geophysical parameters (GEO), in this case to reflectivity in dBZ. The colour palette model had values ranging from 0 to 255. In the *Calibration* subgroup, *calibration\_missing\_data* and *calibration\_out\_of\_image* were found to be equal to 0 and 255, respectively. These values were subsequently set to none-values before the application of the calibration formula.

The following steps were taken to convert data to their respective grid locations in the EPSG4326 coordinate system. In the *geographic* subgroup, the geographical corners of the data grid were stored in [longitude, latitude] under *geo\_product\_corners*, moving clockwise from the lower-left corner. There were no latitude nor longitude grid data available for each pixel, thus a geographical grid had to be created manually that matched the known properties of the reflectivity grid: 700 columns x 765 rows. As the grid corners formed a non-equidistant grid, maximum and minimum latitude and longitude were used to define the grid range, after having been converted to represent the middle of their respective pixels. Next, the grid was created by using a meshgrid function, after which the stereographic coordinates were projected to EPSG4326. The reflectivity data were visualized on a geographical map, as displayed in figure ??, using only data  $\geq 11.8$  dBZ, determined by implementing the 0.5 mm/h detectability of the GPM DPR into the following approximation employed by the KNMI (Wessels, 2006):

$$\text{dBZ} = 16\log(R) + 23 \quad (9)$$

, derived from the Marshall-Palmer reflectivity - rainfall rate relation:

$$Z = 200R^{1.6} \quad (10)$$

, where  $Z$  is the reflectivity in  $\text{mm}^6\text{m}^{-3}$  and  $R$  the rain rate in  $\text{mm}/\text{h}$  (Wessels, 2006).  $\text{dBZ}$  represents the reflectivity factor in logarithmic units. An example of the processed WR data is displayed in figure ??.

### 5.2.1.3 DPR Data

Like the weather radar data, the DPR data was available in hdf5 format. As explained in chapter 4.2.3, the parameter data were stored in different subgroups. The parameters varying in altitude were stored in 3D matrices, so each parameter was available for different altitudes and could be selected as such. Geographical grid data was already available in EPSG4326 projection, so no further conversion was required. Only reflectivity data  $\geq 11.8$  dBZ was selected for the data analysis, based on the minimum detectability.

### 5.2.2 Filtering HI-Precipitation Data

To compare observations of high-intensity precipitation events for the different measuring techniques, subsections of each data set needed to be selected at the time of such an event. First, all DPR scans for the selected time period were matched geographically with the weather stations, as explained in section 5.2.2.1, after which they were temporally matched at the time of the high-intensity precipitation event, as explained in section 5.2.2.2.

#### 5.2.2.1 Geographical Matching

The initial matching (i.e. the process of temporally and spatially linking the different data-sets) was based on gauge and DPR data, as the overpass occurrence was a limiting factor for the DPR data and a high-intensity precipitation event occurrence a limiting factor for the gauge data. The data sets were geographically matched by first creating a circular buffer around each DPR IFOV and next joining the gauge data when an intersection was found with a weather station within that buffer. To perform a relatively tolerant matching, the buffer radius was set equal to a little over the radius of the DPR footprint, namely to 3000 m.

#### 5.2.2.2 Temporal Matching

Next, the dataset was filtered based on the requirement that the gauge data was within a specific time range from the respective DPR scantime. This range was set to 40 minutes, such that all data for gauge 10-minute intervals 40 minutes prior and 40 minutes after DPR scantime were kept. This timeframe was selected based on similar prior research (()). Note that the gauge temporal data was converted such that the time represented the start of the intensity measurement. To accurately match the gauge data with the respective DPR time, the data was re-sampled to 1-minute resolution. Finally, the data was split based on the 40-minute time range, thus consisting of a maximum of 8 gauge intervals matched with the corresponding DPR data, and will from here on be referred to as *events*.

#### 5.2.2.3 Selecting High-Intensity Precipitation Events

To only select events which consist of a gauge observation with a high precipitation intensity, the events were filtered based on that condition. The threshold for a high-intensity event (HI-event) was set to 15 mm/h, such that all events consisting of at least one or more intensity measurements equal to or higher than that respective intensity were selected. Time series were created displaying the gauge observations and the DPR reflectivity measurement within that specific time range (see figure 9 below for an example). Ultimately, a total of 26 events spread over 18 separate dates were found that met the above-mentioned requirements. An overview with the respective event characteristics is given in table 3. A weather station observing a high-intensity event within the specified time range is from hereon referred to as HI-WS. All case studies are classified based on the timing of the DPR scan time with regard to the timing of the high-intensity event as either C1 (DPR scantime during HI-interval), C2 (DPR scantime before HI-interval) or C3 (DPR scantime after HI-interval).

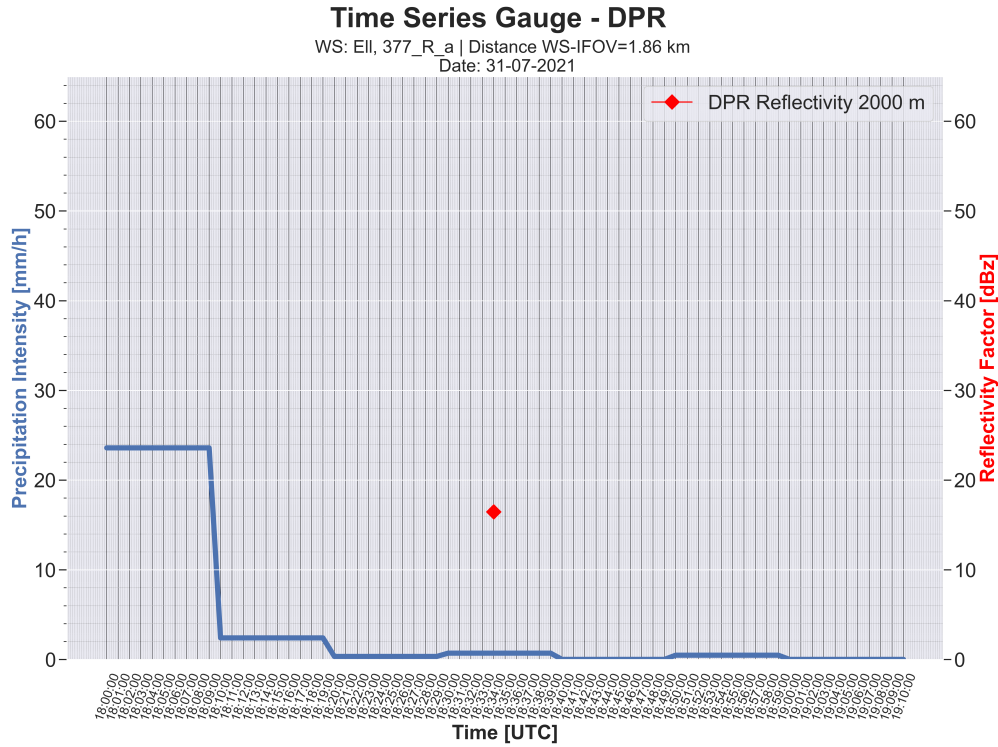


**Figure 9:** Time series of HI-event on 31-07-2021, with the blue graph displaying the precipitation intensity observed by the gauge and the red check displaying the DPR reflectivity of a DPR footprint within a 3 km range of the weather station location

### 5.2.3 Coupling WR and DPR

The weather radar data was selected for multiple timesteps before and after the DPR scan time for the found case studies from section 5.2.2. To directly compare the weather radar and DPR data in space, reflectivity data was required at equal locations. However, the data had different spatial resolutions (i.e. a WR pixel was approximately 20 times smaller than a DPR pixel) and unequal grid points. As a WR reflectivity composite product was used instead of a volume product, volume matching was not possible. Therefore, it was decided to convert the datasets to the other's grid by use of interpolation: either by downscaling the DPR data to the WR grid points or by upscaling the WR data to the DPR grid points. An advantage of downscaling the DPR data to the WR grid is that the WR properties (at higher spatial resolution) were maintained at each specific location, but a disadvantage was the number of data points. An advantage of converting the WR data to the DPR grid was the significant reduction in a number of data points (due to the coarser spatial resolution of the DPR data).

Both conversions were executed by use of interpolation. The interpolation was initially performed by use of both linear and nearest neighbour methods (see figures A.1a and A.1b for examples of both methods applied to DPR data in Appendix A). Finally, it was decided that linear interpolation represented the actual data more realistically and was thus used for further analysis steps. For the rest of the analysis, it should be noted that by interpolating the data, the data was modified and thus could alter in space from the original data.

### 5.3 Data Comparisons

Using the processed and matched data derived as described in the previous sections, different types of observations for the same precipitation event could be analyzed and compared. To study how DPR measurements compare in space and time to surface observations by gauges and weather radar, a performance analysis, qualitative analysis and a quantitative analysis were performed, as described in sections 5.3.1.1, 5.3.1.2 and 5.3.1.3, respectively. In section 5.3.2.1, the method for analyzing the relationship between weather radar and DPR will be discussed. Lastly, in section 5.3.1.1, a description for the formation of precipitation metrics from DPR and gauge data will be given.

#### 5.3.1 Gauge and Radar Relations

In this section, gauge intensity observations and weather radar reflectivity products are compared to DPR estimates. Some of the analyses made use of meteorological data to observe whether DPR observations could indeed be related to the gauge observations based on wind direction and wind speed, as would be expected. The qualitative analysis makes use only of the wind direction, whereas the quantitative analysis also makes use of the windspeed.

##### 5.3.1.1 Precipitation Product Performance

As explained in chapter 1, it is of vital importance to be able to measure and subsequently predict precipitation, and especially high-intensity precipitation, correctly. To assess whether the DPR observes the occurrence of (different types of) precipitation accurately with respect to the "true" gauge observations, performance metrics were determined. The Probability Of Detection (POD) factor and False Alarm Ratio (FAR) were determined for both products based on different precipitation thresholds and for varying distances from the WS to the DPR IFOV. Based on these metrics, a better understanding of the DPR's measurements alignment in time and space could be obtained. By coupling the DPR to different gauge time intervals, it could be analyzed whether a time lag exists between the DPR observations and the gauge observations. Furthermore, the WS measurements (at location X) were coupled to multiple surrounding DPR footprints, such that it could be observed whether the measurements match well geographically. The distance from the respective IFOV to location X was thereby implemented in the research to assess the accuracy of the intersecting DPR footprint. Two precipitation thresholds were used: 0.5 mm/h and 15 mm/h, to indicate the performance with respect to the occurrence of overall precipitation and to high-intensity precipitation, respectively. All matched DPR and gauge data were used, so not just the HI-events. The minimum threshold of 0.5 mm/h was chosen based on the minimum precipitation detection threshold of the DPR.

The POD and FAR were determined using the equations displayed on the right in figure 10, based on the confusion matrix displayed on the left in figure 10. The gauge precipitation product is seen as the true class (due to its ability to observe precipitation directly) and the DPR precipitation product as the predicted class, where TP, FP, FN and TN stand for true positive, false positive, false negative and true negative, respectively. In this research, true positive entails that both the DPR and gauge measure precipitation above a certain threshold, whereas a true negative indicates that both DPR and gauge measure precipitation below a certain threshold. False-positive indicates that the DPR measures above the threshold and the gauge does not, whereas false-negative indicates that the DPR measures below the threshold whereas the gauge does not. A high POD indicates that the DPR's precipitation estimates correspond well (i.e. both measure precipitation above the respective threshold) with the precipitation measurements on the surface by the respective gauge. A low POD indicates that the DPR often does not measure precipitation above the respective threshold, whereas the gauge does. If the footprint's IFOV closest to the WS location corresponds best, a high POD is expected for distances  $\leq 3$

km. If a low time lag corresponds to results in a high POD, it can be assumed that the DPR and gauge measurement correspond well in the temporal domain for the respective threshold.

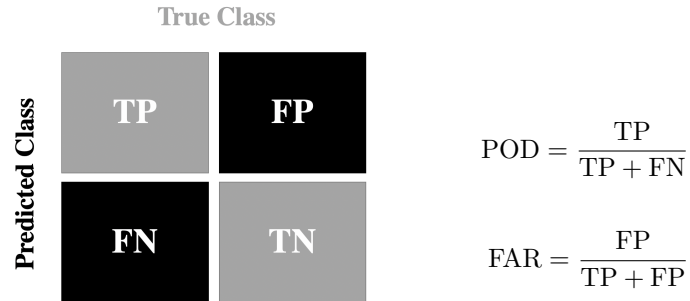


**Figure 10:** Confusion matrix(left) and associated formulas for Probability of Detection and False Alarm Ratio (right)

### 5.3.1.2 Qualitative Analysis

In this part of the analysis, DPR reflectivity scans were manually and visually compared to the observations from the gauge time-series and WR reflectivity scans, to see if certain patterns were visible. Based on the assumption that high reflectivity values correspond to high precipitation intensity (as discussed in chapter 2, see table 1), it was analyzed whether the instantaneous DPR reflectivity products could be visually linked to the occurrence of high-intensity precipitation events on the surface, as measured by gauges. For each case study, the wind direction and speed were retrieved. Per case study, it was analyzed whether high reflectivity zones (HR-zones, i.e. reflectivity  $\geq 35$  dB) were present close to the HI-WS. Based on the assumption that a storm system could have moved away from, or moved towards the HI-WS, during the time in between the HI-measurement and the DPR scan due to wind, it was analyzed whether the observed wind direction was related to the position of the HI-WS with respect to the presumably corresponding HR-zone, as was expected. If so, instantaneous DPR measurements could be used to propose possible locations and times of high-intensity precipitation events. For these analyses, the original DPR and WR reflectivity maps were used (i.e. mapped to their own respective grid, so not scaled). Note that for interpreting the analysis, the following items should be taken into account:

- A high-intensity measurement refers to the high-intensity interval (i.e.  $\geq 15$  mm/h) measured by a gauge system. This is not an instantaneous measurement, but an averaged value over the accumulated rainfall in 10 minutes time at that particular station. For simplicity reasons, such a high-intensity interval is from hereon referred to as *HI-interval*. Furthermore, when stated that for case study X a high-intensity interval is observed at weather station X, it is meant within a 40 minutes range before and after the DPR scan time.
- A high-reflectivity zone refers to a reflectivity measurement of  $\geq 35$  dB. For simplicity reasons, such a region is from hereon referred to as the *HR zone*.
- The *time lag* with respect to the DPR scan refers to the time difference between the DPR scan and the start of the high-intensity interval. For example, "*the intensity is measured 12 minutes before scan time*", indicates that the 10-minute interval in which the respective intensity is measured, started 12 minutes prior to scan time.

### 5.3.1.3 Quantitative Analysis

Based on the assumption that wind was related to the movement of storm systems and the findings from the qualitative analysis, a quantitative analysis was next performed based on the observed wind speed. To analyze whether the time in between the DPR scan time and the occurrence of a HI-event can be related to the wind speed, the following calculations were performed. Based on the assumption that a relatively nearby HR-zone relates to a certain HI-event, the time required for that respective HR-zone to travel to the HI-WS was derived based on wind speed and then compared to the actually measured time lag between the two measurements. For each of the calculations, the presumably corresponding high reflectivity zone was found as follows. Using the analysis from section 5.3.1.2, a latitude and longitude range was determined manually in which the high reflectivity zone was observed to be situated. Next, the pixel with the highest reflectivity value within that zone was selected. Using the coordinates of the selected pixel, the distance was calculated towards the respective HI-WS. Using equation 11, the expected time for that specific pixel (and thus the presumed storm) to reach the HI-WS was calculated, in which  $\bar{v}$  relates to the respective average observed wind speed,  $\Delta x$  to the distance between the HR-location and the HI-WS and  $\Delta t$  to the time required for the HR-region to pass over the HI-WS at 2000 m altitude. As the observed time lag represents the time from the DPR scan time to the moment precipitation is measured on the surface, the travel time for the vertical distance has to be incorporated as well. This is done by dividing the 2000 m vertical by the terminal drop velocity  $v_t$ , which indicates the speed of a precipitation particle when it falls through the air (as explained in chapter 2.1). The terminal velocity is dependent on the size of the precipitation particle, as explained in chapter 2.2.2. In this research, time lag ranges were determined with a minimum and maximum  $v_t$  of 3.18 and 10.06 m/s, based on average maximum and minimum drop radii equal to 2.5 and 0.25 mm, respectively. The final calculated time-lag presented in chapter 6.2.2 considers both the horizontal and the vertical distance from the location of the DPR measurement to the location of the gauge measurements.

$$\bar{v} = \frac{\Delta x}{\Delta t} \quad (11)$$

### 5.3.2 Reflectivity Relations

The reflectivity products of DPR were analyzed with respect to the geographically and temporally corresponding WR reflectivity products. It was assumed that when the products deviate least from one another, that that respective WR-scan relates best to the DPR data. Different successive WR scans were used, such that it could be analyzed whether a time lag existed between the two products or not. This was done based on analyzing deviations and correlations between the two data-sets, in sections 5.3.2.1 and 5.3.2.2, respectively. If the same pattern was observed for all case studies, an assumption could be made about a possible time lag and spatial relationships. The analyses were performed for both the up-scaled WR data and the down-scaled DPR data (such that the compared data-sets had the same grid points).

#### 5.3.2.1 Deviations

A method to study the relationship between the DPR and weather radar observations was by determining the deviation of DPR-reflectivity with respect to WR-reflectivity for different WR intervals, limited to the respective scan area of the DPR. This research comprised of subtraction of weather radar reflectivity from the DPR reflectivity at the same respective grid point, using the DPR data that had been linearly interpolated to the weather radar grid to secure a direct spatial comparison. By determining these deviations, it was analyzed how well the two reflectivity products compare in both space and time. The deviations are based on data in which missing values (i.e. *NaN-values*) are excluded, for both DPR and weather radar data, and only

reflectivity values  $\geq 11.8$  dBZ are used.

It should be noted that the spatial resolutions of the two datasets were originally different, with a footprint of  $1 \text{ km}^2$  and  $20 \text{ km}^2$  for WR and DPR, respectively. Through the interpolation process, they were visually equalized. Also, it should be taken into account that both WR and DPR produce one reflectivity product for each of their respective footprints, thereby averaging the small-scale existing processes within that footprint to one final averaged reflectivity product. Due to its smaller footprint, WR can take small-scale variation more accurately into account than DPR. Therefore, it was expected that even in zones where the reflectivity products correspond well, high deviations may be observed.

### 5.3.2.2 Correlations

Another manner used in this study to determine whether a relationship exists between the two variables, was by the creation of density scatterplots and derivation of the correlation coefficient. Based on the density scatterplot patterns, a linear regression line was created using equation 14, by implementing the slope  $m$  found in equation 12 and the y-intercept  $b$  from equation 13. For each case study, two regression lines were calculated, with either  $Z_{DPR}$  or  $Z_{WR}$  as independent variable, which denote the reflectivity in dBZ from the DPR and WR, respectively. In these equations,  $x$  and  $y$  represent the independent and dependent variable, respectively. Variable  $n$  denotes the number of scattered points. The regression line indicates how  $Z_{WR}$  is numerically related to  $Z_{DPR}$  and can be used as an indicator of which value  $Z_{WR}$  should have based on variable  $Z_{DPR}$ , and vice versa. A perfect linear relationship (i.e. if one variable increases by 1, consequently so will the other) occurs when the slope is equal to 1 and the y-intercept equal to 0. If the reflectivity products correspond well, a positive linear relationship with a slope close to 1 would be expected.

$$m = \frac{n \sum(xy) - \sum x \sum y}{n(\sum x^2) - (\sum x)^2} \quad (12)$$

$$b = \frac{\sum y - m \sum x}{n} \quad (13)$$

$$y = m * x + b \quad (14)$$

The Pearson correlation coefficient  $r$  determines the co-relationship between variables  $Z_{DPR}$  and  $Z_{WR}$  and was determined as follows:

$$r = \frac{\sum (Z_{DPR} - \overline{Z_{DPR}}) (Z_{WR} - \overline{Z_{WR}})}{\sqrt{\sum (Z_{DPR} - \overline{Z_{DPR}})^2 \sum (Z_{WR} - \overline{Z_{WR}})^2}} \quad (15)$$

, where  $Z_{DPR}$  and  $\overline{Z_{DPR}}$  denote the DPR reflectivity and mean reflectivity, respectively, and  $Z_{WR}$  and  $\overline{Z_{WR}}$  denote the weather radar reflectivity and mean reflectivity. A positive correlation coefficient indicates a positive relationship, thus when one variable increases, the other will too. A negative correlation coefficient means that when one variable increases, there is a decrease of the other. The larger the correlation coefficient (either positive or negative), the stronger the relationship between the two datasets. A correlation coefficient between 0.9 and 1.0 indicates that the variables are very highly correlated, between 0.7 and 0.9 indicates that the variables are highly correlated, between 0.5 and 0.7 indicates a moderate correlation and between 0.3 and 0.5 indicates that the variables have a low correlation. Below 0.3, the variables are considered to have little or no linear correlation (Calkins, 2005).

The analysis was performed for all data, as shown above, but also separately for convective and stratiform data, based on the *precipitation type* variable produced by the DPR algorithm.

Case Study Label	Date	Scantime (UTC)	Peak Time (UTC)	Nr. of HI-WS	Station Name(s)	Temporal Classification	Peak Intensity $mm/h$	Intensity at Scantime $mm/h$
A	09-08-2018	08:06	08:40	2	Ell	C2	37.6	0
			08:10		Maastricht	C2	48.1	11
B	23-08-2018	20:34	20:10	4	Deelen locatie obs02t	C3	16	0
			20:30		Hoogeveen	C1	16.1	16.1
			20:40		Heino	C2	25	1
			20:50		Volkel locatie A	C2	16.9	0
C	06-09-2018	16:19	15:50	1	Deelen locatie A	C3	22	4
D	21-09-2018	19:05	19:00	1	Herwijnen	C1	15.7	15.7
E	08-05-2019	17:02	17:20	1	Deelen locatie obs02t	C2	22.6	0
F	12-06-2019	07:06	07:00	1	Gilze-Rijen locatie 10t	C1	25.3	25.3
G	15-06-2019	06:04	05:40	1	Wijk aan Zee	C3	39.7	10.5
H	09-08-2019	20:53	20:50	1	Leeuwarden locatie A	C1	19.7	19.7
I	18-10-2019	17:41	18:00	1	Hoorn Terschelling	C2	44.3	6
J	27-06-2020	15:15	14:40	3	Heino	C3	21.9	0
			15:20		Hoogeveen	C2	18.5	4
			15:30; 15:40		Nieuw Beerta	C2	48; 104	0
K	04-06-2021	18:23	19:00	1	Arcen	C2	72.4	0
L	28-06-2021	11:40	11:30	2	Ell	C1	51.8	51.8
			12:10		Westdorpe	C2	34.9	0
M	25-07-2021	20:37	20:30	2	Rotterdam locatie 24t	C1	19.6	19.6
			20:00		De Bilt locatie A	C3	24	9
N	31-07-2021	18:34	18:00	1	Ell	C3	23.5	1
O	08-08-2021	16:21	16:50	1	Maastricht locatie 22t	C2	15.5	
P	15-08-2021	21:25	20:50	1	Hoorn Terschelling	C3	52.7	1
Q	27-08-2021	10:52	11:10	1	Volkel locatie A	C2	18	0
R	15-09-2021	05:26	05:00	1	Ell	C3	29.3	3
			04:50; 05:40		Arcen	C3, C2	17.8	4

**Table 3:** Overview of the characteristics of the 18 analyzed case studies

## 6 Assessing Coupled Observations

The results from the analyses, as described in chapter 5.3, will be discussed in this chapter. In section 6.1, the precipitation products' performance will be assessed for both DPR and gauge data. Section 6.2.1 will next discuss the main findings from the visual analysis of gauge measurements relating to reflectivity measurements. Section 6.2.2 will continue on these findings, by discussing how the wind speed was found to relate to the observations from the visual analysis. Lastly, it will be discussed how reflectivity products from DPR and WR were found to relate to one another in both time and space in section 6.3.

### 6.1 Metrics

The precipitation metrics were used to assess the performance of the DPR to predict precipitation, and to obtain an idea of how accurate the DPR's performance is in both the spatial and the temporal domains. In figures 11 and figure 12, the POD and FAR, respectively, are shown for two precipitation intensity thresholds and multiple distances from the WS to the DPR's IFOV.

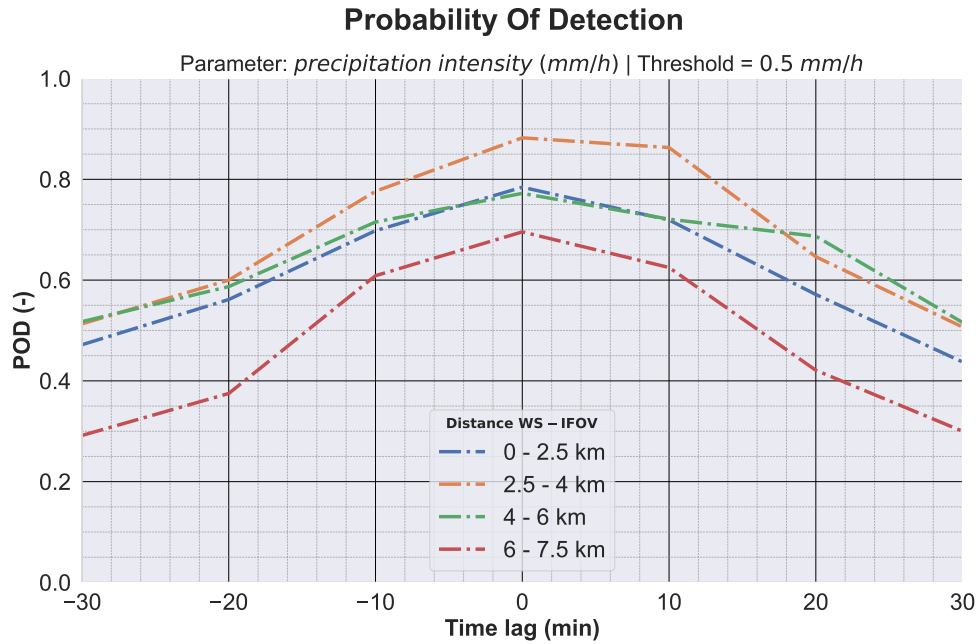
The results for POD and FAR show that the DPR precipitation product corresponds relatively well in time with the gauge product for a threshold of 0.5 mm/h (i.e. precipitation occurrence in general), as the POD is highest with a time lag of 0 (i.e. POD and FAR range of  $\pm 0.7 - 0.9$  and  $0.18 - 0.25$ , respectively). It is observed that, for all distances, the POD decreases with increased time-lag. Regarding spatial relations, it shows that the POD is lowest for IFOVs situated at  $\geq 4$  km. The highest PODs are found for distances between 2.5-4 km. Regarding the DPR footprint size, the 2.5-4 km range could either relate to the footprint intersecting with the WS or a neighbouring footprint, i.e. when the WS is situated near the edge of a footprint. The POD results for the threshold of 15 mm/h showed very little correspondence between DPR and gauge data, as the POD was lower than 0.4 for all distances. Regarding the spatial domain, the furthest distance range again resulted in the lowest POD, now being equal to zero. Regarding the temporal domain, it showed that the POD was highest for a time lag of +10 minutes, thus the DPR data corresponded best with one gauge interval later than the one it temporally coincided with.

### 6.2 Comparison Gauge and Radar Observations

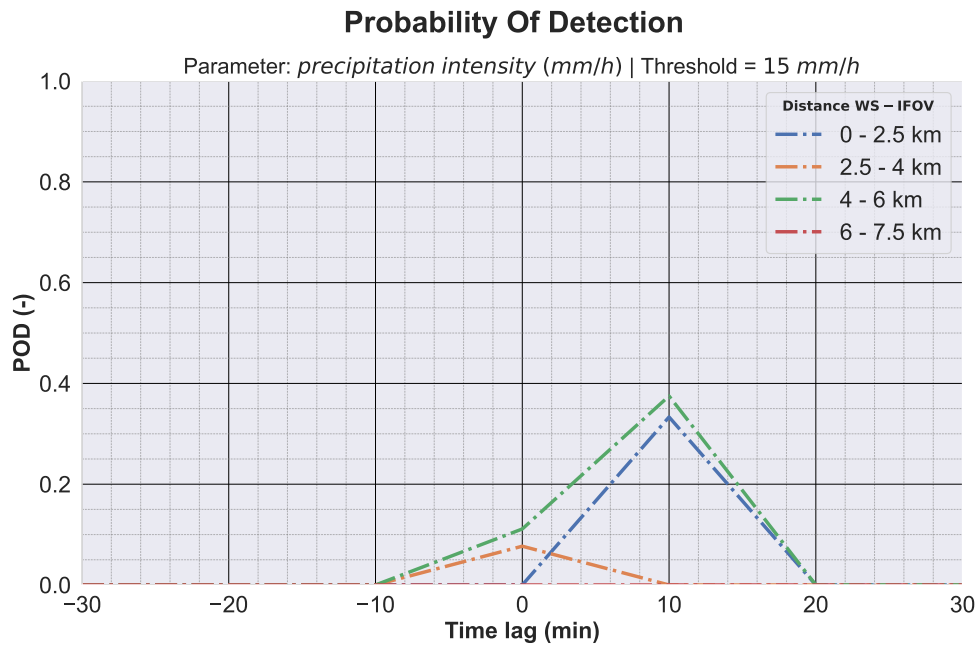
To observe whether relations in time and space can be found between instantaneous DPR measurements and surface precipitation intensity measurements, a manual analysis is performed for all case studies.

#### 6.2.1 Visual Analysis Events

The performed analyses as explained in chapter 5.3.1.2 aimed to find out whether the presence of high reflectivity zones nearby the location of a HI-WS was found and whether the wind orientation could be related to the observations. From these analyses, it was found that the wind orientation corresponded with the location of the HI-WS with respect to a nearby HR-zone, as was expected. Furthermore, for all cases, it showed that zero precipitation intervals corresponded to none or low reflectivity measurements. An example such an analysis is given on page 37 for case study N. The analyses of the other case studies can be found in Appendix B

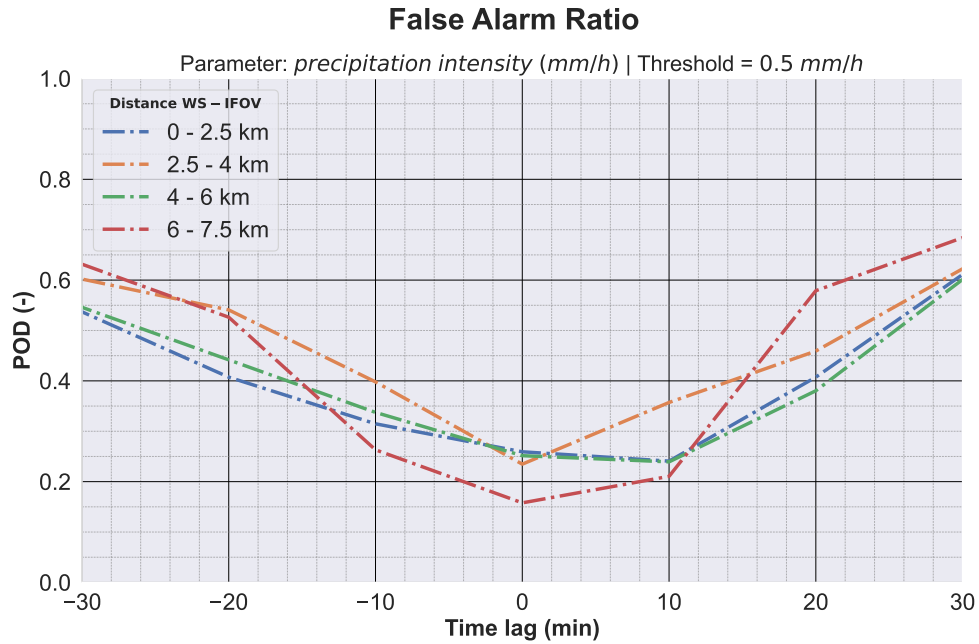


(a) Threshold: 0.5 mm/h

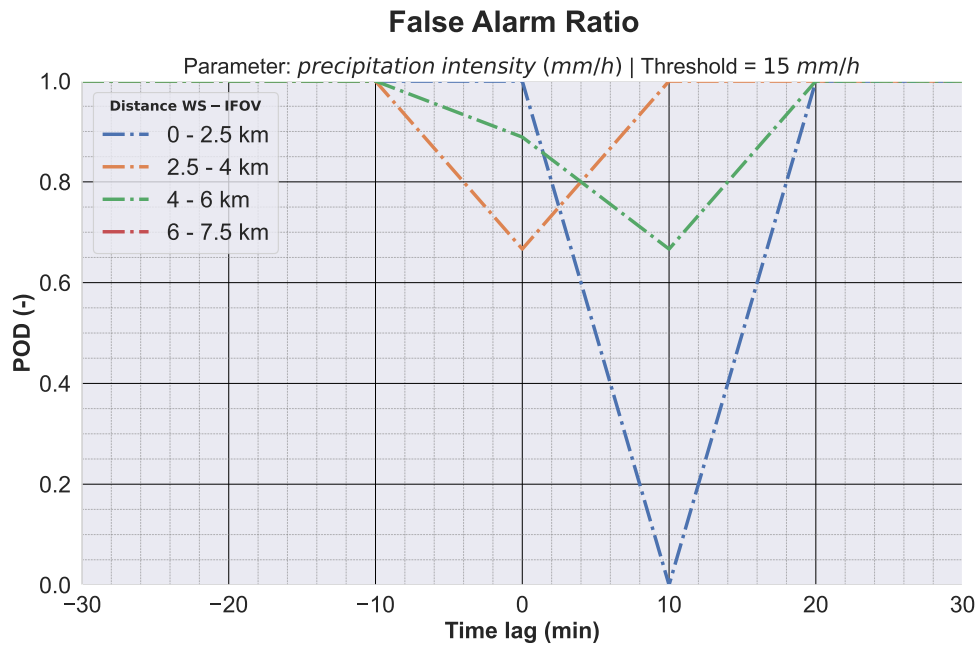


(b) Threshold: 15 mm/h

**Figure 11:** Probability Of Detection factor with respect to the time-lag from the gauge interval coinciding with scantime to the one used for the metrics calculation, for different distances from the HI-WS to IFOV



(a) Threshold: 0.5 mm/h



(b) Threshold: 15 mm/h

**Figure 12:** False Alarm Ratio with respect to the time-lag from the gauge interval coinciding with scantime to the one used for the metrics calculation, for different distances from the HI-WS to IFOV

**Case Study N**

WS *Ell* observes an intensity of 23.6 mm/h 34 minutes prior to DPR scan time. During scan time, a marginal intensity is observed and a low reflectivity zone. Multiple high reflectivity zones are visible in the scan, of which the closest ones are located on the east of the HI-WS. A westerly wind is observed, thus it could be assumed that the HR zones in the east are related to the HI-event at *Ell*. The wind speed is moderate and the time lag relatively high, thus presumably the second furthest HR zone corresponds to the HI-peak.

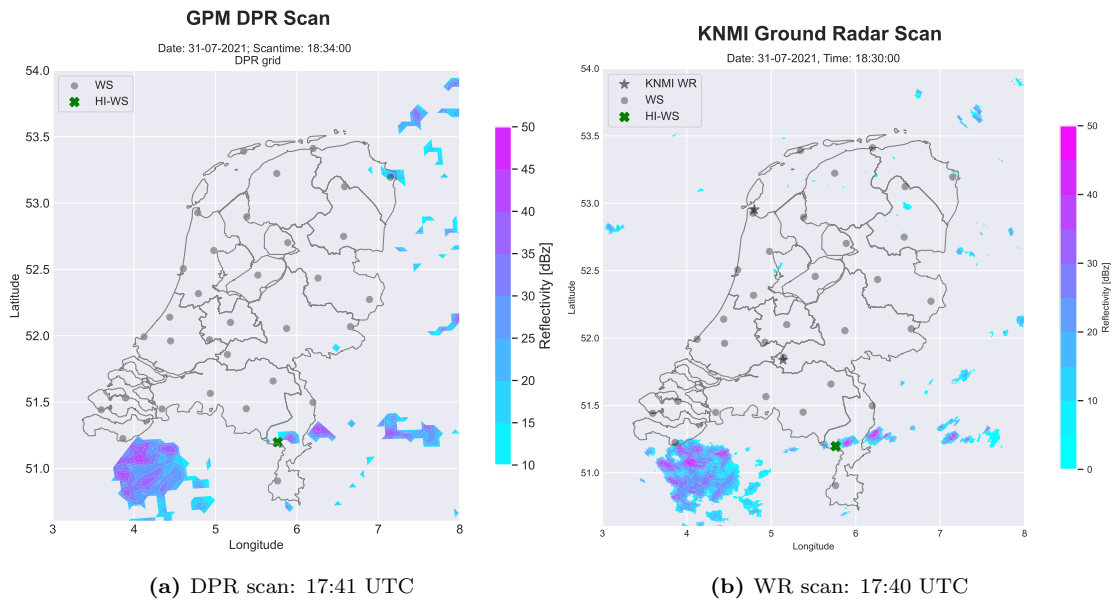


**Figure 13:** Reflectivity scans of 31-07-2021; HI-measurement starting at 20:50 UTC

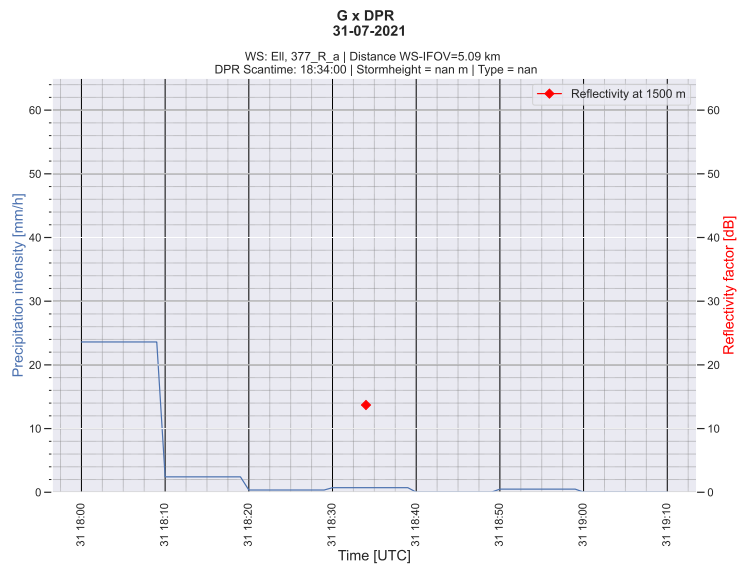


**Figure 14:** Time series of HI-WS measurements within a range of  $\pm 40$  minutes from DPR scan time on 31-07-2021; the red check indicates the DPR reflectivity

### 6.2.2 Wind Speed Influence

To support the visual analysis described in the previous section, calculations were performed to determine the time it would take the high reflectivity zone presumably corresponding to the high-intensity interval to pass over the HI-WS. These calculations were based on the observed wind speed and calculated distance, as explained in chapter 5.3.1.3. The calculations were performed for a selection of the 18 case studies, on the condition that a clearly visible high-reflectivity zone could be determined within a sufficient distance from the HI-WS to perform the calculations. The results of the calculations are displayed in table 4 on the following page, in which the calculated time lag implements both the horizontal and vertical distance from the reflectivity measurement to the surface gauge measurement and is shown for both the minimum and maximum terminal velocity  $v_t$  (based on drop radii of 0.25 and 2.5 mm, respectively). If the results did not agree with the calculated time lags, they are highlighted in red. If there were any uncertainties with regard to the presumably related high reflectivity zone from chapter 6.2.1, multiple high reflectivity pixels were selected for the calculations and hence multiple results are displayed in table 4 for those cases. Maps displaying the selected high reflectivity pixel and the respective high-intensity weather station for each analyzed case can be found in Appendix B.

Overall, the calculated time lags coincided well with the timings of the HI-intervals. As stated above, for some case studies multiple high reflectivity pixels were considered for the analysis, namely case studies E, N and R. For case study E, two options were considered, which are both displayed in figure 15a. The first calculation was based on the highest reflectivity zone near the HI-WS, which was slightly more south than the wind direction. The second calculation was based on the highest reflectivity pixel directly orientated against the wind direction. The first assumption resulted in a much higher time lag than the observed time lag, whereas the second assumption's result quite agreed with the observed time lag. The visual analysis for case study N showed two close-by high-reflectivity zones situated in the direction of the wind (see figure 15b), hence both could be considered to relate to the high-intensity interval. The calculations show that the closest selected pixel agrees most with the actual time lag. For the other case studies, only one high reflectivity pixel was considered for the analysis. It showed that for the majority of analyzed case studies, the calculated time lags agree well with the timing of the high-intensity intervals, with the calculated time-lags either being within the actual time lag range or a few minutes outside the range. Only case studies A and B (WS: Hoogeveen) showed high deviations from the actual time lag.

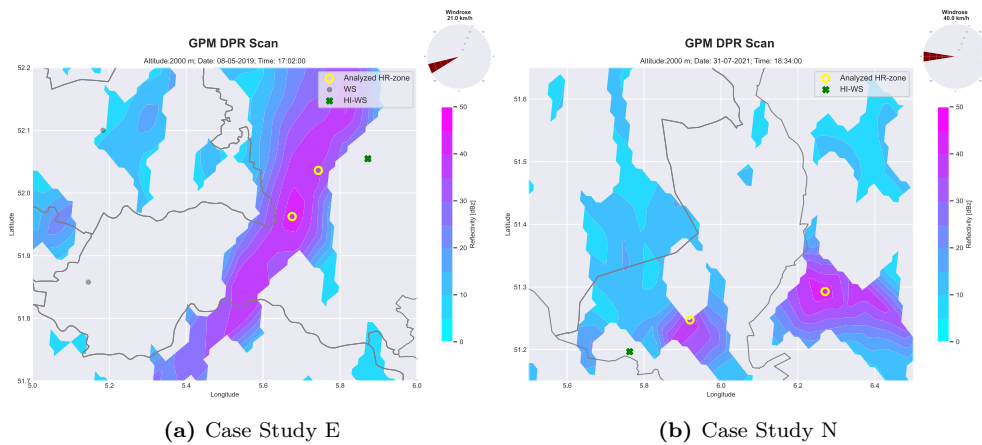


**Figure 15:** Selected high-reflectivity pixels (denoted by the yellow circle) presumed to be related to the HI-event at the weather station (denoted by the green cross)

Case Study	Station Name	$Z_{DPR}$ dBZ	Distance WS-HR km	Windspeed km/h	Actual Timelag min	Calculated Timelag min $v_t$ - max $v_t$ min
<b>A</b>	Ell	40.4	31.8	41	34 - 44	50 - 57
	Volkel locatie obs24Rt	35.0	13.6	49	15 - 25	20 - 27
<b>B</b>	Deelen locatie obs02t	29.9	13.7	49	15 - 25	20 - 27
	Hooerveen	39.9	11.4	49	± 5	17 - 24
<b>E</b>	Deelen locatie obs02t	44	17.0	21	18 - 28	52 - 59
	Deelen locatie obs02t	35.7	9.1	21	18 - 28	29 - 39
<b>I</b>	Hoorn Terschelling	44.8	21.5	81	19 - 29	19 - 27
<b>J</b>	Heino	46.1	30.6	65	24 - 34	31 - 38
<b>N</b>	Ell	38.5	12.3	40	24 - 34	21 - 28
	Ell	43.7	37.1	40	24 - 34	59 - 66
<b>O</b>	Maastricht locatie 22t	35.9	32.3	54	29 - 39	35 - 42
<b>P</b>	Hoorn Terschelling	41.0	20.0	67	25 - 35	21 - 28
<b>Q</b>	Volkel locatie obs24Rt	35.5	12.0	35	18 - 28	24 - 31
	Ell	33.5	14.5	40	16 - 26	25 - 32
<b>R</b>	Ell	38.6	38.0	40	16 - 26	60 - 67

**Table 4:** Overview of calculation parameters per case study and the result of the calculations as Calculated Timelag. The results that were not in agreement with the actual timelag are highlighted red

### 6.3 Reflectivity Relations

In this section, the results from section 5.3.2.1 will be discussed.

#### 6.3.1 Direct Reflectivity Comparisons

The original WR and DPR reflectivity maps showed clear correspondence with one another (see figure 16a and 16b for resulting maps of case study F). Similar reflectivity patterns were observed, with reflectivity increasing towards the middle of each reflectivity zone. Due to its higher spatial resolution, more variance on a smaller scale is observed in the WR maps compared to the DPR maps. Furthermore, more separate low reflectivity zones were observed in the DPR scans. Also, the magnitude of reflectivity observations from DPR appears to be constantly higher than WR. These patterns were observed in all case studies. It should be noted that the reflectivity scans from DPR are limited to the overpass location for that specific date, which directly results in possible differences between WR and DPR scans. As observed in the maps below, the DPR reflectivity observations end in an unnatural manner just east of the HI-WS, where the WR scan does contain reflectivity observations  $\geq 11.8$  dBZ.

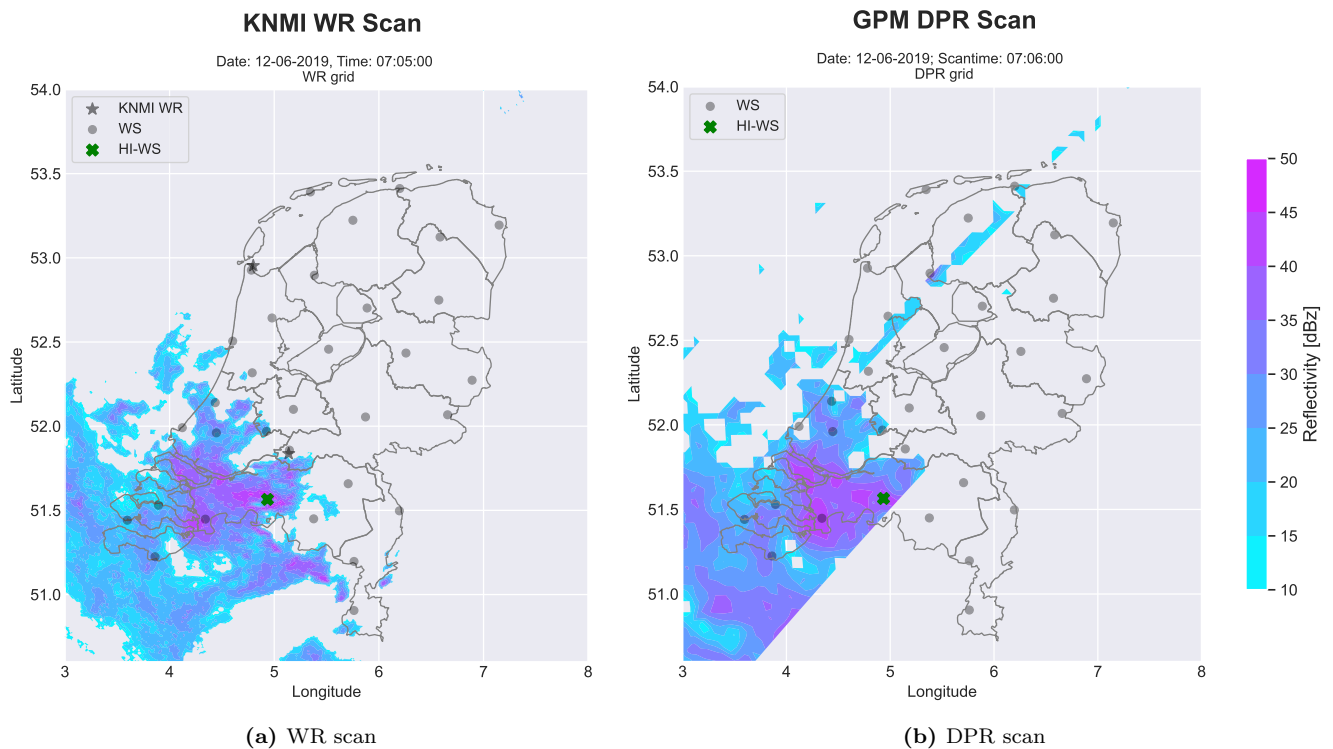
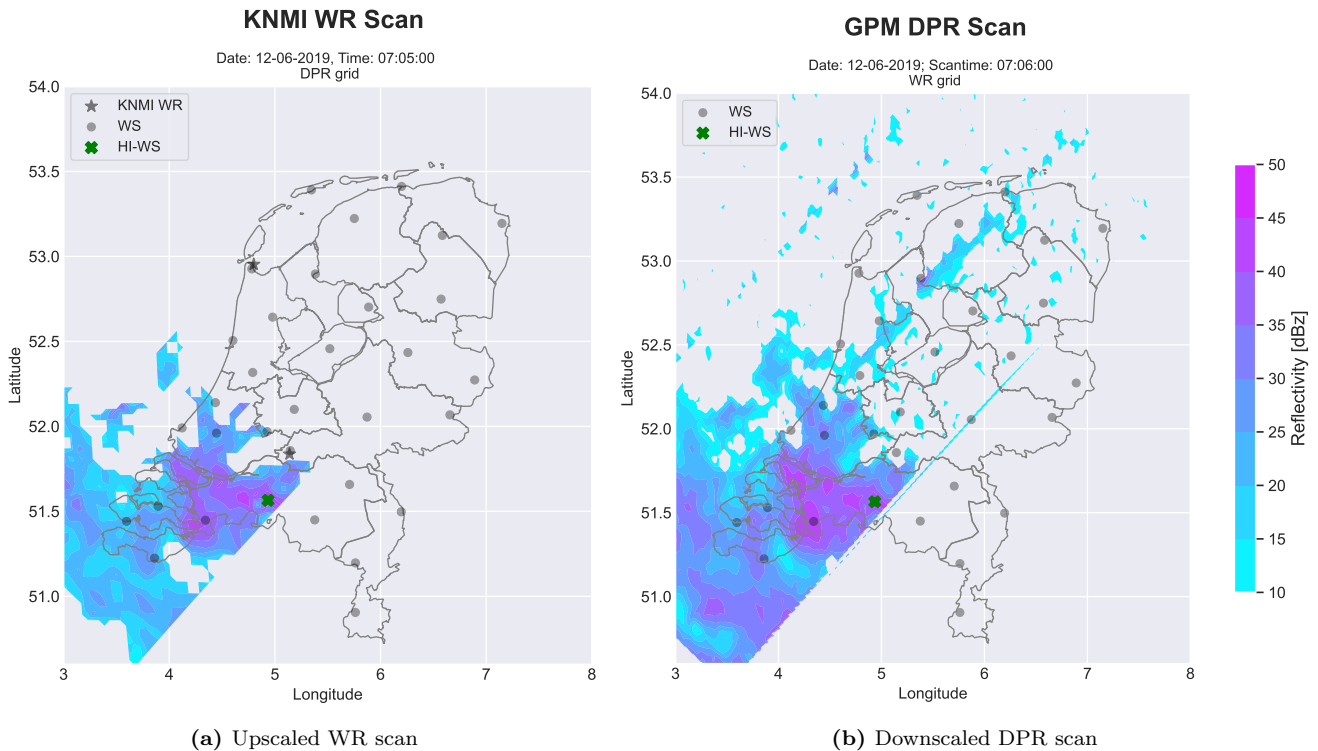


Figure 16: WR and DPR reflectivity scans for case study F

As explained in section 5.2.3, the DPR and WR data were converted to the other's respective grids, such that the data would be co-located and fit for direct comparisons. The resulting upscaled WR data and downscaled DPR data are displayed in figure 17a and 17b, respectively, for case study F. When comparing the maps to their original counterparts, the following was observed. Logically, the upscaled WR data show more averaged reflectivity zones and less small-scale variation. The upscaled reflectivity patterns are observed to resemble the original observations well, as the same magnitude of reflectivity is observed at the expected locations and the area sizes of the reflectivity zones are similar as well. In the downscaled DPR reflectivity maps, two notable things were observed. In all upscaled DPR maps, a pattern of scattered low reflectivity zones is observed at locations where no reflectivity  $\geq 11.8$  was observed in the original maps. Furthermore, the areas of reflectivity zones appear to have expanded in the downscaled maps with respect to the original DPR maps. Based on these observations, it could be stated that the results from upscaling WR data are more representative of reality than the results from downscaling DPR data.



**Figure 17:** Interpolated WR data to DPR grid points (left) and DPR data to WR grid points (right)

### 6.3.2 Deviations

As explained in section 5.3.2.1, to relate the reflectivity products of both DPR and WR in space and time, the reflectivity deviations per grid point were created on geographical maps for different WR scans, as shown in figures 19a and 19b for case study G. A positive deviation (coloured red in the figure) indicates that the DPR reflectivity is higher than the weather radar reflectivity. A negative deviation (coloured blue) shows that the weather radar reflectivity is higher than the DPR reflectivity for that specific location. When solely light blue or light red colours are observed, it indicates that both reflectivity products correspond relatively well with one another (i.e. a variance  $\leq 5$  dBZ).

### 6.3.2.1 Scaling Influence

The deviation maps were created for both scaling methods (i.e. for data on the WR grid and the DPR grid), as visualized in figure 18 for case study F. As expected, the higher spatial resolution of the data on the WR grid results in more small-scale deviations (figure 18a), whereas the deviations on the DPR grid are more averaged in space (figure 18b). The patterns are however observed to agree, showing low and high deviations at similar locations.

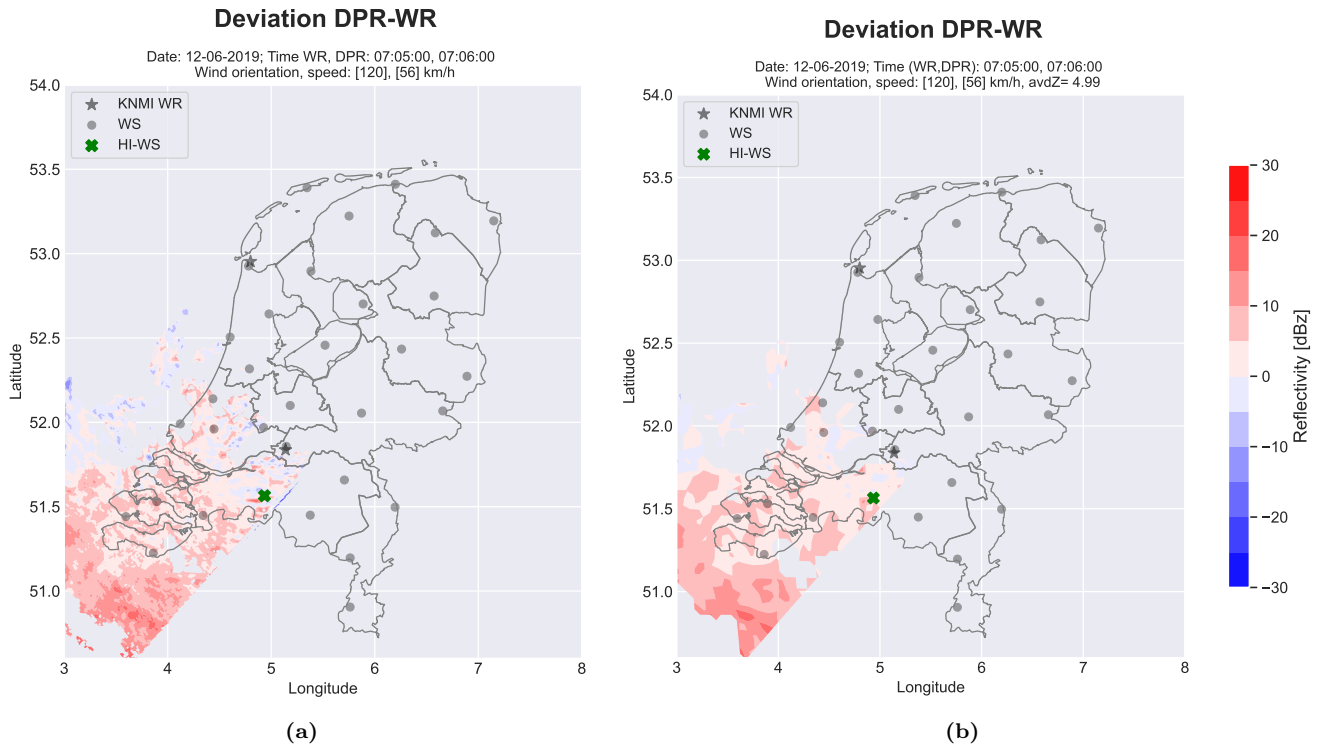


**Figure 18:** Reflectivity deviation maps for case study F with downsampled data (left) and upsampled data (right)

### 6.3.2.2 Temporal influence

By comparing the deviation maps for varying WR scan times, assumptions could be made of whether the weather radar measurements experience a temporal delay with regard to the DPR measurements, and vice versa. Also, high deviations were analyzed with regard to location, to see if specific patterns could be observed. As can be seen in case study G, the deviations are much higher in figure 19b, where weather radar data is used with a higher time-lag with respect to DPR scantime than in figure 19a. This increase in deviations with increasing time-lag was observed for all case studies (see Appendix B). With regard to the spatial domain, it was observed that high deviation zones were still present, both at a small scale and a large scale, for the combination of DPR and WR scans that showed highest correspondence (i.e. overall least deviations). These DPR and WR matches that show least extreme deviations will from here on be referred to as *best matches*,

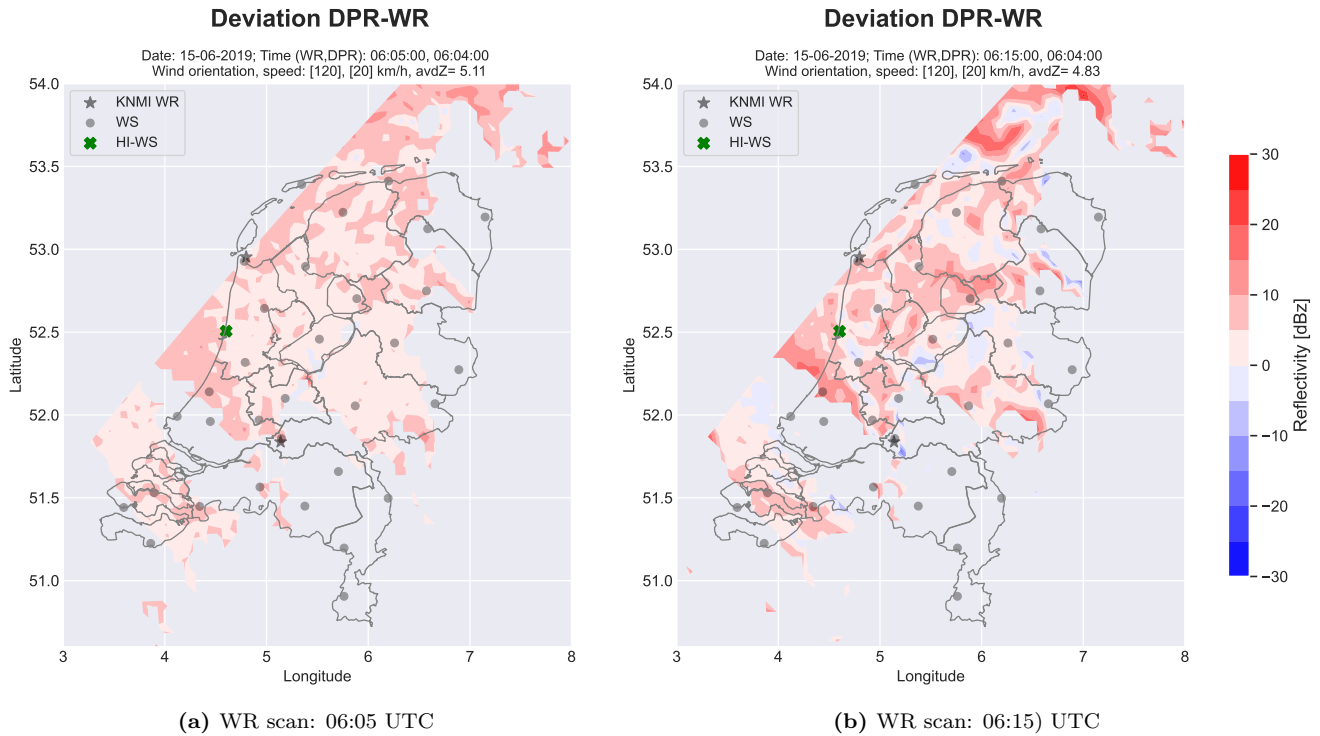


**Figure 19:** Reflectivity deviation maps for case study G using upscaled data for two WR intervals: 06:05:00 UTC (left) and 06:15:00 UTC (right), with DPR scantime equal to 06:04:00 UTC

### 6.3.2.3 Remarkabilities

In several of the deviation maps of the earlier denoted *best matches*, where low deviations were expected, relatively large regions with high deviations were observed. This was observed in the deviation maps based on both WR and DPR grids. However, small-scale high deviations were only observed in the maps based on WR grids. An example of the low-scale high deviations is for instance visible in figure 18a. An example of large-scale high deviations are displayed in figure 20, alongside the corresponding WR and DPR scans. In the southeast of the map, a zone of high reflectivity deviation is visible (indicating high  $Z_{DPR}$  observations with respect to  $Z_{WR}$ ), as well as unnatural gaps at locations where high  $Z_{DPR}$  is observed in the DPR map. Another example is visualized in figure 21, where a large-scale and relatively high deviation zone is observed in the east. The same phenomenon is observed in case study F as presented earlier (see figures 18), where a large high deviation zone is observed in the southwest of the map.

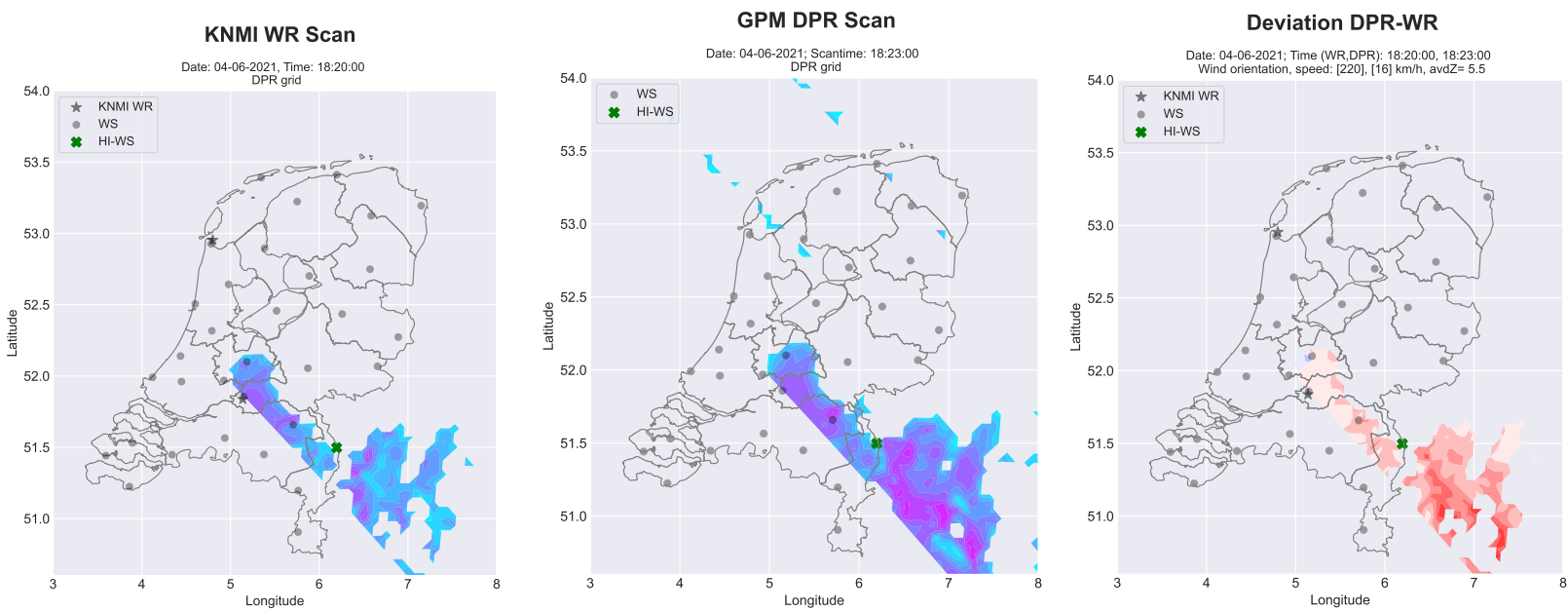
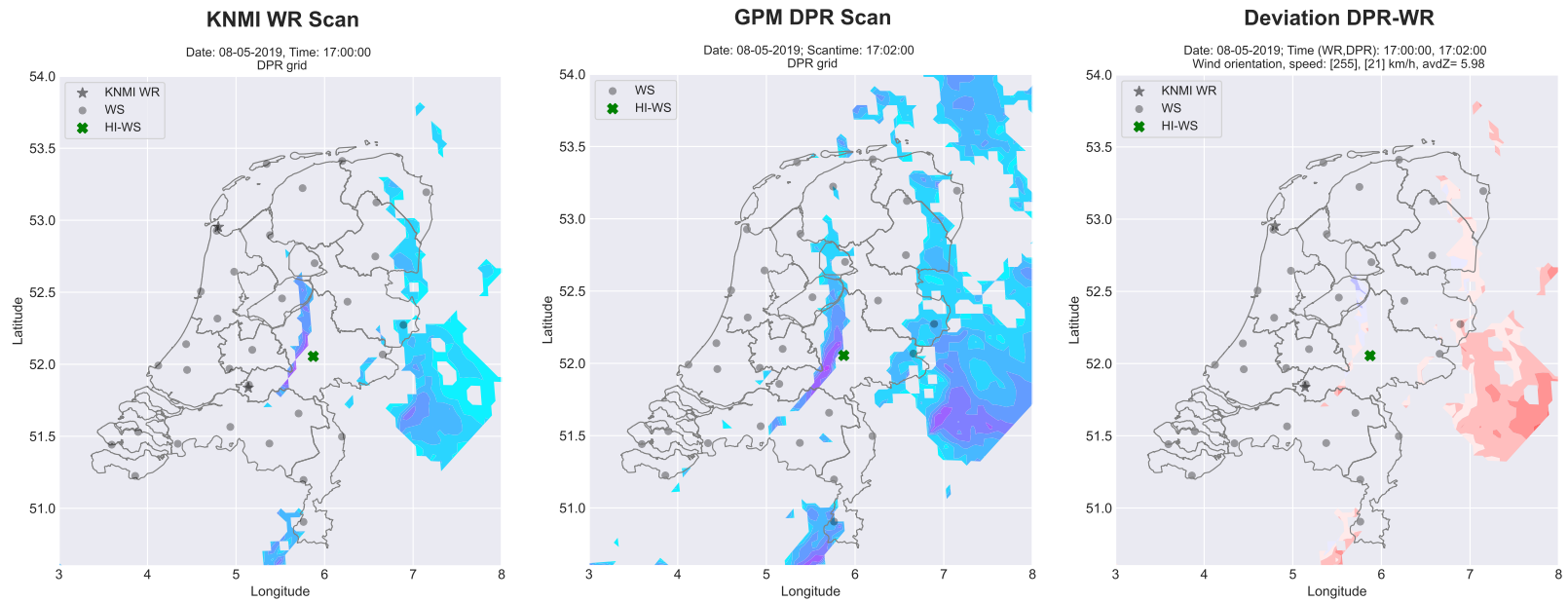


Figure 20: Upscaled WR scan, DPR scan and upscaled reflectivity deviation map for case study K



(a) WR scan: 06:05 UTC



Figure 21: Upscaled WR scan, DPR scan and upscaled reflectivity deviation map for case study E

### 6.3.3 Correlations

In this section, the results from 5.3.2.2 are presented, discussing temporal influence, scaling influence and precipitation type influence on the relationship between  $Z_{DPR}$  and  $Z_{WR}$ .

#### 6.3.3.1 Temporal Influence

In figure 22, density scatter plots are shown displaying the relationship between DPR reflectivity and WR reflectivity (upscaled to DPR grid) at equal grid points for case study R for two different WR scan times. For all case studies (see Appendix B), the regression line shows a positive, linear relationship for weather radar intervals coinciding with DPR-scan time or for weather radar intervals within a range of 3 minutes from DPR scan time. Also, the slope and correlation coefficient were observed to be highest for these cases (see figure 22a). Matches with weather radar scan times occurring outside of this 3 minute range showed a decrease in slope and correlation coefficient (as observed in figure 22b). For case studies with a high wind speed, the correlation coefficient and slope were observed to decrease slower with increasing and decreasing time, respectively, with regard to DPR scan time. The term *best match*, i.e. between DPR and WR, will from hereon be used to refer to the "match" between the WR scan that shows the best correspondence to the respective DPR scan (i.e. least deviations and highest correlation).

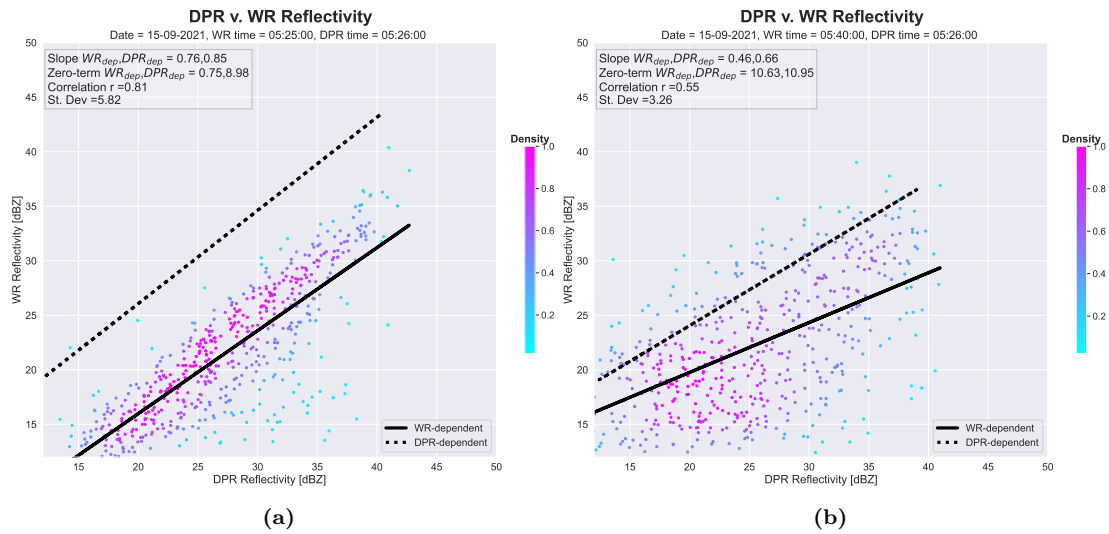


**Figure 22:** Density scatterplots of  $Z_{DPR}$  and  $Z_{WR}$  for case study R for varying WR scantimes: 05:25 UTC (left) and 05:40 UTC (right), with DPR scantime 05:26:00 UTC

#### 6.3.3.2 Scaling Influence

In figure 23, density scatter plots are shown for all *best matches* displaying the relationship between DPR reflectivity and WR reflectivity at equal grid points, for both the upscaled and downscaled data (in figure 23a and 23b, respectively). A positive, linear and relatively strong relationship is observed for both scaling choices and the correlation factors, equal to 0.72 and 0.73 for the upscaled and downscaled data, respectively, are similar. The regression line slopes with  $Z_{DPR}$  as the dependent variable are equal to 0.79 and 0.76 for the upscaled and downscaled data, respectively, and equal to 0.65 and 0.71 for  $Z_{WR}$  as the dependent variable. The regression line for  $Z_{WR}$  as a dependent variable appears to fit the data best from a visual point of view, as it matches the location of the highest density zone. The results for both scaling methods are thus relatively similar, indicating that the choice of scaling method isn't of high influence on the

correlation results. Based on this finding, only results based on the DPR grid will be displayed in the following section.

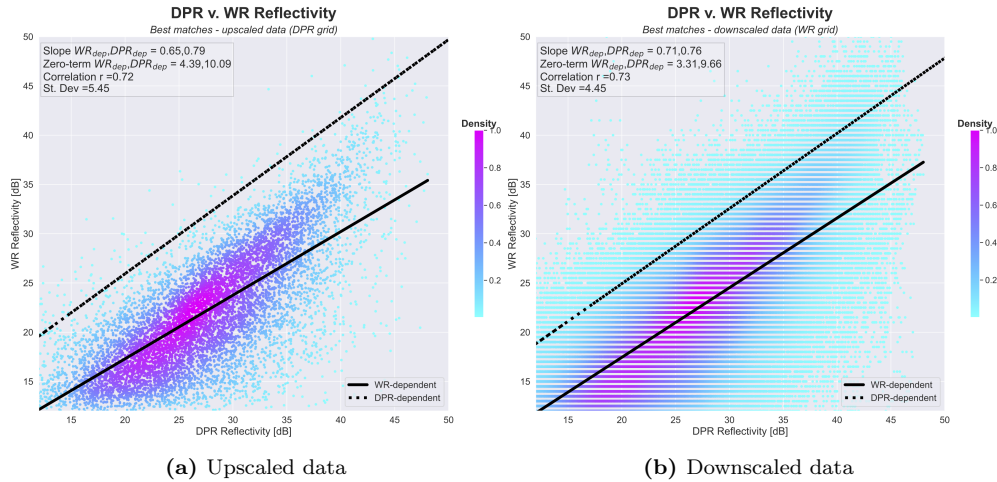


**Figure 23:** Density scatterplots of  $Z_{DPR}$  and  $Z_{WR}$  for all best matches using different scaling methods

### 6.3.3.3 Precipitation Type Influence

The relationship between  $Z_{WR}$  and  $Z_{DPR}$  was also analyzed with a distinction based on precipitation type, namely between stratiform and convective precipitation as depicted by the DPR algorithm per DPR measurement. All data from the best matches with a stratiform classification and with a convective classification are shown in figure 24a and figure 24b, respectively. The measurements for stratiform precipitation appear to be slightly better correlated, with a correlation coefficient equal to 0.7 with respect to 0.64 for convective precipitation. Furthermore, it was observed that all observations classified as convective are mostly approximately  $\geq 35$  dBZ, whereas the majority of the observations classified as stratiform have a reflectivity approximately  $\leq 35$  dBZ. This was expected based on the characteristics of each precipitation type as explained in chapter 2.

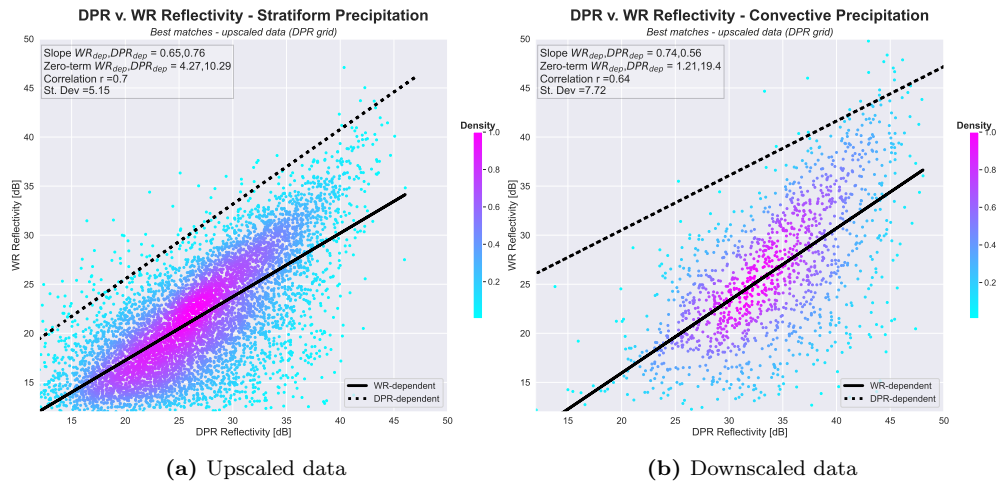


**Figure 24:** Density scatterplots of  $Z_{DPR}$  and  $Z_{WR}$  for all best-matched case study data sets for stratiform (left) and convective (right) precipitation

## 7 Discussion

This study has compared instantaneous Level 2A DPR-Ku products from the GPM constellation with surface data, namely a weather radar network and automatic gauge network, for high-intensity precipitation events over the Netherlands, to gain more insights into the relationship between spaceborne and surface data in both the temporal and spatial domain. The data were co-located and temporally matched, such that data presumably corresponding to the same precipitation event could be compared. The comparison of satellite measurements with surface measurements is not necessarily straightforward and many factors have to be considered, such as the differences in spatial resolution, temporal resolution, measurement technique, analyzed parameter, incorporated algorithms and altitude at which the measurements are made. These varying characteristics are bound to result in differences in each measurement technique's final product and thus to difficulties when comparing the measurements directly. The results of this study showed overall positive relationships with regard to similarities in the spatial and temporal domain of both reflectivity (DPR and weather radar) and precipitation intensity measurements (rain gauge) for severe rainfall events, which will be further discussed in the following paragraphs. First, the results from the comparison study of DPR with gauge observations will be discussed. Next, the findings from the reflectivity relations between the DPR product and the weather radar products will be elaborated on.

### 7.1 Gauge and DPR Relations

The precipitation performance metrics showed that for measurements of overall precipitation ( $\geq 0.5$  mm/h) the DPR precipitation product corresponds well in time to the gauge measurements, as the POD is highest with a time lag equal to 0 and decreases with an increased time lag. For high-intensity precipitation, the POD was relatively low, indicating that the capability of DPR to predict high-intensity precipitation is low with respect to the gauge's observations. It should be noted however that in general less high-intensity events occurred with respect to the 0.5 mm/h threshold and thus less data is incorporated in the POD determination for the threshold of 15 mm/h, and the result is, therefore, more prone to errors/bias. This gives way to an unfair comparison between the two resulting PODs and thus the performance of the DPR with respect to both thresholds. Another explanation for the low POD for the 15 mm/h threshold is that the DPR precipitation product is corrected for attenuation, and its attenuation correction algorithm is known for underperformance in heavy precipitation (Biswas and Chandrasekar, 2018). This could thus lead to underestimations of the 15 mm/h threshold and lower detection performance of DPR compared to gauge observations, as was observed.

The analysis comparing the DPR reflectivity data at 2000 m altitude with the surface gauge and weather radar data showed relations in both space and time for reflectivity zones  $\geq \pm 35$  dBZ and surface intensity observations  $\geq 15$  mm/h within a 40-minute time range for most analyzed case studies. It was observed that all HI-WS were located near a high reflectivity zone oriented towards the wind direction. Therefore, it could be assumed that the movement of high-reflectivity zones is directly affected by the wind direction. This was supported by the spatial shifts of reflectivity zones observed in consecutive weather radar scans. In all analyzed examples, the following was observed with regard to gauge observations coinciding with DPR-scan time. If the average observed intensity during an interval was equal to 0 mm/h, it was observed that the respective weather station was not located in a high reflectivity zone. Furthermore, if a relatively low precipitation intensity was observed by a weather station, the respective DPR scan showed the reflectivity at the location of the weather station to always be  $> 0$  dBZ.

The calculations to determine the time lag based on wind speed and direction from the high reflectivity zone location towards the HI-WS showed good resemblances to the actually observed

time lags for several of the analyzed events. Therefore, the assumption can be made that, for the circumstances in this study, instantaneous DPR Level 2A reflectivity measurements can be related to high-intensity observations on the surface by incorporating wind speed and direction and by considering a drop radius of minimally 0.25 and maximally 2.5 mm. However, as only instantaneous DPR measurements were available, storm behaviour was challenging to identify, and thus led to many uncertainties in this analysis. Small deviations in actual and calculated time lag could be related to the following factors.

Firstly, the influence of the raindrop's terminal velocity. Assumptions were made on the raindrop's radius range being between 0.25 and 2.5 mm, which results in specific terminal velocities, which in turn influence the travel time. A different terminal velocity would lead to a decrease or increase in vertical travel time. The results showed that when adding the drop-time to the horizontal travel time, the calculated time lag coincided well with the timing of the HI-interval for most cases. However, the exact size of the precipitation particles is unknown, and therefore uncertainties remain on which drop size to use for the terminal velocity calculation and whether the actual drop size would result in correct timelags as well. Secondly, the effect of the selected location of the to be considered a high reflectivity zone. This selection was based on the highest reflectivity value within a certain high reflectivity zone. However, if a pixel closer to or further from the HI-WS is considered, a decrease or increase, respectively, in both distance and time-lag would be the result. Thirdly, the windspeed naturally has a great effect on the calculated time-lag. The wind speed implemented in the calculations is from a specific altitude, namely 2500 meters, as no winddata was available at 2000 m altitude. Therefore, it should be considered that the wind speed at 2000 m could differ from the wind speed at 2500 m. Furthermore, the credibility and accuracy of the used wind data is of course a critical factor. As the wind data used in this research is based on a model, and are not direct measurements, a certain level of uncertainty has to be taken into account. Fourthly, it should be considered that, in certain cases, during the interval prior to or after the HI-interval, high-intensity precipitation was actually already occurring although an intensity  $< 15$  mm/h is recorded. Such intervals show to have recorded non-zero rainfall for a shorter duration than the 10-minute interval, for instance in case study Q. From the gauge data, it was observed that the interval before the HI-interval recorded rainfall for 192 sec at 10 mm/h. Converting the 10 mm/h back to the amount measured in the 10-minute interval leads to 1.66 mm/10 minutes. The time in which that precipitation amount was actually recorded was 192 sec. Converting that to an average intensity per hour results in 31.25 mm/h, which is considerably higher than the averaged 10 mm/h provided as representative for that 10-minute interval. Hence, the HI-interval actually started sooner. The actual time lag could thus be a few minutes shorter or longer when such short high intensity durations are considered, instead of just considering the time lag with respect to the averaged HI-interval. Lastly, account must be taken of the aforementioned highly dynamic nature of precipitation systems. Between the DPR scan time and the preceding or succeeding passing of a HR zone over the respective HI-WS, many factors could have influenced the local storm system (e.g. wind speed or temperature changes), such that the observations at DPR scan time are no longer applicable. This applies most of all to DPR scans with a large time lag between the HI gauge measurement.

### 7.1.1 Deviating Observations

In some of the analyzed cases, a direct relationship could not be found between present HR-zones and a HI-WS regarding wind direction and wind speed. This can be explained by multiple factors, among which is the duration between the DPR-scan time and the time of the observed rainfall (also denoted by *a time lag* in the previous sections). Storms have a highly dynamic nature and are influenced by many factors. Thus, in time, the characteristics of a storm, and therefore the observations made of that respective storm (i.e. reflectivity), will evolve as well. Consequently, a larger time lag between the two types of measurements will lead to more

uncertainties with regard to the storm's behaviour. As a result, there can be less confidence in the assumption that a specific observation from a DPR scan can be related to the behaviour observed on the ground by a weather station. For example, if the DPR scan occurs prior to the HI-interval and the time lag is ample, it could be that the storm still has to initiate and thus no notable relating reflectivity observations are yet present in the DPR scan. Equally so, if the DPR scan occurs much later than the HI-interval. Then, it could be that the storm has already dissipated and thus no notable relating reflectivity observations are longer present in the DPR scan. In some of the analyses, namely case studies K and R, the locations of the HR-zone movement and the HI-WS could not be related to the wind direction at 2000 meters. It was found that wind directions at a higher altitude did seem to agree with the movement direction. The fact that the storm movement seemed to be affected by a wind direction at a relatively higher altitude, could have to do with the respective storm height. It was found that in those cases, the storm height indeed corresponded with the altitude at which a wind direction agreeing with the HI-WS's direction was measured. Furthermore, the calculated time lag of some case studies did not correspond well with the observed time lag (i.e. a deviation of  $\geq 5$  minutes from the observed interval). Also, in multiple case studies, weather stations are observed in high reflectivity zones without recording precipitation intensity intervals of  $\geq 15$  mm/h. Multiple arguments can be given for these observations, among which is the choice of time range used in the analysis. For example, when regarding case study G, multiple weather stations are located either in high reflectivity zones (such as *Berkhout*) or nearby them in the same direction as the wind (such as *Schiphol locatie 18Ct* and *Stavoren*). The gauge datasets show high-intensity records at those stations, outside the selected 40-minute time range. It should be noted that in this particular example, the wind speed is relatively low. Therefore, the assumption can be made that with a very low wind speed a longer time range can be used to accurately relate high-reflectivity zones and HI-intervals with the wind direction. Another explanation for the absence of HI-WS in or near high-reflectivity zones is faulty recordings at the respective weather station, thus resulting in null measurements when precipitation actually does occur.

## 7.2 WR and DPR Relations

The reflectivity products from both weather radar and DPR were compared in both space and time for all case studies. If assumed that there is no or minimal delay between the timing of the DPR and weather radar, then it would be expected to see similar reflectivity values in each respective scan and thus small deviations in the deviations maps. Subsequently, it was expected that a larger time difference between the DPR and WR scan time would lead to larger reflectivity deviations, as during that respective time difference the potentially present storm system would have developed and potentially moved, therefore the reflectivity value measured at a specific pixel in a WR-scan would have changed with respect to the former WR-scan. This assumption was confirmed by results from the scatterplots, deviation maps and correlation factors from the reflectivity comparison study, as an increase in deviations and a decrease in slope and correlation factor were observed with increasing time lag for all case studies (see Appendix B), thereby indicating that reflectivity observations of both datasets correspond best when the weather radar scan time is relatively close to DPR scan time (i.e. either the WR interval before/after or coinciding with DPR scan time, as long it's in a  $\pm 3$ -minute range). Furthermore, as was expected, case studies with a relatively high wind speed showed a much faster decrease in correlation with increasing time lag.

### 7.2.1 Deviating Observations

In the best corresponding deviation maps (hereafter referred to as *best matches*), the deviations were on average approximately + 8 dBZ. Such a difference in magnitude is logical, as the radars' products are based on different techniques (and therefore affected by different processes, for instance by horizontal and vertical attenuation for WR and DPR, respectively) and the measurements are compared from different altitudes (1500 m and 2000 m for WR and DPR, respectively). Apart from these standard deviations, zones with relatively high deviations (i.e.  $\geq + 20$  dBZ) were observed in the deviation maps of some of the case studies' best matches. This indicated that there were factors causing variations in space. These high deviation zones could be divided into two subcategories: small-scale high deviation zones and large-scale high deviation zones. For each of the two subcategories, different factors were assumed to be the cause:

The small-scale high deviations were observed at several locations of HR zones in both WR and DPR maps, in between relatively low reflectivity deviation zones in the deviation maps (a good example is visible in case study N). These observations could be related to the difference in spatial resolutions of the data sets and to the fact that the DPR data had been interpolated to the WR grid using a linear interpolation method. The higher spatial resolution of WR causes more small-scale variability in precipitation processes to be taken into account in the reflectivity product and thus provides multiple reflectivity products within the scale of the DPR footprint, which in turn only provides one reflectivity product. Previous research showed that for high-intensity precipitation processes, small-scale variability is expected within the scale of a DPR footprint (i.e.  $\pm 20 \text{ km}^2$ ). Therefore, it is a logical result that within that respective area, variations in reflectivity between DPR and WR are observed. Furthermore, the choice of interpolation technique played a role in the spatial distribution of the DPR data used in the deviation determinations. Linear interpolation causes the DPR value on a specific WR grid point to be predicted, based on the distance between neighbouring DPR footprints. Therefore, the DPR reflectivity products used for the deviations are not accurately representative of the raw DPR products but have been altered based on their location. Another interpolation method (like kriging) would cause different and perhaps improved results.

The occurrence of large-scale high deviation zones was analyzed per case study and based on these analyses, it was found that possible causes are weather radar attenuation and spatial expansion of the weather radar beam. Weather radar attenuation can occur in situations where many and/or large storm systems are present and prevents the radar from detecting any precipitation cells behind the first storm, as the first storm has already absorbed (a large part of) the radar signal. Thus, no pulses are emitted back towards the radar and hence, no (high) reflectivity is visible in the radar product, in regions where high precipitation actually does occur. This phenomenon may have caused the occurrence of large-scale high deviation zones, as observed in case studies A, D, E, F, and K, where it is observed that the DPR detects a high reflectivity zone behind another high reflectivity zone, whereas the WR only detects the first one. Some of the high deviation zones were located relatively far from the locations of the weather radars (i.e.  $\geq 150$  km). This could be related to the fact that the radar's beam range is limited. The radar's observations are representative of observed particles at 1500 m altitude within a range of about 120 km. However, for a range larger than 120 km, the beam is affected by the curvature of the Earth, which results in its measurements being representative of a higher altitude (Wessels, 2006). Therefore, the high deviations at a larger range (as seen in case studies E, F, and G) may have been the result of this radar range limitation, as the deviations occur at a distance of approximately more than 120 km from the closest weather radar.

### 7.3 Reflection

Prior research showed overall good agreement between precipitation estimates from DPR Ku-band and gauge of weather radar precipitation observations. Some of the research was done in mountainous areas, which subsequently led to lower PODs. This research showed a resemblance in precipitation performance to research by Lasser and Foelsche (2018), with a POD of 0.75 and a range of 0.7-0.9 in their and this study, respectively. In comparison to research by Kidd et al. (2017), the POD in this research was relatively high. As in this study, research by Biswas and Chandrasekar (2018) focused on reflectivity relations between DPR and weather radar. Their correlation results corresponded well with the results of this research, as they determined a maximum correlation of 0.9 for DPR and weather radar reflectivities in comparison to a correlation factor of 0.875 in this study. In general, previous studies showed that DPR underestimates high-intensity precipitation, which was confirmed by the precipitation performance metrics for a threshold of 15 mm/h in this study.

## 8 Conclusions and Recommendations

In this research, high-quality surface datasets produced by a weather radar network and automatic rain gauge network have been used to compare Dual-frequency Precipitation Radar Level 2A Ku reflectivity data from the GPM Core Observatory satellite in the spatial and temporal domain for high-intensity precipitation surface observations over the Netherlands. In this chapter, final conclusions and recommendations based on the results of this study will be given.

### 8.1 Key Findings

This research aimed to identify how rainfall estimates from a gauge network and weather radar network on the surface relate to the estimates from the GPM DPR for high-intensity rainfall events. Based on both a quantitative and qualitative analysis using both direct and indirect precipitation estimates (precipitation intensity and reflectivity, respectively), the research questions as posed in the introductory chapter of this research can be answered and conclusions can be made regarding relations between DPR and WR and between DPR and gauge observations.

Based on the comparisons of DPR and WR reflectivity products, it can be concluded that instantaneous DPR reflectivity estimates at 2000 meters altitude show a positive relation in time and space with WR reflectivity composited at 1500 meters altitude. Reflectivity comparisons of co-located WR and DPR reflectivities showed that the two reflectivity products show the highest correlation and least deviations with the littlest time lag (namely 3 minutes or less) between the two measurements, indicating that the products of both radars are well related in both the spatial and temporal domain. The DPR products constantly produce higher reflectivity estimates, with an average of approximately 5 dBZ for all best-related WR products. Furthermore, noticeable differences in reflectivity were observed at relatively large distances from the weather radar network and in areas of multiple high reflectivity zones. At these locations, DPR reflectivities were remarkably higher than WR reflectivities (i.e. differences equal to or larger than 20 dBZ), caused by attenuation and overshooting of the WR beam. From the analyses of DPR reflectivity products with high-intensity gauge observations, the conclusion can be drawn that instantaneous reflectivity measurements equal to approximately 35 dBZ or higher can be related to (relatively) heavy precipitation events within at least a 30-minute range from DPR scantime, by incorporating wind speed, wind direction and terminal drop velocities ranging from approximately 3 - 10 m/s. In case of very low wind speeds and storm systems of less dynamic nature, a larger temporal range can be used for which relations can still be found. In case of highly dynamic storms and high wind speeds, smaller temporal ranges are advised for relating DPR to surface precipitation. Based on these findings, and the performance analysis of precipitation products, it can be concluded that DPR products show no obvious spatial and temporal lag with respect to surface precipitation measurements.

The main research question of this thesis can be answered as follows. It can be concluded that instantaneous DPR reflectivity products at 2000 meters altitude can be directly related to gauge precipitation estimates at the surface for a minimum temporal range of 30 minutes from DPR scantime, equal to or higher than 15 mm/h, by incorporating local wind characteristics and precipitation dynamics. In case of relatively low windspeed (and stable storm dynamics) or high wind speed (and highly fluctuating storm dynamics), a respectively higher and lower temporal range than 30 minutes from DPR scantime should be implemented for accurate analysis. With regard to DPR and WR reflectivity products, it can be concluded that the two products relate best to one another when DPR scantime is within a range of maximally 3 minutes from WR scantime.

## 8.2 Limitations

There are two main limitations in this study. The first limitation has to do with the different characteristics of the measuring techniques and their products that were used in this research, such as varying geometries, spatial resolutions, temporal resolutions and measurement altitudes. These differences may have led to possible inaccuracies and errors when making direct data comparisons. A second limitation of this research is the difference in the amount of human processing steps that were incorporated in both reflectivity products. The aim of this research was to make use of precipitation estimates that were relatively unprocessed. The WR composite products were however corrected for attenuation, and thus more prone to human errors, whereas the DPR reflectivity products were not.

## 8.3 Outlook

The findings of this study showed that instantaneous measurements made by the DPR on board the GPM Core Observatory satellite can be spatially and temporally related to precipitation observations at the surface and that a positive relationship in time and space was found with weather radar observations. These findings can be of use for the scientific community, and eventually for society, as predictions can be made of the timings and locations of precipitation events by use of DPR reflectivity and wind data. If the temporal resolution of the DPR, or an alike device, were to improve such that continuous observations were made, precipitation information will become available on a global scale and thus aid regions where surface rainfall measurements are not possible.

## 8.4 Future Research

To further analyze the temporal and spatial relations of DPR products with surface measurements, a few items are recommended for further research.

Two items are recommended for future research with respect to the methodology of this research. Firstly, this research could be performed using different interpolation techniques for resampling the data, such as the relatively more complex kriging method. This could lead to a more realistic representation of the original data and thus to different results than by use of linear interpolation, as was used in this study. Secondly, the terminal drop velocities used to calculate the vertical time lags in section 5.3.2.1 were simplified and generalized for all situations based on an average minimum and maximum raindrop size. For a more accurate analysis, it would be recommended to derive the terminal drop velocities by dividing the observed gauge precipitation intensity by the third moment of the drop size distribution, which can be based on estimated for the location of interest.

A recommendation concerning the choice of data-sets is the following. As stated in section 8.2, a limitation of this research concerning the preferred usage of products with as few human alterations as possible, is that WR reflectivity composite products were used instead of the raw volume data products. In research following up on this study, it would be recommended to make use of volume data reflectivity products. Another advantage of using those instead of the composite data is that reflectivities at multiple altitudes (from different elevation angles) can be extracted, instead of being restricted to an altitude of 1500 meters.

Recommendations for further specifying and deepening the results, it would be recommended to perform this research for multiple locations with varying meteorological characteristics, to observe whether climate and geographical location are of influence on the results. Also, the methodology of section 5.3.1.3 could be performed for high-reflectivity zones situated near weather stations that do not record any high-intensity precipitation (i.e. a form of reversed analysis with respect to the focus of this study).

## References

- Battaglia, A., Kollias, P., Dhillon, R., Roy, R., Tanelli, S., Lamer, K., Grecu, M., Lebsock, M., Watters, D., Mroz, K., Heymsfield, G., Li, L., and Furukawa, K. (2020). Spaceborne cloud and precipitation radars: Status, challenges, and ways forward. *Reviews of Geophysics*, 58.
- Beek, R. v. d. (2013). *Rainfall variability in the Netherlands from radars, rain gauges, and disdrometers*. PhD thesis.
- Berndtsson, R. and Niemczynowicz, J. (1988). Spatial and temporal scales in rainfall analysis — some aspects and future perspectives. *Journal of Hydrology*, 100:293–313.
- Biswas, S. K. and Chandrasekar, V. (2018). Cross-validation of observations between the GPM dual-frequency precipitation radar and ground based dual-polarization radars. *Remote Sensing*, 10.
- Brandsma, T. (2014). KNMI Technical Report: Comparison of automatic and manual precipitation networks in the Netherlands.
- Calkins, K. G. (2005). Introduction to statistics.
- Coz, C. L., Heemink, A., Verlaan, M., and van de Giesen, N. (2021). Spatial and time warping for gauge adjustment of rainfall estimates. *Atmosphere*, 12.
- Coz, C. L. and van de Giesen, N. (2020). Comparison of Rainfall Products over Sub-Saharan Africa. *Journal of Hydrometeorology*, 21.
- Fiener, P. and Auerswald, K. (2009). Spatial variability of rainfall on a sub-kilometre scale. *Earth Surface Processes and Landforms*, 34:848–859.
- Gabella, M., Speirs, P., Hamann, U., Germann, U., and Berne, A. (2017). Measurement of precipitation in the alps using dual-polarization c-band ground-based radars, the gpm-spaceborne ku-band radar, and rain gauges. *Remote Sensing*, 9.
- Holleman, I. (2001). Hail detection using single-polarization radar.
- Houze, R. A. (2014). *Cloud Dynamics*.
- Iguchi, T., Seto, S., Meneghini, R., Yoshida, N., Awaka, J., and Kubota, T. (2010). GPM/DPR Level-2 Algorithm Theoretical Basis Document.
- IPCC (2021). *IPCC, 2021: Summary for Policymakers. Climate Change 2021: The Physical Science Basis. Contribution of Working Group I to the Sixth Assessment Report of the Intergovernmental Panel on Climate Change*. The Intergovernmental Panel on Climate Change.
- JAXA (2018). *GPM Data Utilization Handbook*.
- Jensen, N. E. and Pedersen, L. (2005). Spatial variability of rainfall: Variations within a single radar pixel. *AtmRe*, 77:269–277.
- Kidd, C., Becker, A., Huffman, G. J., Muller, C. L., Joe, P., Skofronick-Jackson, G., and Kirschbaum, D. B. (2017). So, how much of the Earth’s surface is covered by rain gauges? *Bulletin of the American Meteorological Society*, 98:69–78.
- Kidd, C., Tan, J., Kirstetter, P. E., and Petersen, W. A. (2018). Validation of the Version 05 Level 2 precipitation products from the GPM Core Observatory and constellation satellite sensors. *Quarterly Journal of the Royal Meteorological Society*, 144:313–328.

- KNMI (2000). Handbook for the Meteorological Observation.
- Krajewski, W. F., Ciach, G. J., and Habib, E. (2003). An analysis of small-scale rainfall variability in different climatic regimes. *Hydrological Sciences Journal*, 48.
- Lasser, M. and Foelsche, U. (2018). Evaluation of GPM-DPR precipitation estimates with Wegenernet gauge data.
- NASA (2017). README Document for the GPM Data.
- Overeem, A. (2009). Climatology of extreme rainfall from rain gauges and weather radar.
- Overeem, A., Leijnse, H., and Uijlenhoet, R. (2011). Measuring urban rainfall using microwave links from commercial cellular communication networks. *Water Resources Research*, 47:12505.
- Pedersen, L., Jensen, N. E., Christensen, L. E., and Madsen, H. (2010). Quantification of the spatial variability of rainfall based on a dense network of rain gauges. *Atmospheric Research*, 95:441–454.
- Peleg, N., Ben-Asher, M., and Morin, E. (2013). Radar subpixel-scale rainfall variability and uncertainty: Lessons learned from observations of a dense rain-gauge network. *Hydrology and Earth System Sciences*, 17:2195–2208.
- Petracca, M., D’Adderio, L. P., Porcù, F., Vulpiani, G., Sebastianelli, S., and Puca, S. (2018). Validation of GPM Dual-Frequency Precipitation Radar (DPR) rainfall products over Italy. *Journal of Hydrometeorology*, 19:907–925.
- Sokol, Z., Szturc, J., Orellana-Alvear, J., Popová, J., Jurczyk, A., and Céleri, R. (2021). The role of weather radar in rainfall estimation and its application in meteorological and hydrological modelling—a review. *Remote Sensing*, 13:351.
- Speirs, P., Gabella, M., Berne, A., Speirs, P., Gabella, M., and Berne, A. (2017). A comparison between the GPM Dual-Frequency Precipitation Radar and Ground-Based Radar Precipitation Rate Estimates in the Swiss Alps and Plateau. *JHyMe*, 18:1247–1269.
- Syed, K. H., Goodrich, D. C., Myers, D. E., and Sorooshian, S. (2003). Spatial characteristics of thunderstorm rainfall fields and their relation to runoff. *Journal of Hydrology*, 271.
- Tan, J., Petersen, W. A., Kirchengast, G., Goodrich, D. C., and Wolff, D. B. (2018). Evaluation of global precipitation measurement rainfall estimates against three dense gauge networks. *Journal of Hydrometeorology*, 19:517–532.
- University of Texas Institute for Geophysics (2022). Radar Principles.
- Wessels, H. (2006). KNMI Radar Methods. *KNMI Technical Report*.

## A Data Details

Item	Value
Swath Width	245 kilometers (km)
Range Resolution	250 meters (m)
Spatial Resolution	5 km (Nadir)
Beam Width	0.71 degrees
Transmitter	128 Solid State Amplifiers
Peak Transmit Power	1013 Watts (W)
Pulse Repetition Freq.	4100 to 4400 Hertz
Pulse Width	two 1.667 microseconds ( $\mu$ s) pulses
Beam Number	49

**Table A.1:** DPR Ku-Band specifications

	STORM Setting
<b>Data Type</b>	2a
<b>Algorithm</b>	2aKu
<b>Satellite</b>	GPM
<b>Instrument</b>	DPR
<b>Time Range</b>	01/05/2018 - 30/09/2020 excl. months 1, 2, 3, 4, 10, 11, 12
<b>Geographical area boundaries</b>	N-lat: 53.6482, S-lat: 50.6539 E-lon: 7.3416, W-lon: 2.81

**Table A.2:** GPM DPR download specifications from STORM

Number	Station Name	Latitude	Longitude
1	Arcen	51.497	6.196
2	Berkhout	52.643	4.979
3	Cabauw locatie A	51.969	4.926
4	De Bilt testlocatie A	52.100	5.183
5	De Kooy waarneemterrein	52.927	4.781
6	Deelen locatie obs02t	52.055	5.872
7	Eelde locatie 23t	53.124	6.585
8	Eindhoven locatie obs22t	51.450	5.377
9	Ell	51.197	5.762
10	Gilze-Rijen locatie 10t	51.565	4.935
11	Heino	52.434	6.259
12	Herwijnen	51.858	5.145
13	Hoek van Holland	51.991	4.122
14	Hoogeveen	52.749	6.573
15	Hoorn Terschelling	53.391	5.346
16	Hupsel	52.068	6.657
17	Lauwersoog	53.412	6.199
18	Leeuwarden locatie obs24t	53.223	5.752
19	Lelystad locatie 23t	52.457	5.52
20	Maastricht locatie 22t	50.905	5.762
21	Marknesse	52.702	5.888
22	Nieuw Beerta	53.194	7.149
23	Rotterdam locatie 24t	51.961	4.447
24	Schiphol locatie 18Ct	52.317	4.790
25	Stavoren	52.897	5.383
26	Twenthe locatie A	52.273	6.891
27	Vlissingen	51.441	3.596
28	Volkel locatie obs24Rt	51.658	5.707
29	Voorschoten	52.140	4.436
30	Westdorpe	51.225	3.861
31	Wijk aan Zee	52.505	4.603
32	Wilhelminadorp	51.530	3.894
33	Woensdrecht locatie A	51.448	4.342

**Table A.3:** Overview of all weather stations within the study area that were used in this research, indicating station name, latitude and longitude

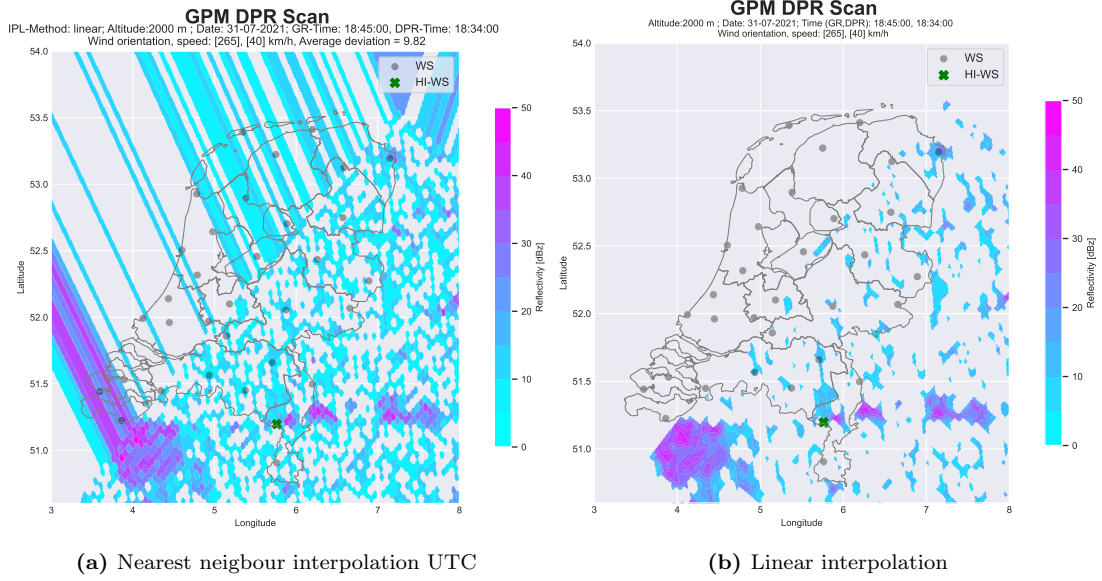


**Figure A.1:** DPR data interpolated to WR grid for case study N

## B Case Study Data

### Case Study A

Two stations in the automatic network measured a precipitation intensity  $\geq 15$  mm/h within a range of  $\pm 40$  minutes from DPR scan time: *Ell* recorded a peak intensity of 37.6 mm/h starting 34 minutes after DPR scan time and *Maastricht locatie 22t* recorded a peak intensity of 48.1 mm/h starting 4 minutes after DPR scan time. During scan time, *Ell* measures 0 mm/h and Maastricht  $\pm 11$  mm/h. In both DPR -and WR-scans, *Maastricht locatie 22t* is situated in an HR zone, whereas *Ell* is not. When moving perpendicularly from *WS Ell* against the wind direction in the DPR scan (towards the southwest), an HR zone is observed, which might correspond to the HI-peak observed after DPR scan time. The same is observed for *Maastricht locatie 22t*, but with a closer-by HR zone, which corresponds to the smaller timelag between DPR scan time and the start of the HI-interval.

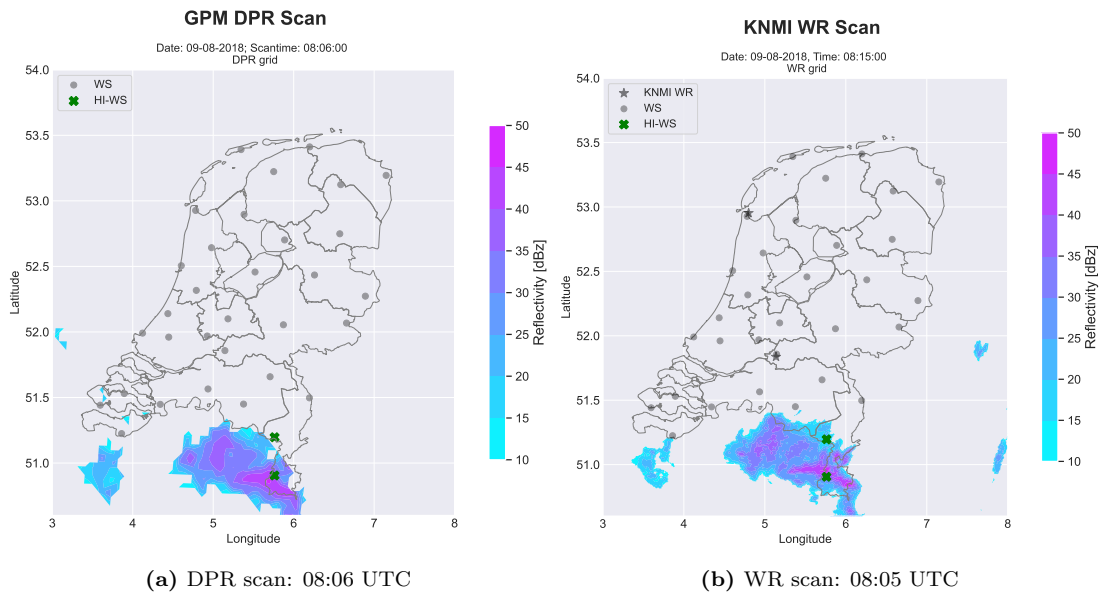
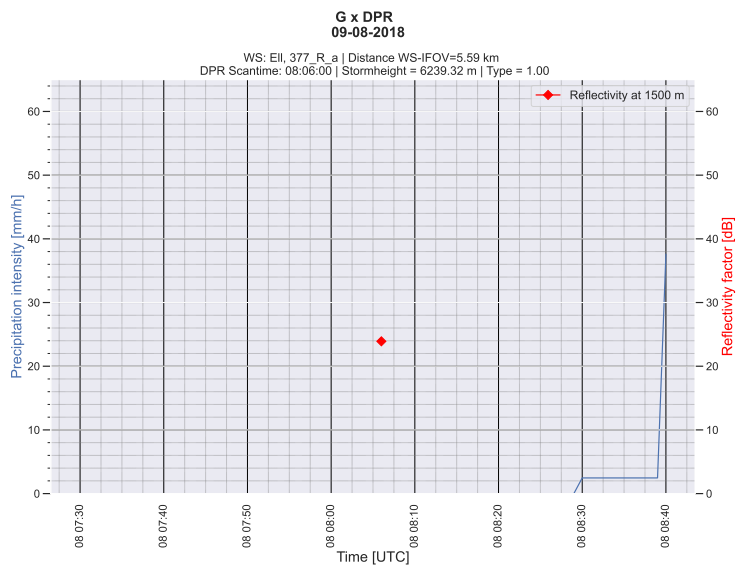
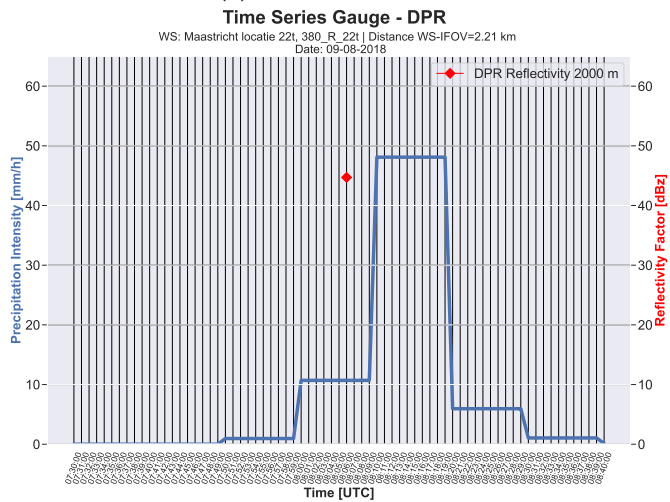


Figure B.1: DPR and WR scan for 09-08-2018; HI-measurement starting at 15:50 UTC



(a) Weather station: Ell



(b) Weather station: Maastricht locatie 22t

**Figure B.2:** Time series of HI-WS measurements within a range of  $\pm 40$  minutes from DPR scan time on 09-08-2018; the red check indicates the DPR reflectivity

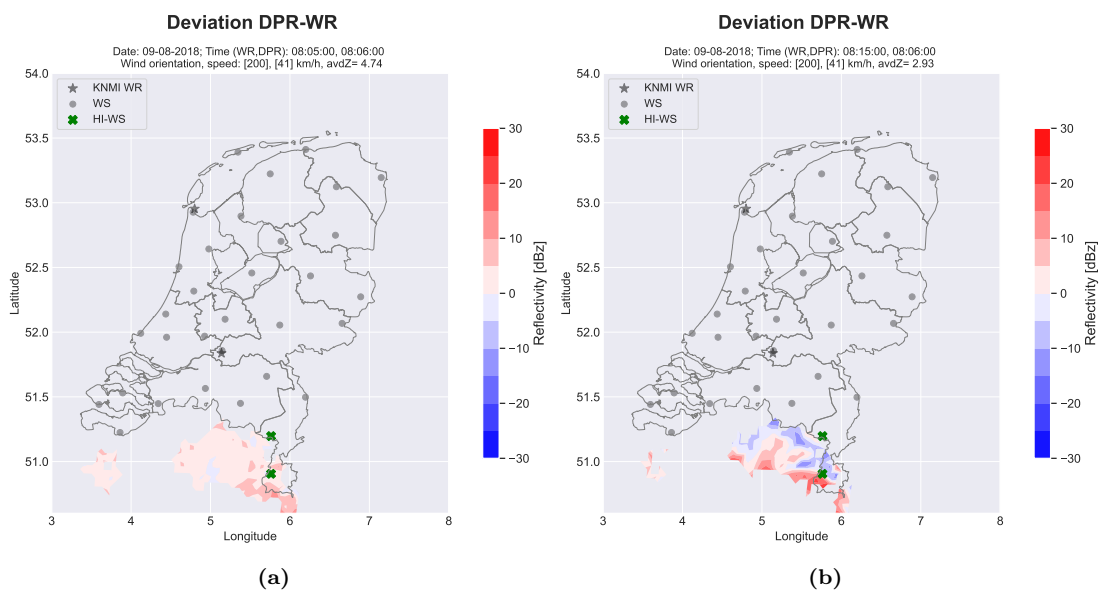


Figure B.3: DPR and WR scan for 09-08-2018; HI-measurement starting at 15:50 UTC

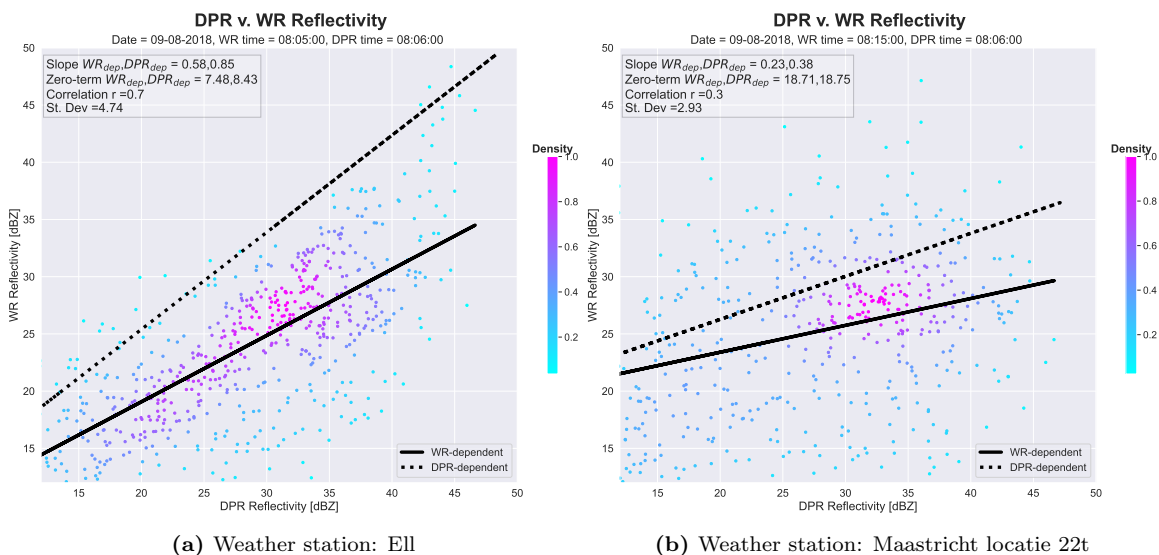


Figure B.4: Time series of HI-WS measurements within a range of  $\pm 40$  minutes from DPR scan time on 09-08-2018; the red check indicates the DPR reflectivity

### Case Study B

Within a  $\pm 40$  minutes range from DPR scan time on 23-08-2018, four weather stations recorded intervals with intensities  $\geq 15$  mm/h. Stations *Hoogeveen* and *Heino* are situated in an HR zone in both DPR and WR, whereas *Deelen locatie obs02t* and *Volkel locatie A* are located near HR zones. During scan time, *Deelen locatie obs02t* and *Volkel locatie A* observe no rainfall, whereas *Heino* observes a very low intensity of  $\pm 1$  mm/h. The HI-interval at *Hoogeveen* coincides with DPR scan time. During all 4 time series, singular high-intensity peaks are observed, which can be related to the small width of the HR zones. At 2000 m altitude, a southwesterly wind is observed. This direction corresponds to the timings of the HI-intervals of the different weather stations, as explained below. Furthermore, the movements observed in the WR scans align with the observed wind direction.

At scan time, an intensity of 0 mm/h is observed at *Volkel locatie A*. 16 minutes following scan time, a peak of 16.9 mm/h is observed. It can be assumed, regarding the wind orientation and speed, that the HR zone on the southwest of the corresponds to that particular peak.

At scan time, an intensity of 0 mm/h is observed at *Deelen locatie obs02t*. 25 minutes prior to scan time, a peak of 16 mm/h is observed. It can be assumed, regarding the wind orientation and speed, that the HR zone northeast of the HI-WS corresponds to that particular peak.

At *Heino*, scan time occurs 5 minutes before the start of the HI-interval. During scan time, very low intensity is observed. The HI-WS is located at the edge of a HR region, with the centre of the HR-region southwest of the station. Again, this region is therefore assumed to correspond to the observed peak.

The fourth station, *Hoogeveen*, measures a HI interval during scan time. This corresponds to the DPR scan, in which the HI-WS is situated within an HR zone.

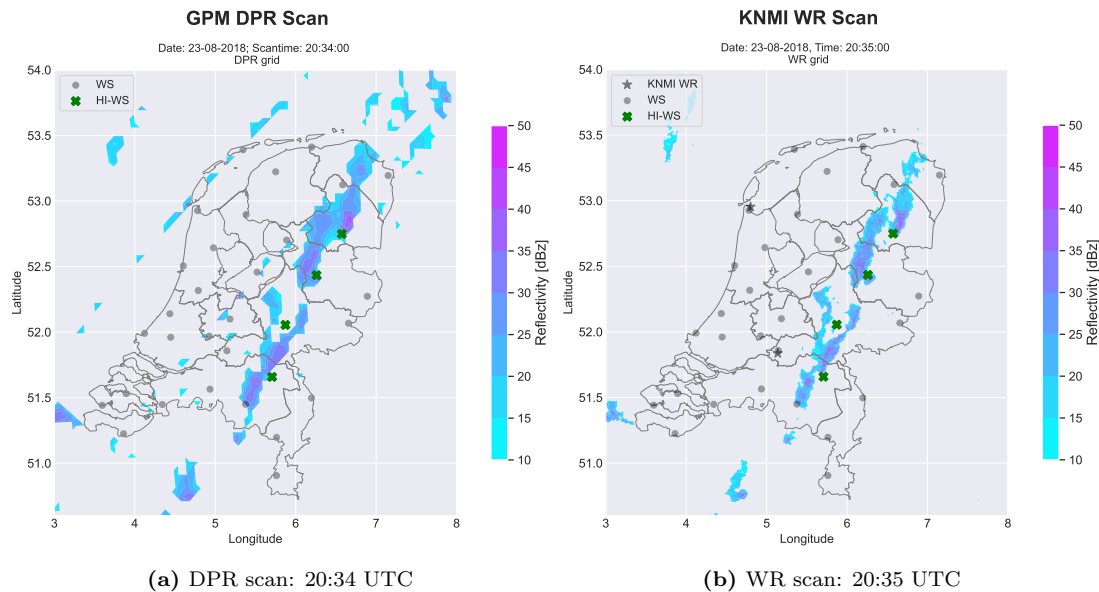
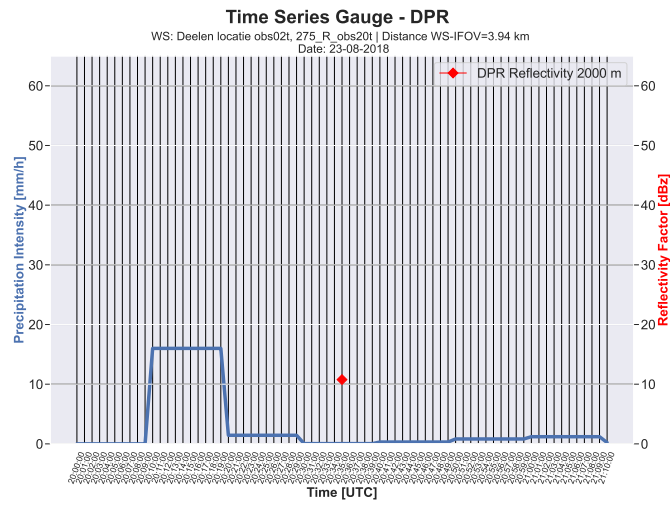
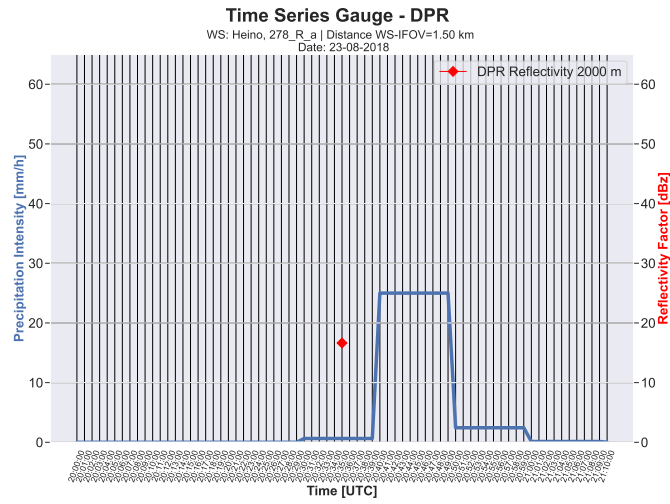


Figure B.5: DPR and WR map for 23-08-2018



(a) Weather station: Deelen



(b) Weather station: Heino

**Figure B.6:** Time series of HI-WS measurements within a range of  $\pm 40$  minutes from DPR scan time on 23-08-2018; the red check indicates the DPR reflectivity

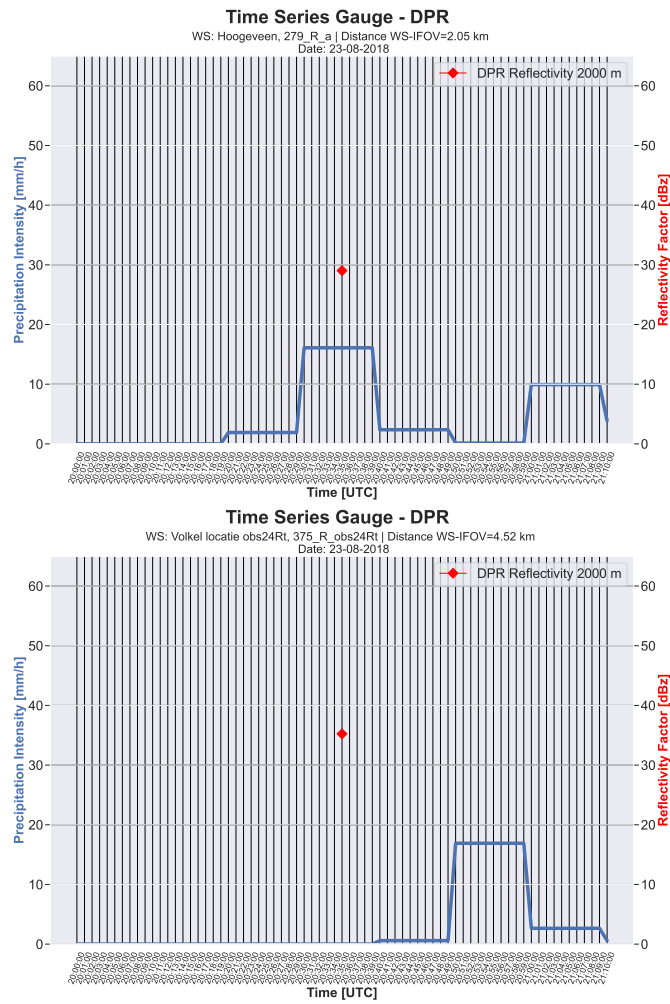


**Figure B.7:** Time series of HI-WS measurements within a range of  $\pm 40$  minutes from DPR scan time on 23-08-2018; the red check indicates the DPR reflectivity

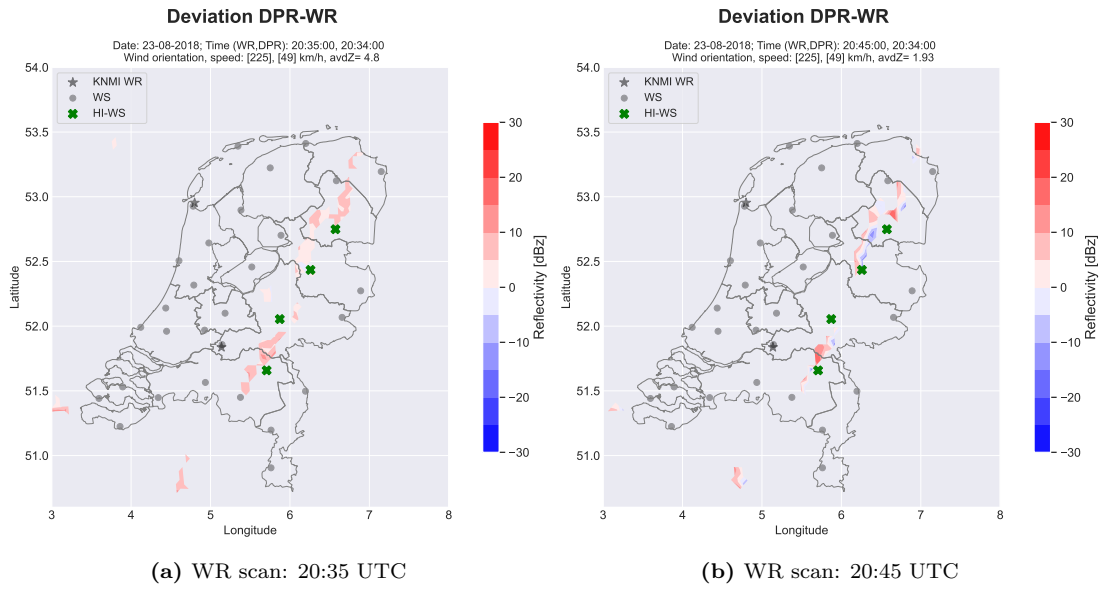


Figure B.8: Reflectivity deviation scans of DPR and WR scans on 23-08-2018

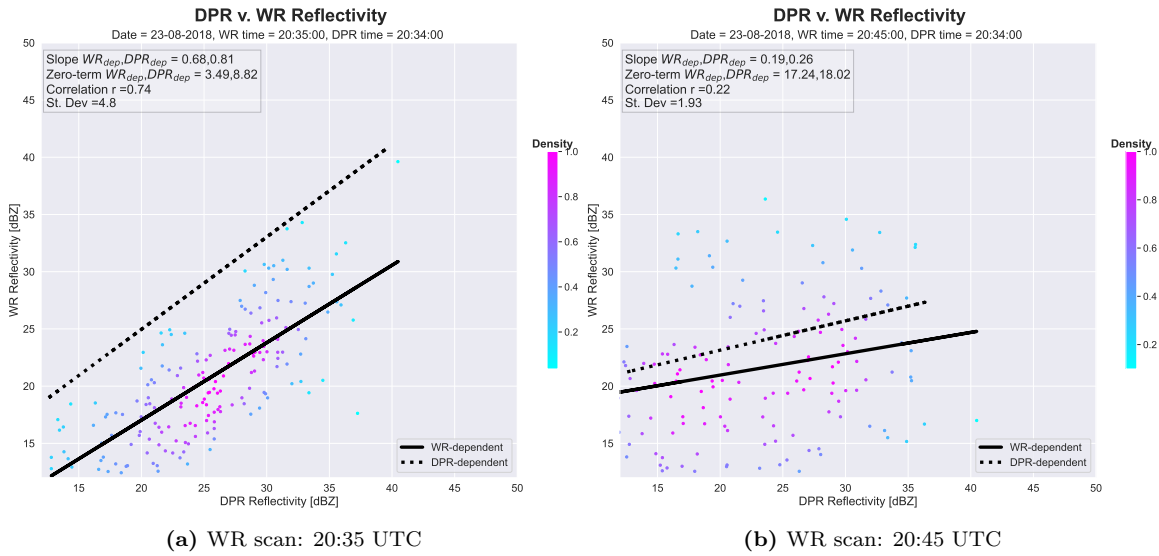
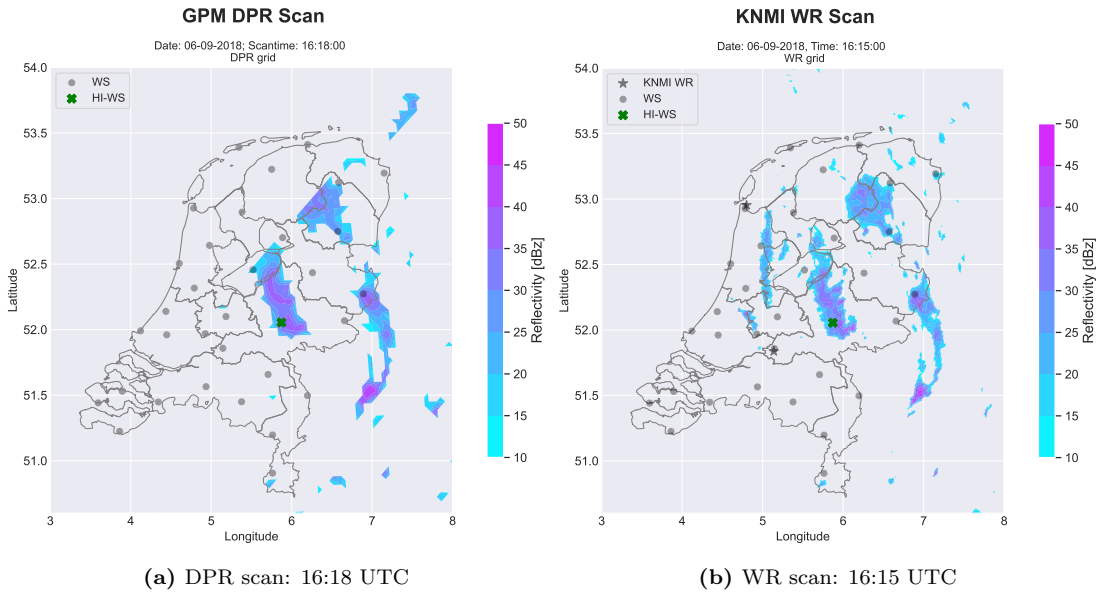


Figure B.9: Density scatter plots of  $Z_{DPR}$  and  $Z_{WR}$  on 23-08-2018

**Case Study C**

A HI-WS measurement is observed starting 29 minutes prior to the GPM scan time with a peak intensity of 22 mm/h. After the HI-measurement, lower intensity peaks follow (ca. 4 mm/h at scan time). The HI-WS is situated in an HR zone, in both DPR -and WR observations. The consecutive WR scans show the HR region moving in the wind direction at 1500 m. Moving perpendicularly from the HI-WS in the wind direction, HR zones are observed, possibly relating to the HI-measurement.



**Figure B.10:** DPR and WR map for 06-09-2018

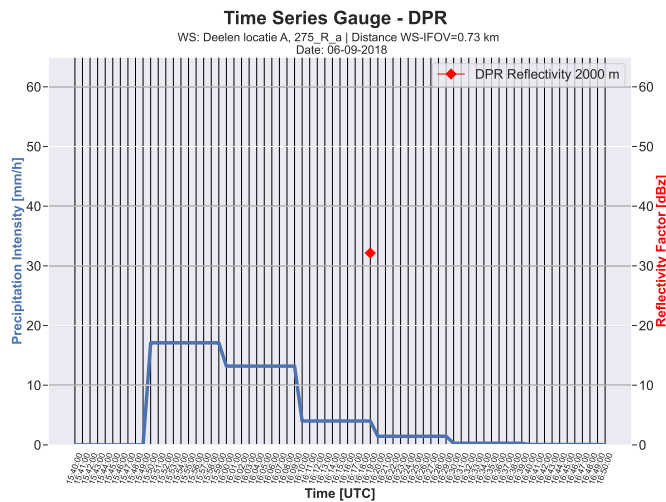


**Figure B.11:** Time series of HI-WS measurements on 06-09-2018; the red check indicates the DPR reflectivity

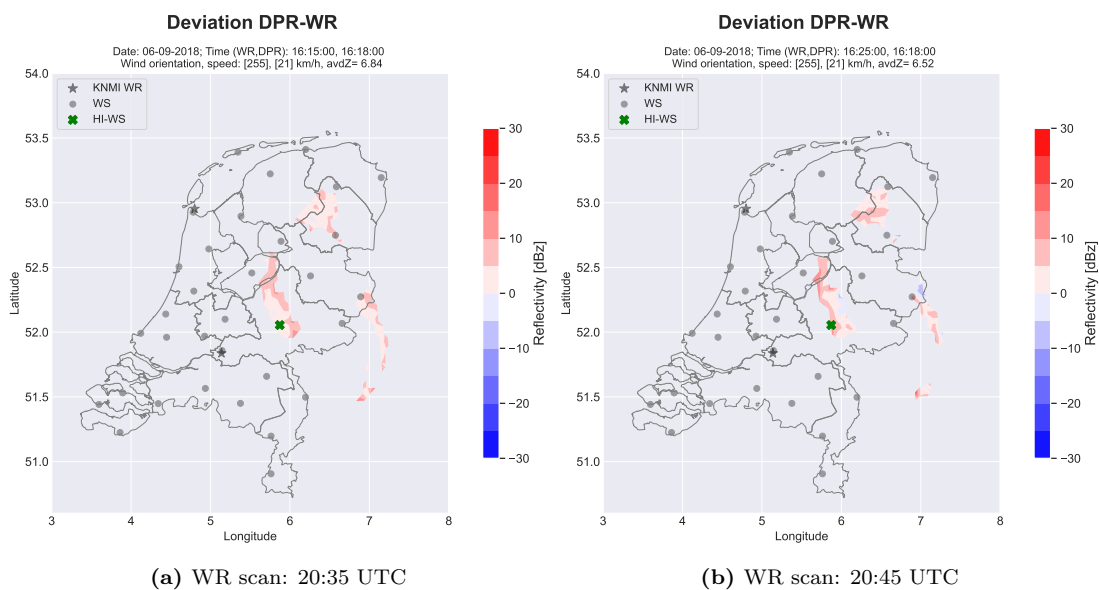


Figure B.12: Reflectivity deviation scans of DPR and WR scans on 06-09-2018

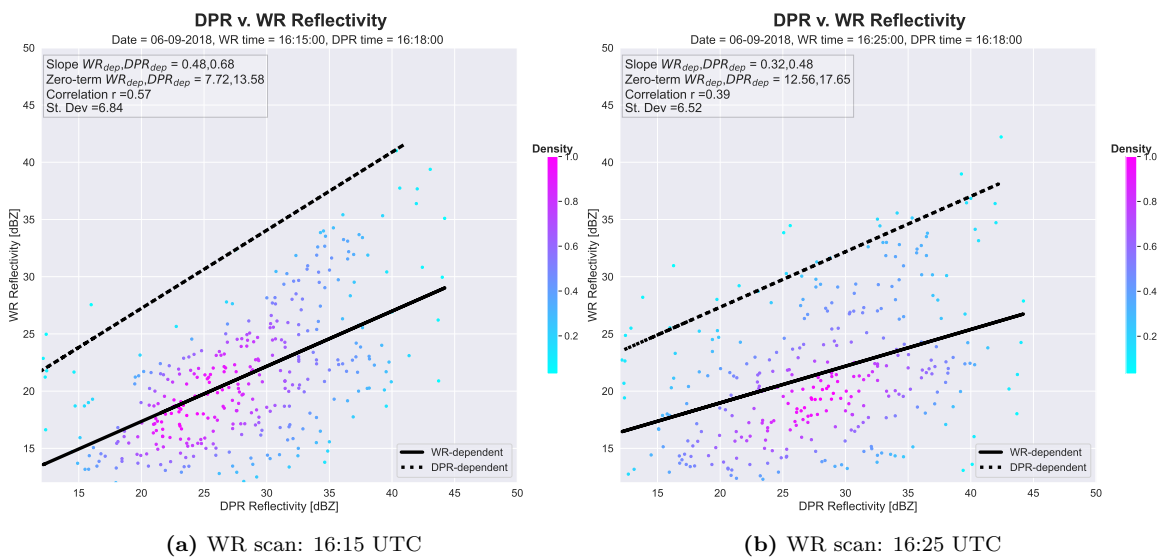
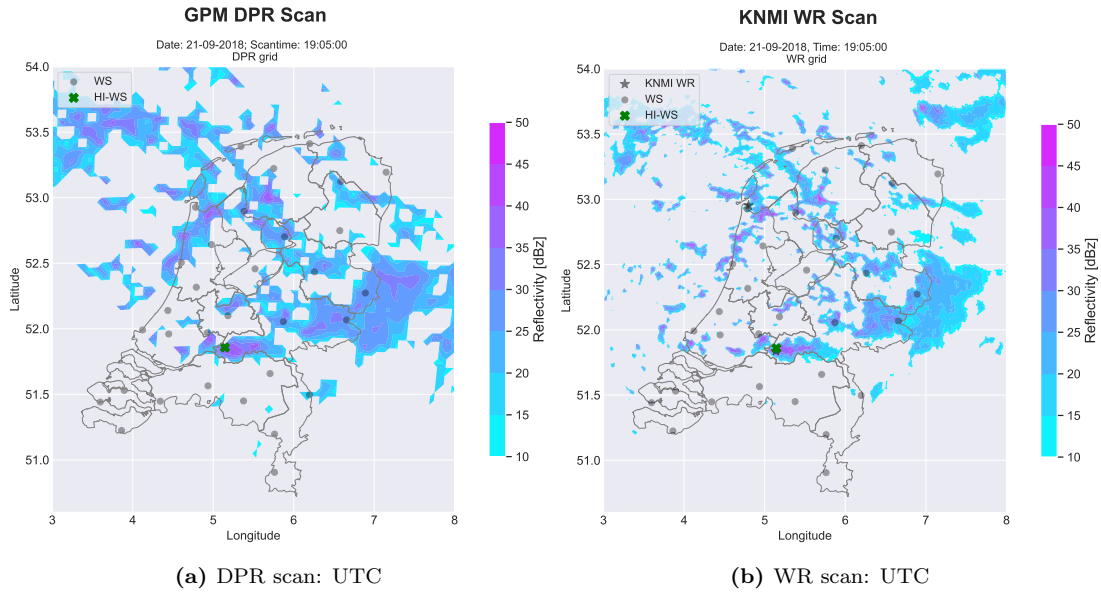


Figure B.13: Density scatter plots of  $Z_{DPR}$  and  $Z_{WR}$  on 06-09-2018

**Case Study D**

DPR scan time coincides with the HI-interval. Lower intensity intervals occur prior to and after the peak, which has an intensity of 15.7 mm/h. In both the DPR and WR scans, the HI-WS is situated in an HR zone. The wind direction is  $\pm 270^\circ$ . On the east side of the WS, the HR zone extends. The wind speed is relatively high (ca. 90 km/h), so it could be assumed that the HR zone passes fast over the WS towards the east. Due to the high wind speed, the middle of the HR zone could have been the start of the HI-interval. This assumption is substantiated by the WR observations, in which the HR zone moves towards the east quickly.



**Figure B.14:** DPR and WR scan for 21-09-2018

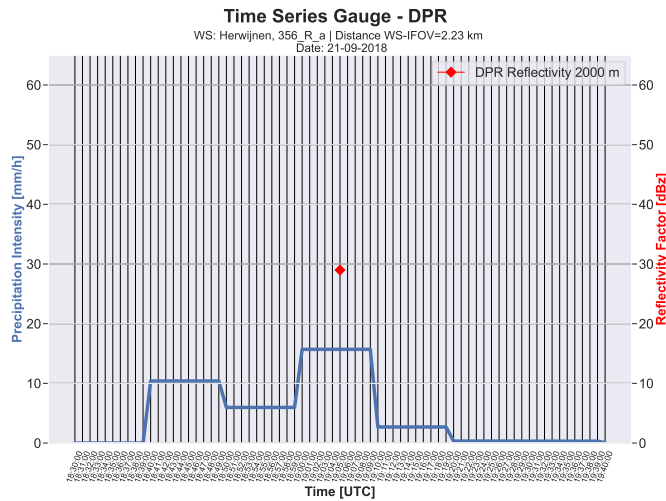


**Figure B.15:** Time series of HI-WS measurements within a range of  $\pm 40$  minutes from DPR scan time on 21-09-2018; the red check indicates the DPR reflectivity

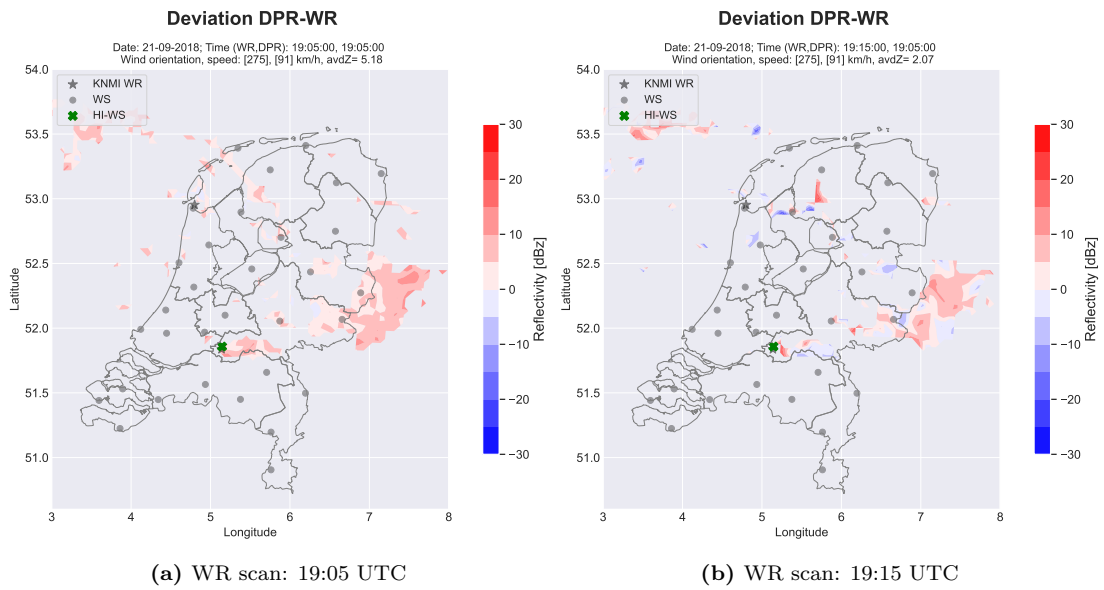


Figure B.16: Reflectivity deviation scans of DPR and WR scans on 21-09-2018

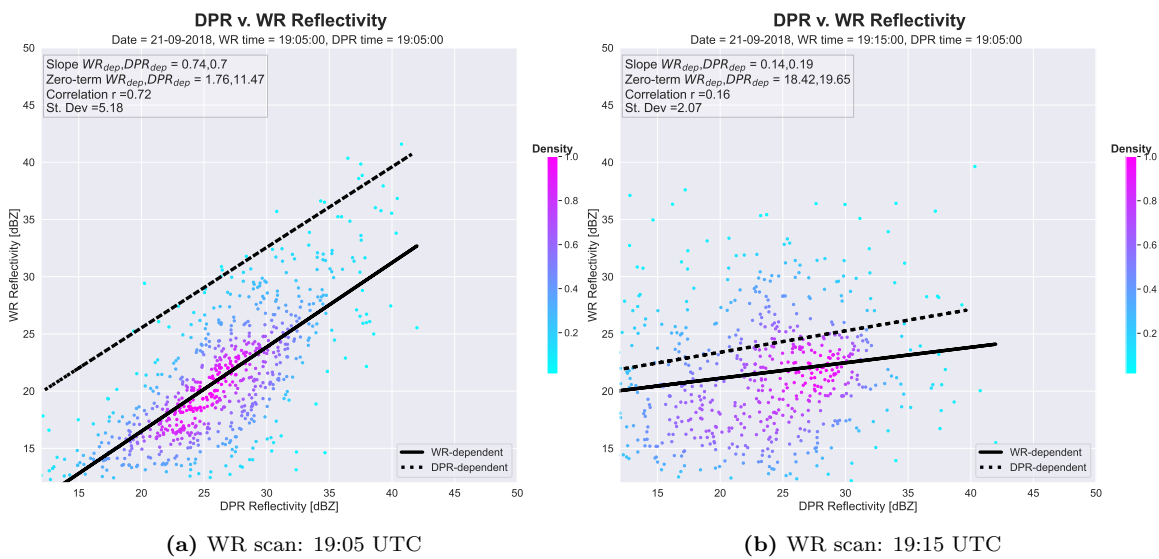
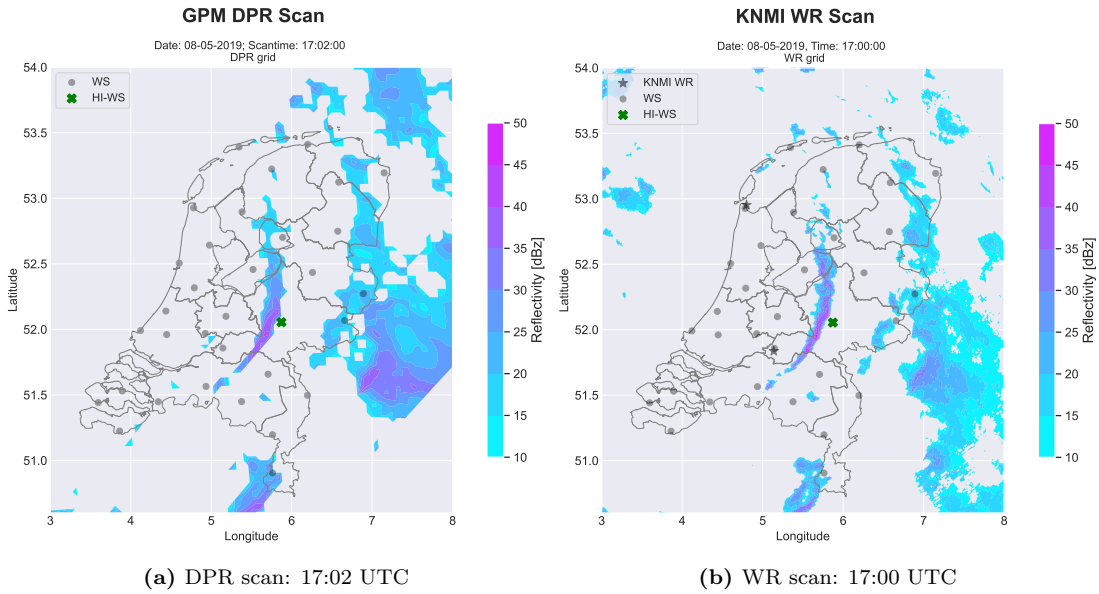


Figure B.17: Density scatter plots of  $Z_{DPR}$  and  $Z_{WR}$  on 21-09-2018

**Case Study E**

A HI-WS measurement is observed starting 18 minutes after GPM scan time with a peak intensity of 22.6 mm/h. After the HI-interval, lower intensity peaks follow. During scan time, the accumulated rainfall intensity at the HI-WS is equal to 0 mm/h. The HI-WS is not situated in an HR zone, which could be assumed to relate to the absence of rainfall at scan time. West of the HI-WS, an HR zone is observed. The various WR-scans in time show the HI-region moving in the wind direction at 1500 m. Moving from the HR zone towards the HI-WS in the direction of the wind, it can be assumed that the HR zone will pass over the HI-WS, presumably corresponding to the thereafter occurring HI-peak.



**Figure B.18:** DPR and WR scan for 08-05-2019; HI-measurement starting at 17:20 UTC

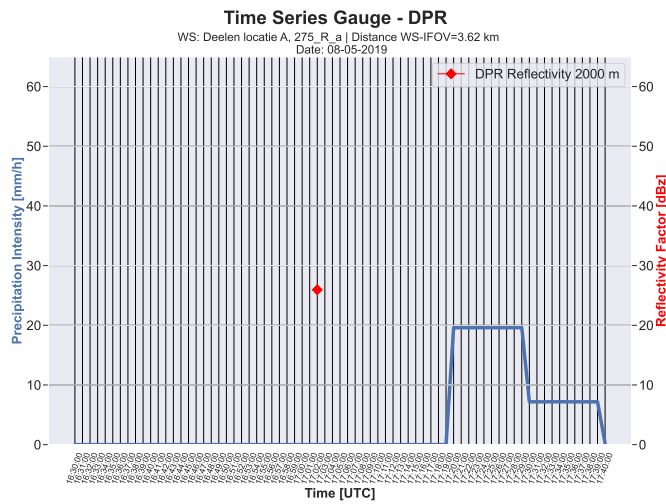


**Figure B.19:** Time series of HI-WS measurements within a range of  $\pm 40$  minutes from DPR scan time on 08-05-2019; the red check indicates the DPR reflectivity

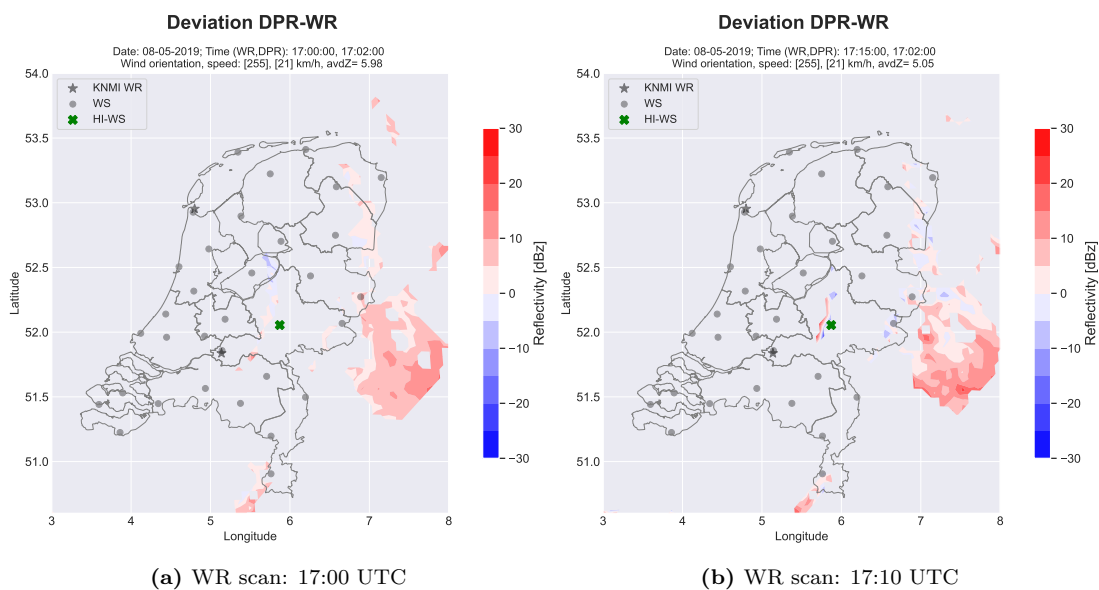


Figure B.20: Reflectivity deviation scans of DPR and WR scans for two time intervals on 21-09-2018

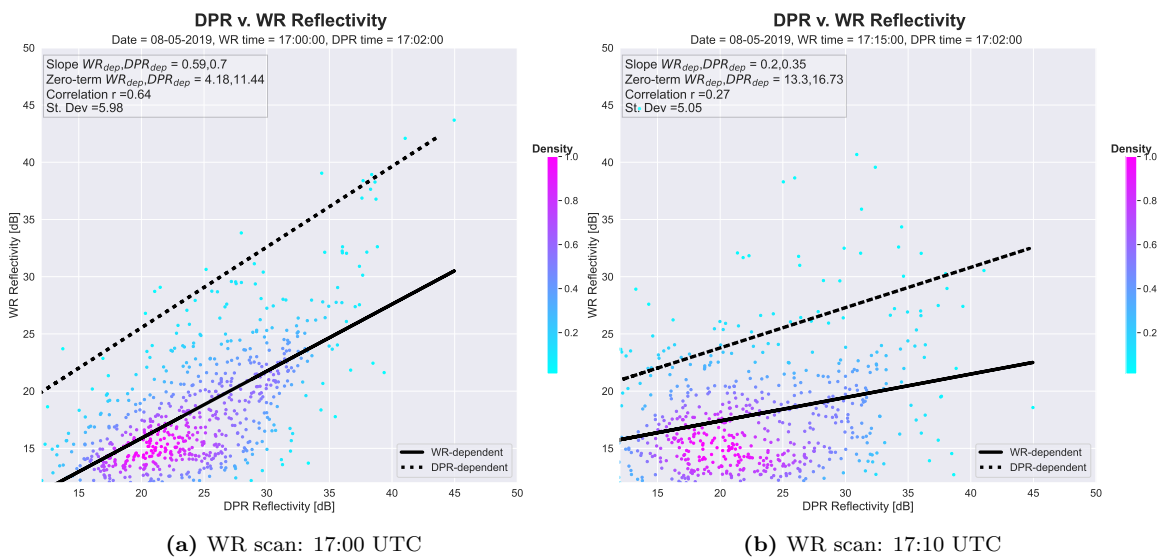
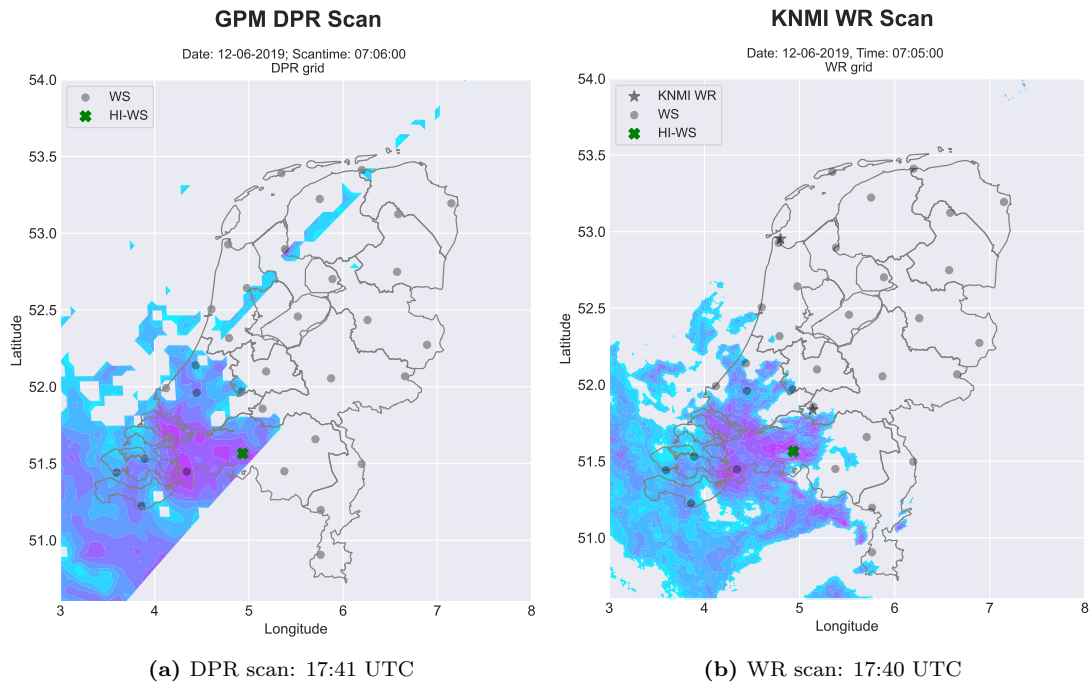


Figure B.21: Density scatter plots of  $Z_{DPR}$  and  $Z_{WR}$  on 21-09-2018

### Case Study F

A high-intensity interval of 25.3 mm/h is observed starting 7 minutes prior to scan time. Therefore, scan time occurs during the HI-interval. After the peak, a slightly lower intensity interval occurs of  $\pm 15.5$  mm/h. In both radar scans, the weather station is situated in a relatively large HR zone. The area extends a bit towards the southeast, which, taking into account the southeasterly wind, could relate to the two consecutive high-intensity intervals. The movement direction in the consecutive WR scans corresponds to the observed wind direction. In those scans, however, the HR zone appears to have passed theat 17.15 already, whereas the HI-WS measured an average of 15.5 mm/h throughout the entire 10-minute interval (i.e. rain was observed during the full interval duration). This could indicate the effect of the distance between the two measurement types, namely the time it takes a raindrop to reach the ground depending on its specific drop velocity.



**Figure B.22:** DPR and WR scan for 12-06-2019

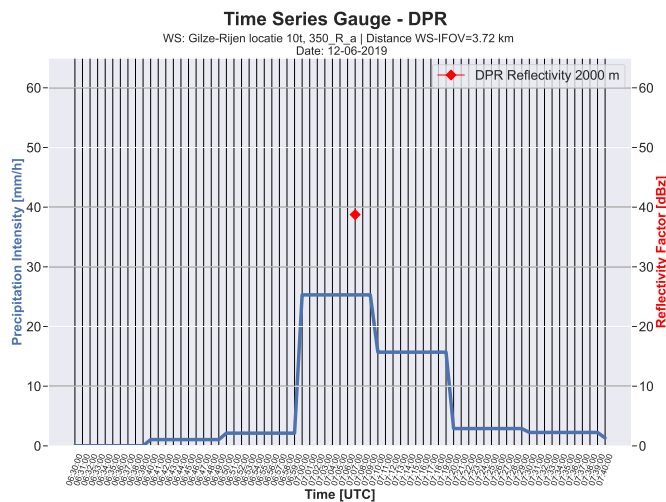
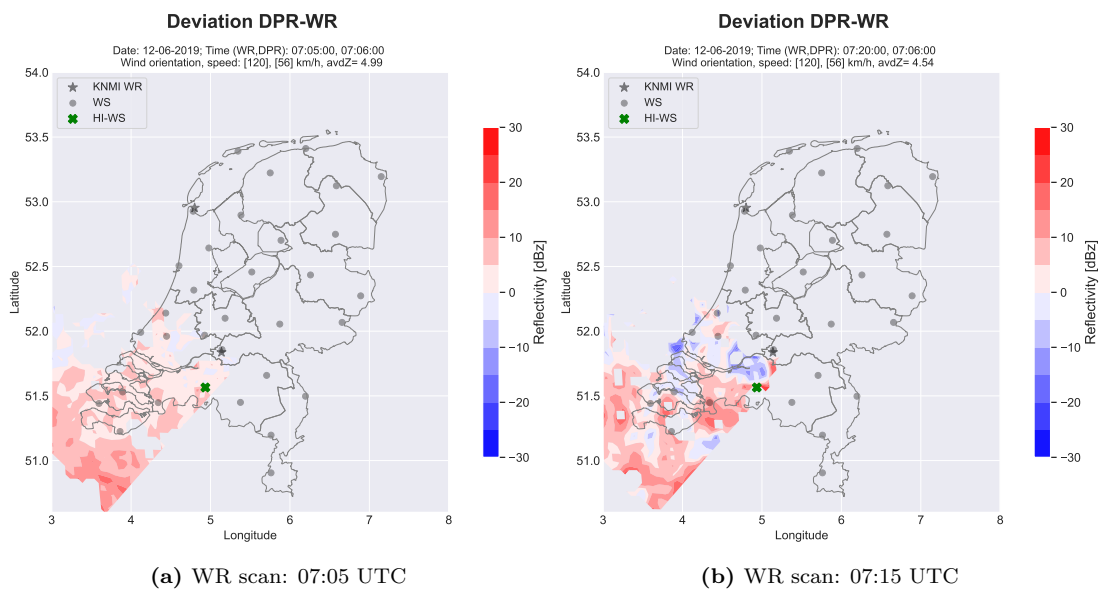
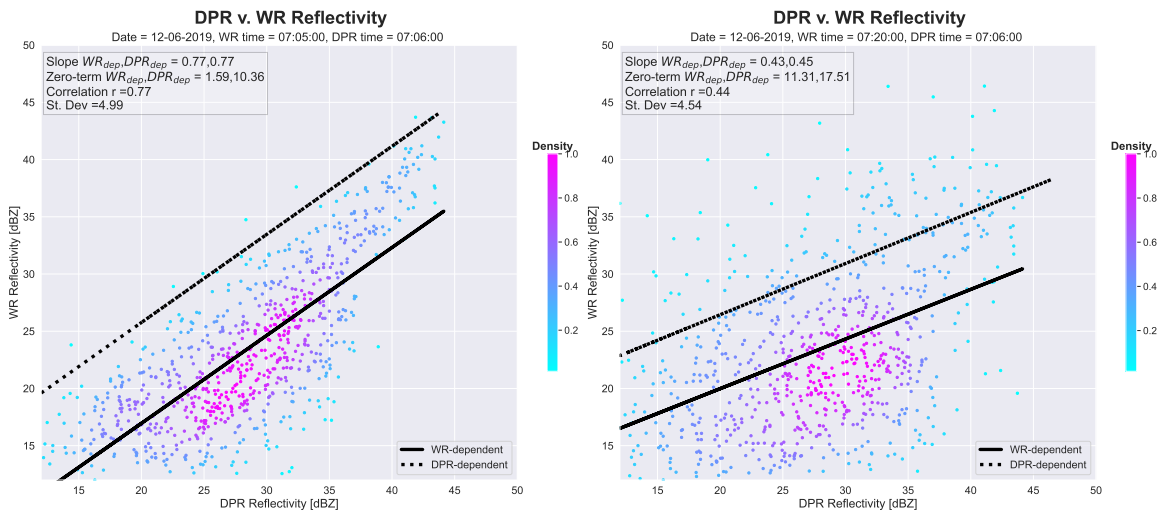


**Figure B.23:** Time series of HI-WS measurements within a range of  $\pm 40$  minutes from DPR scan time on 12-06-2019; the red check indicates the DPR reflectivity



(a) WR scan: 07:05 UTC (b) WR scan: 07:15 UTC  
**Figure B.24:** Reflectivity deviation scans of DPR and WR scans on 12-06-2019



(a) WR scan: 07:05 UTC

(b) WR scan: 07:15 UTC

**Figure B.25:** Density scatter plots of  $Z_{DPR}$  and  $Z_{WR}$  on 12-06-2019

**Case Study G**

During the 40 minute range from DPR-scantime, one HI-WS is observed: *Wijk aan Zee* observed two consecutive HI-intervals of 39.7 and 27 mm/h occurring 24 and 14 minutes prior to DPR scan time, respectively. Striking in this case study is that a very large high-reflectivity zone is present, covering most of the left swath of the DPR scan. The windorientation is  $\pm 120^\circ$ . Reflectivity values  $\geq 40$  dB are observed northwest of the HI-WS which are assumed to be related to the high intensity intervals, considering the winddirection and the relatively low wind speed and small time lag between scantime and the HI-intervals.

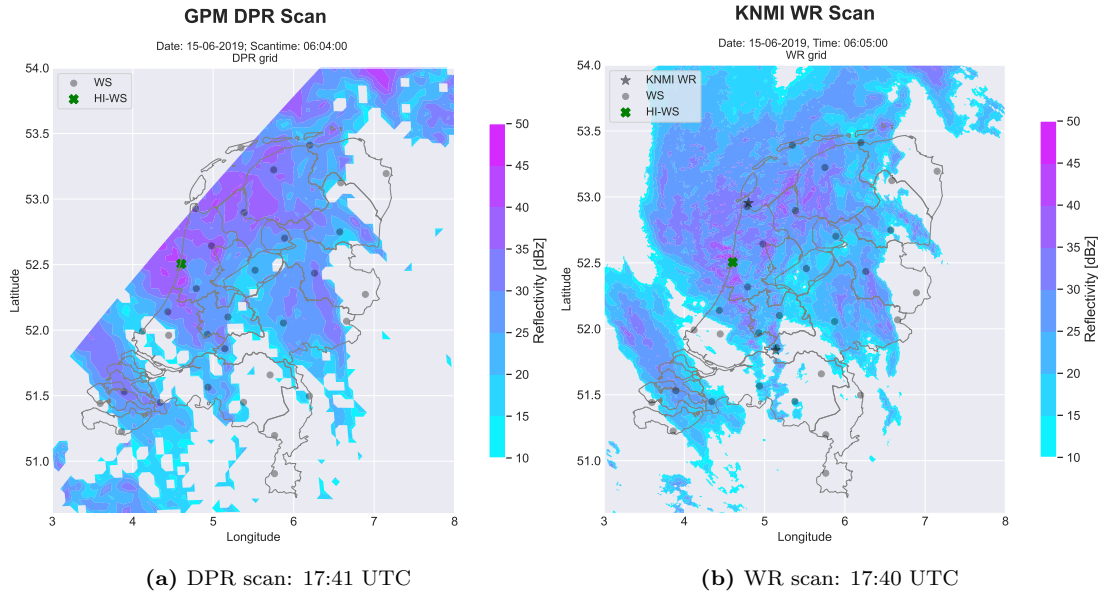


**Figure B.26:** DPR and WR scan for 15-06-2019

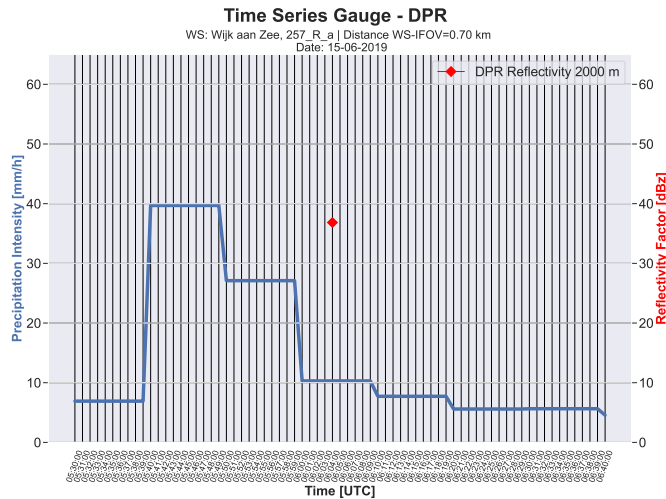


**Figure B.27:** Time series of HI-WS measurements within a range of  $\pm 40$  minutes from DPR scan time on 15-06-2019; the red check indicates the DPR reflectivity

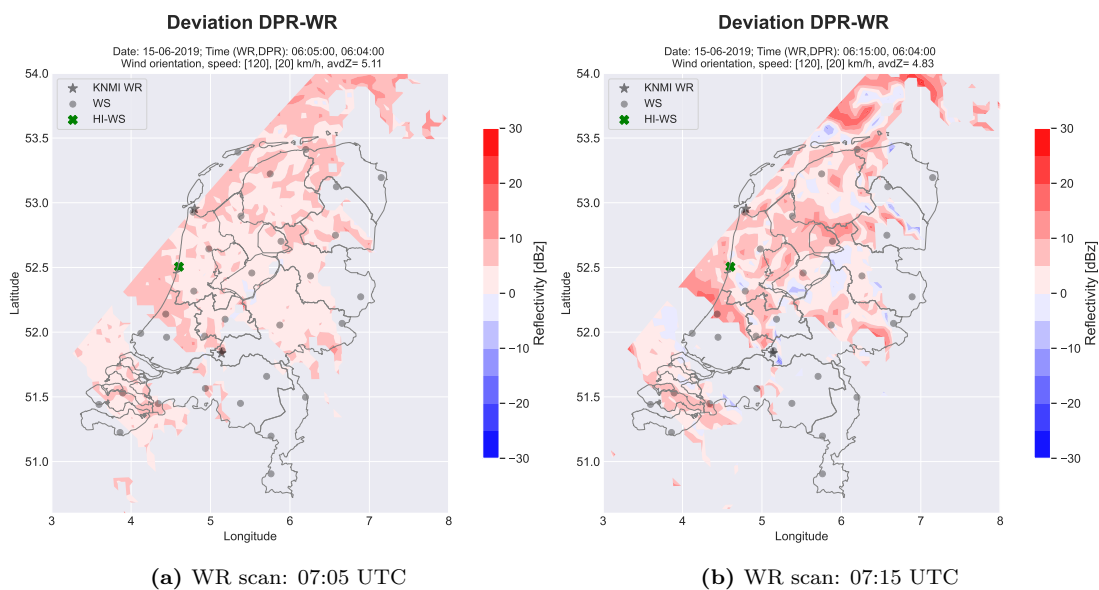


Figure B.28: Reflectivity deviation scans of DPR and WR scans on 12-06-2019

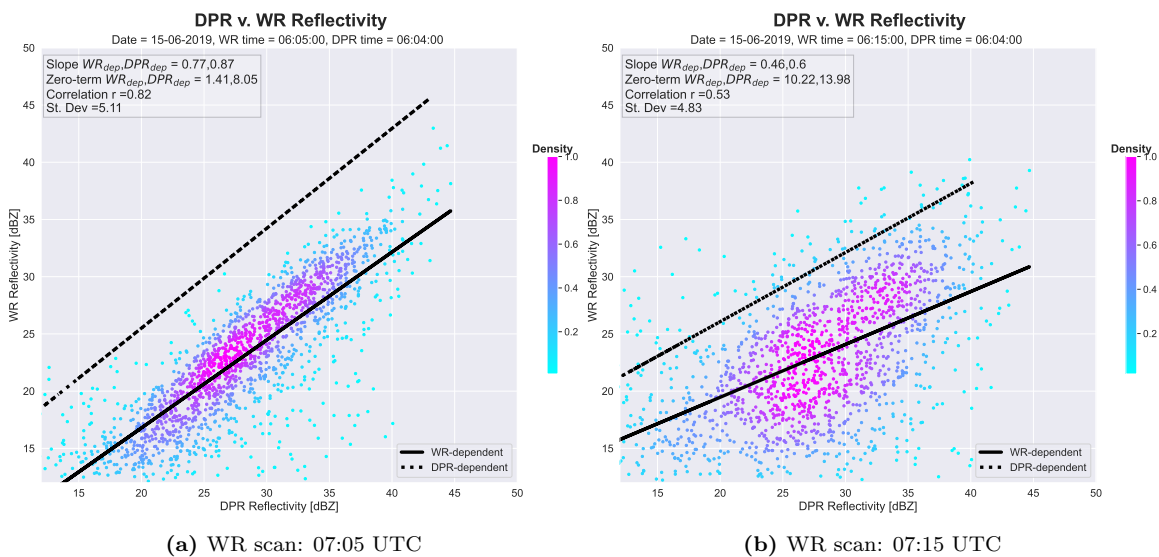


Figure B.29: Density scatter plots of  $Z_{DPR}$  and  $Z_{WR}$  on 12-06-2019

### Case Study H

The DPR scan time coincides with the HI-WS interval, with a peak intensity of 19.7 mm/h. Both the DPR -and WR scan display an HR zone overlapping the HI-WS. The observed wind speed is relatively high with a value of 59 km/h and the HR zone is observed to have a small width, which can be assumed to cause the local, one-interval peak. This can be verified in the WR measurements after 21.00 UTC, in which the HR zone no longer overlaps the HI-WS.

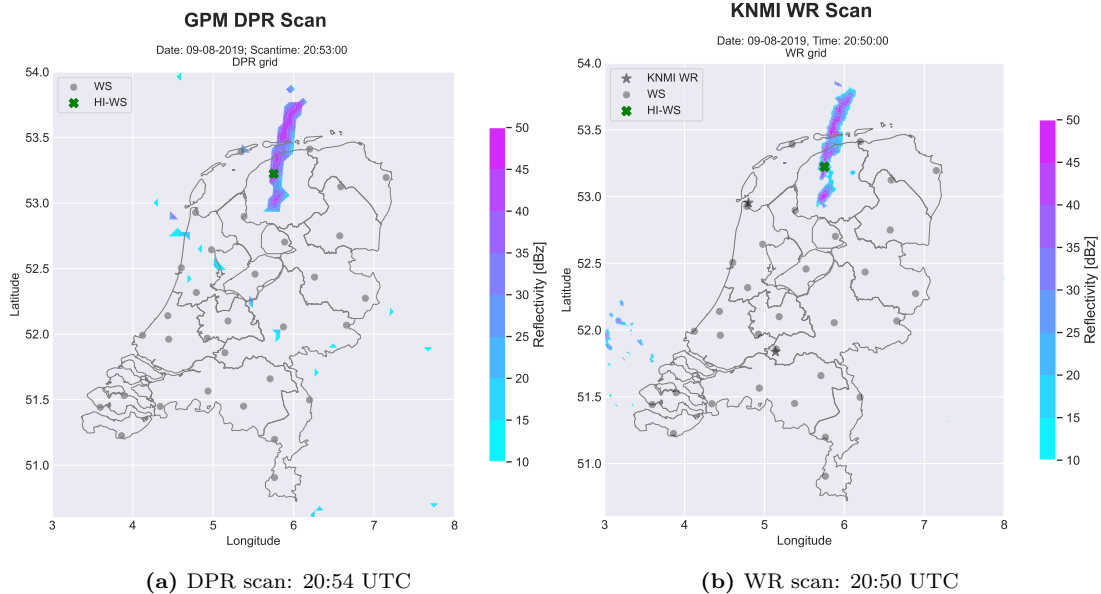


Figure B.30: DPR and WR scan for 09-08-2019

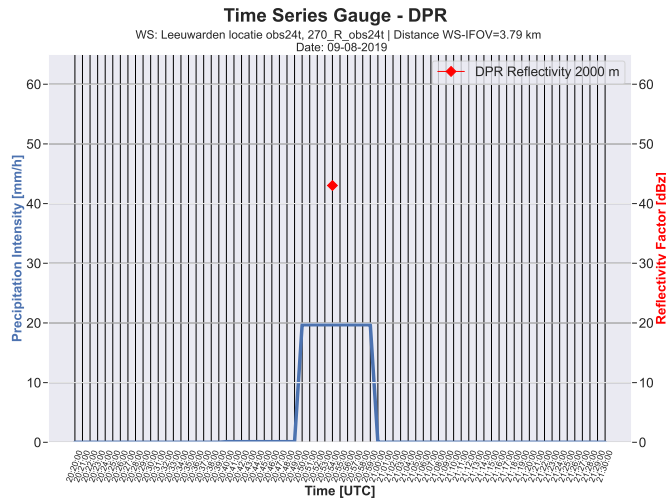


Figure B.31: Time series of HI-WS measurements within a range of  $\pm 40$  minutes from DPR scan time on 09-08-2019; the red check indicates the DPR reflectivity

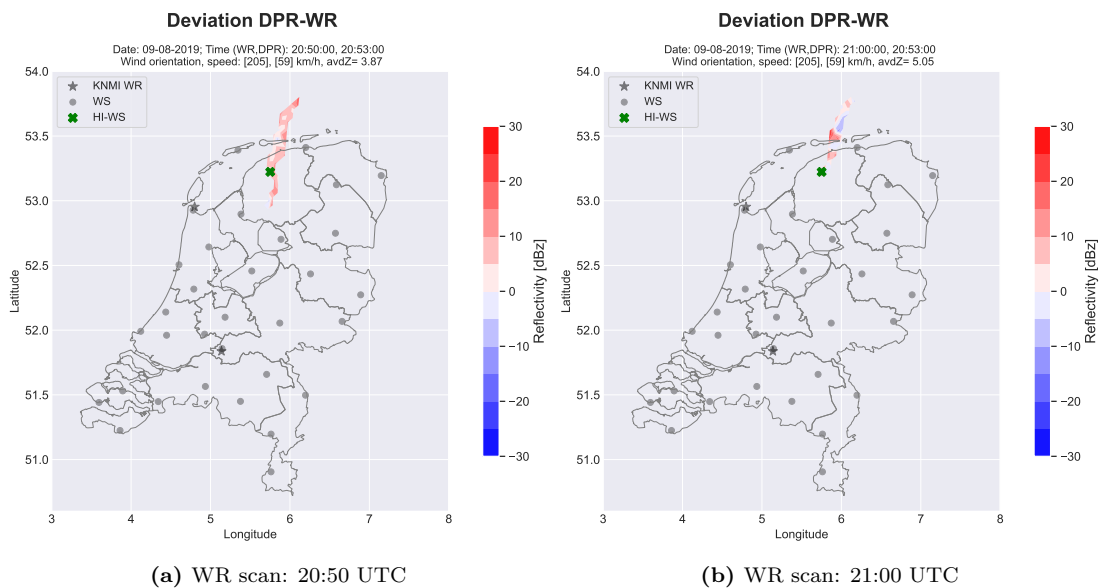


Figure B.32: Reflectivity deviation scans of DPR and WR scans on 09-08-2019

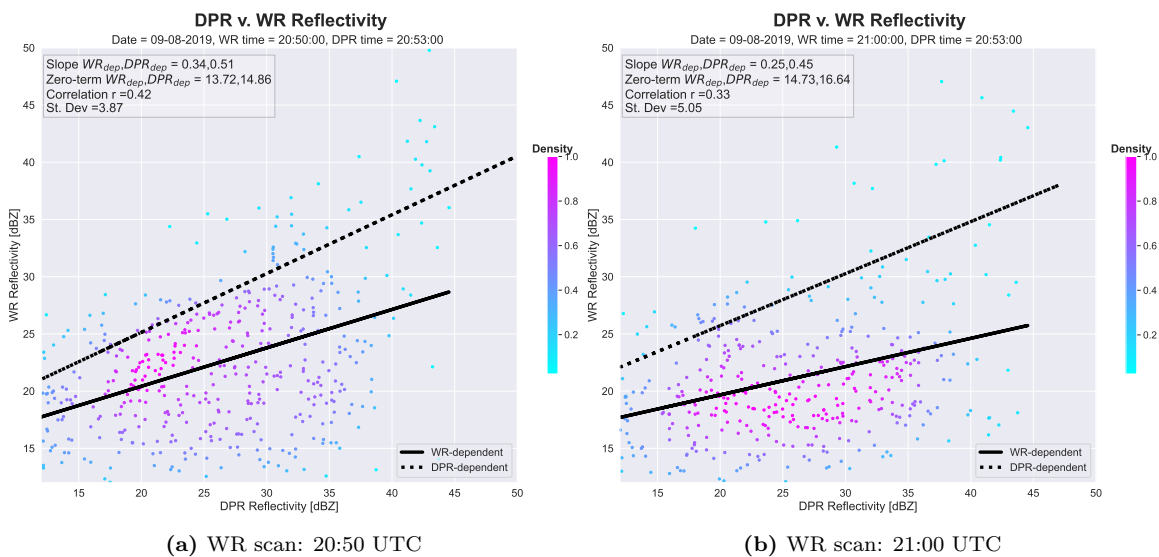
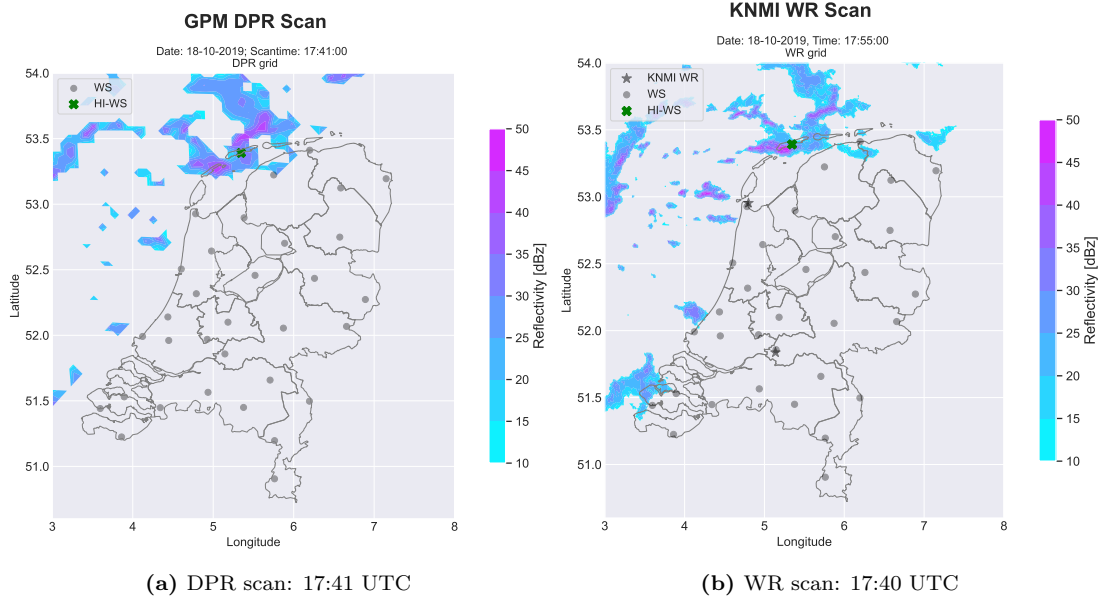


Figure B.33: Density scatter plots of  $Z_{DPR}$  and  $Z_{WR}$  on 09-08-2019

**Case Study I**

The DPR scan time occurs 19 minutes before the start of the HI-WS interval, with a peak intensity of 44.3 mm/h. At scan time, a lower intensity is observed of  $\pm 6$  mm/h. In both the DPR and WR scan, the HI-WS is situated in a relatively high reflectivity zone. A south-westerly wind is observed with a relatively high wind speed (ca. 80 km/h), so it can be assumed that the HR zone situated south-west of the HI-WS will move with great speed over the HI-WS. Therefore, that particular HR zone can be assumed to correspond to the observed HI-interval. This claim can be further substantiated using the consecutive WR-scans, in which the respective HR zone is indeed moving over the HI-WS around the time of the HI-interval.



**Figure B.34:** DPR and WR scan for 18-10-2019

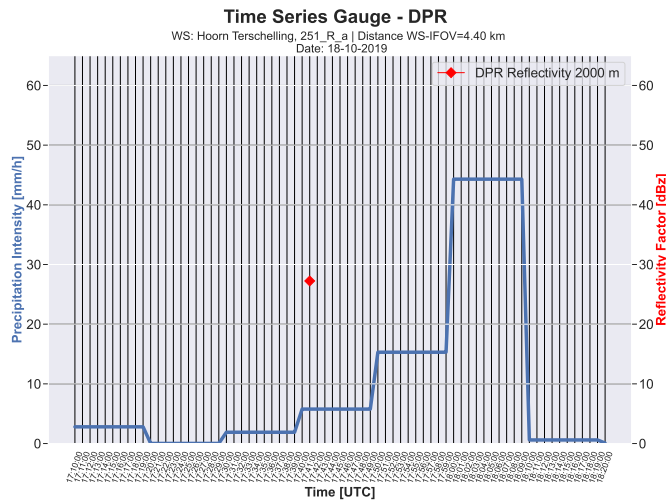


**Figure B.35:** Time series of HI-WS measurements within a range of  $\pm 40$  minutes from DPR scan time on 18-10-2019; the red check indicates the DPR reflectivity

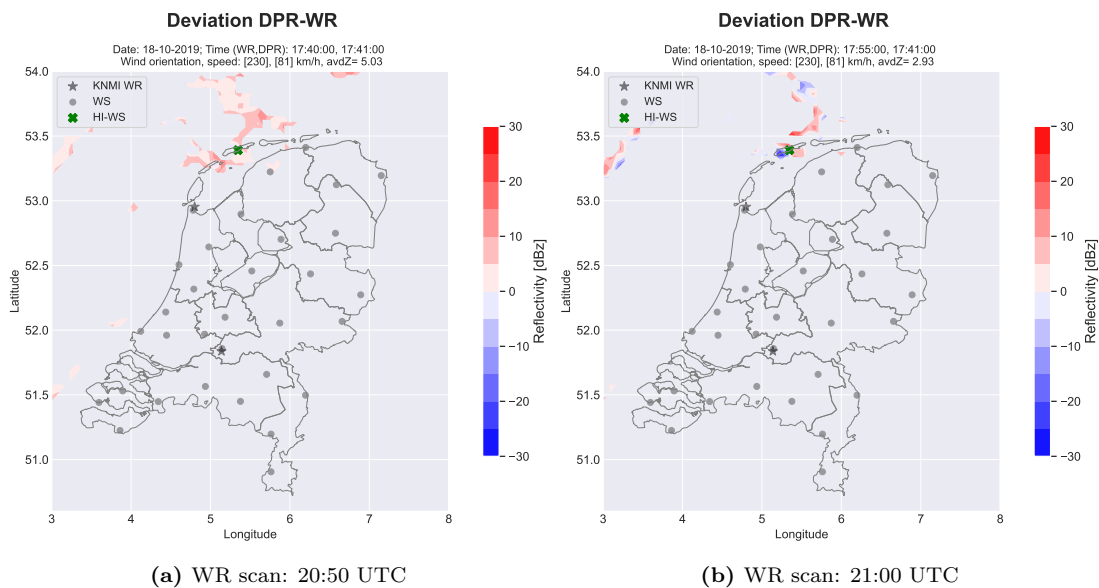


Figure B.36: Reflectivity deviation scans of DPR and WR scans on 18-10-2019

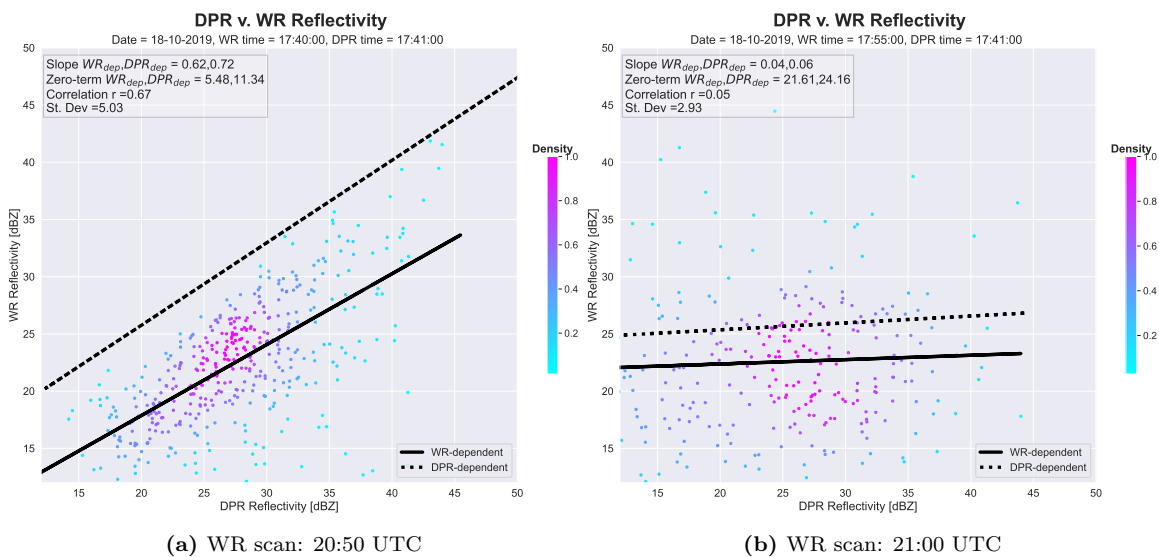


Figure B.37: Density scatter plots of  $Z_{DPR}$  and  $Z_{WR}$  on 18-10-2019

### Case Study J

Three stations in the automatic network measured a precipitation intensity  $\geq 15$  mm/h within a range of  $\pm 40$  minutes from DPR scan time: *Nieuw Beerta* measured a peak intensity of 104 mm/h starting 24 minutes after DPR scan time, *Heino* measured a peak intensity of 21.9 mm/h starting 36 minutes before DPR scan time and *Hoogeveen* measured a peak intensity of 18.5 mm/h starting 4 minutes after DPR scan time.

During scan time, *Hoogeveen* is the only station measuring rainfall (intensity of approximately 4 mm/h). *Nieuw Beerta* and *Hoogeveen* are situated outside the range of the scan width (and thus directly overlapping reflectivity measurements aren't known), whereas *Heino* is situated at the edge of the scan. In the WR scan, *Hoogeveen* is the only station situated in a HR zone and also the only station that measures HI during scan time. Therefore, it could be assumed that that particular high reflectivity zone relates to the high-intensity that is measured at the ground. When moving from *Heino* in a northeast direction to first *Hoogeveen* and then *Nieuw Beerta*, it can be noted that the three HI-WS are aligned with one another. Since the wind orientation is found to be southwesterly, it could be assumed that the HR zone observed at *Hoogeveen* has first passed *Heino* and will then move to *Hoogeveen*. Furthermore, another HR zone is observed near *Nieuw-Beerta*, which, since the relatively high wind speed, is presumably related to the HI-peak at that station. When regarding the consecutive ground radar scans, this indeed seems to be the case.

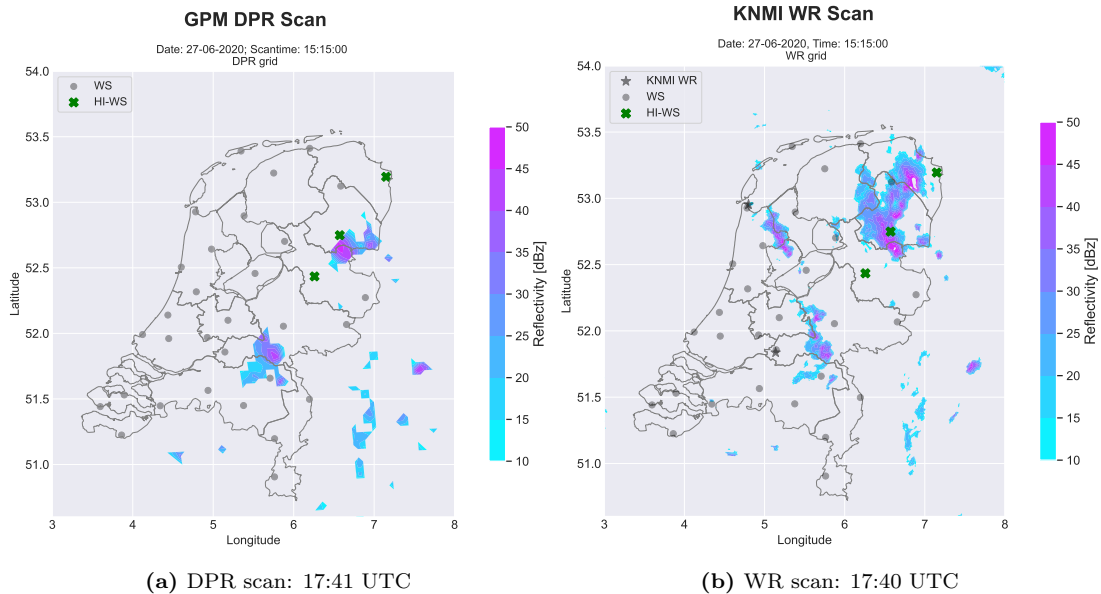
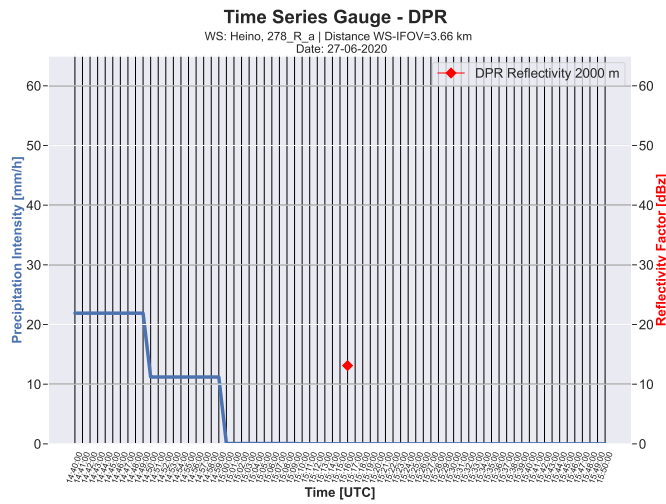
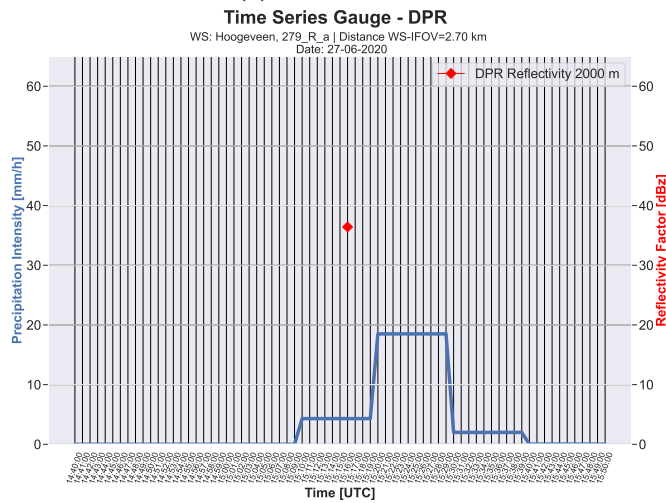


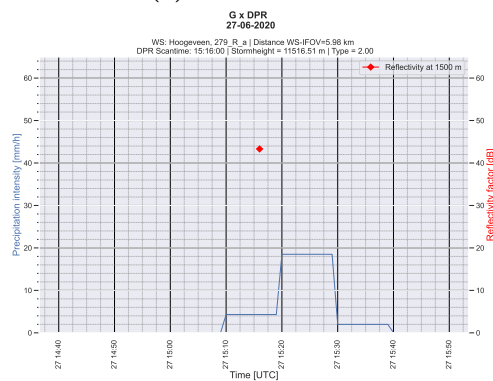
Figure B.38: DPR and WR scan for 27-06-2020;



(a) Weather station:



(b) Weather station:



(c) Weather station:

**Figure B.39:** Time series of HI-WS measurements within a range of  $\pm 40$  minutes from DPR scan time on 27-06-2020; the red check indicates the DPR reflectivity

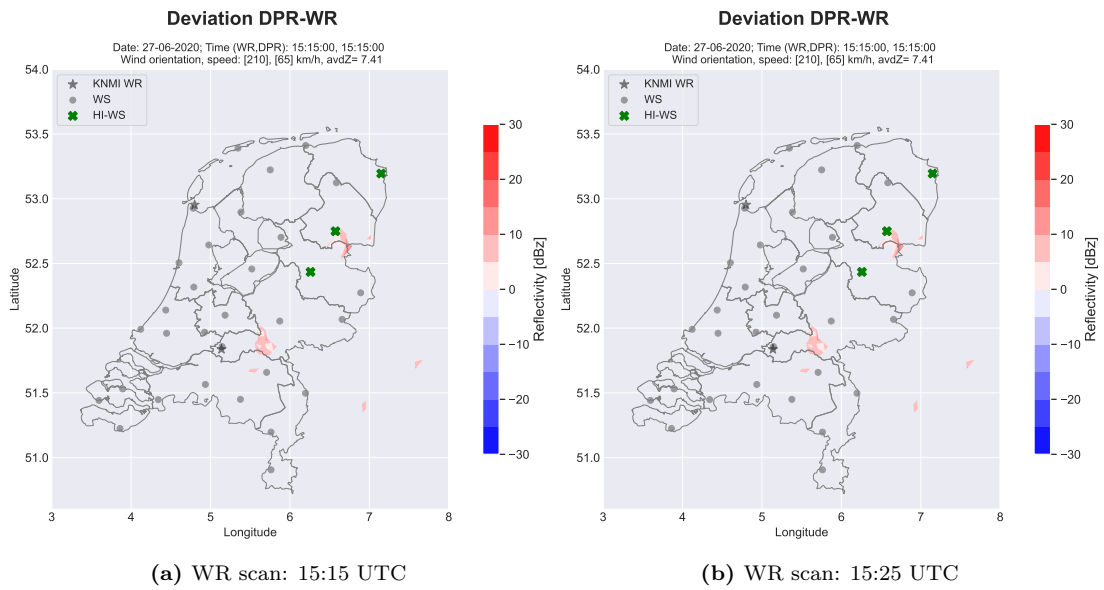


Figure B.40: Reflectivity deviation scans of DPR and WR scans on 27-06-2020

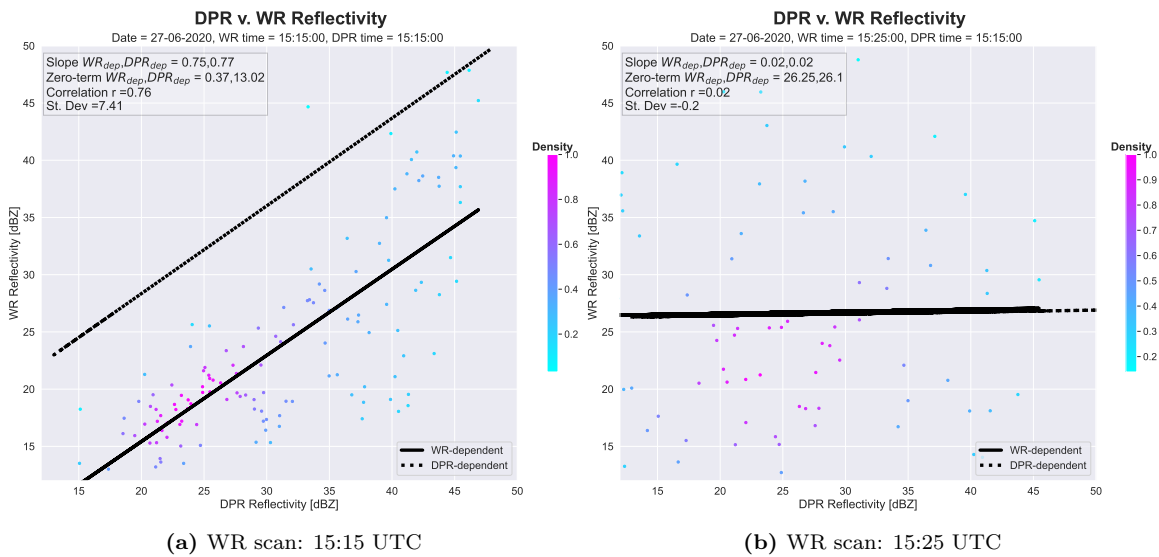


Figure B.41: Density scatter plots of  $Z_{DPR}$  and  $Z_{WR}$  on 27-06-2020

### Case Study K

*Arcen* recorded a HI-interval of 72.4 mm/h starting 37 minutes after DPR scan time. At scan time, zero rainfall is observed. From both DPR and WR data, it can be observed that the HI-WS is not situated in a high reflectivity zone during scan time, possibly relating to the zero rainfall measurement during the coinciding gauge interval. Several high reflectivity zones are located near the HI-WS, in southeasterly, southwesterly and northwesterly direction. The wind orientation is  $\pm 220^\circ$ , which would lead to the assumption that the HR on the southwest of the HI-WS relates to the HI-interval. However, from the consecutive WR scans, it can be observed that all high-reflectivity zones move towards the north. This wind direction corresponds to the wind observations from 9000 m altitude ( $\pm 185^\circ$ ), which then again relates to the observed storm height by the DPR ( $\pm 10,000$  m). Also, the WR scans show that the southwesterly HR-zone expands with time and overlaps the HI-WS during the HI-interval. Considering only the wind direction and observations from the DPR scan, this was not expected. However, when taking into account the relatively large time lag and the dynamic behaviour of storm systems, it could have been expected that the instantaneous DPR measurement would not be able to provide sufficient information.

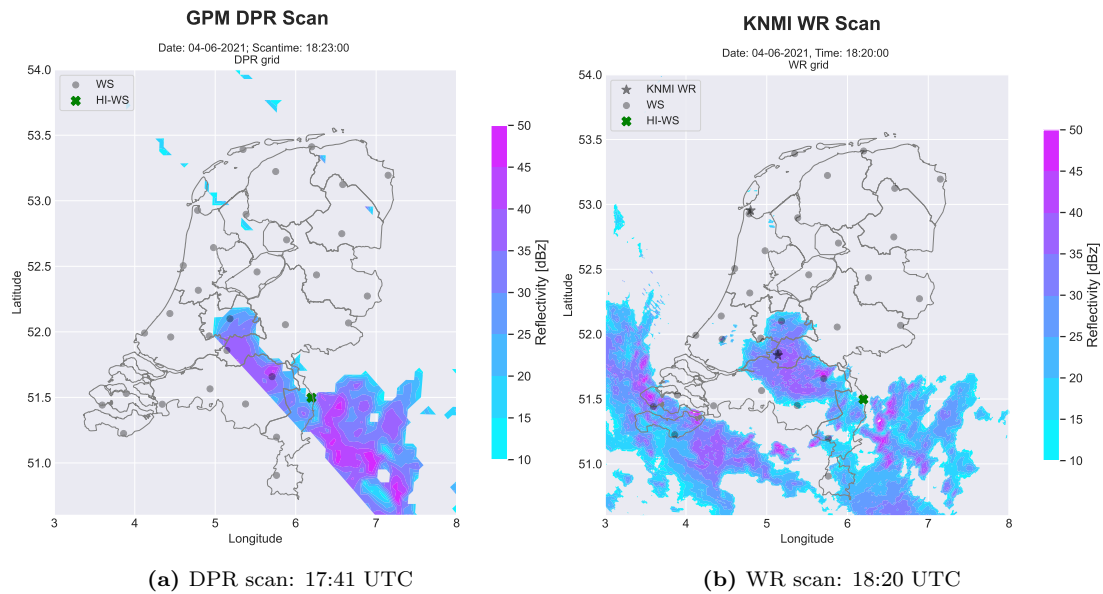
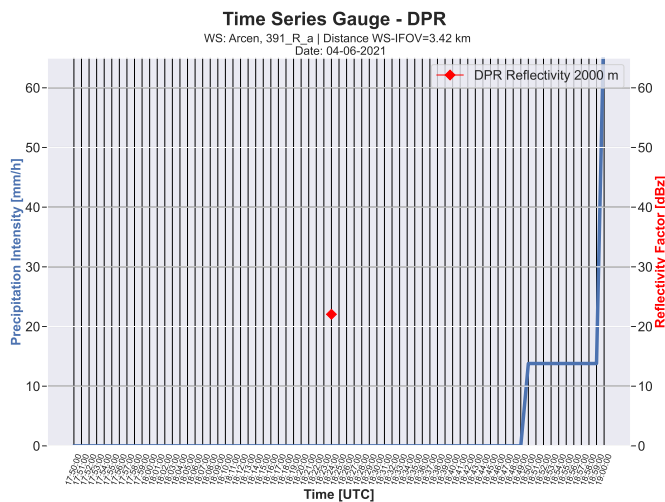
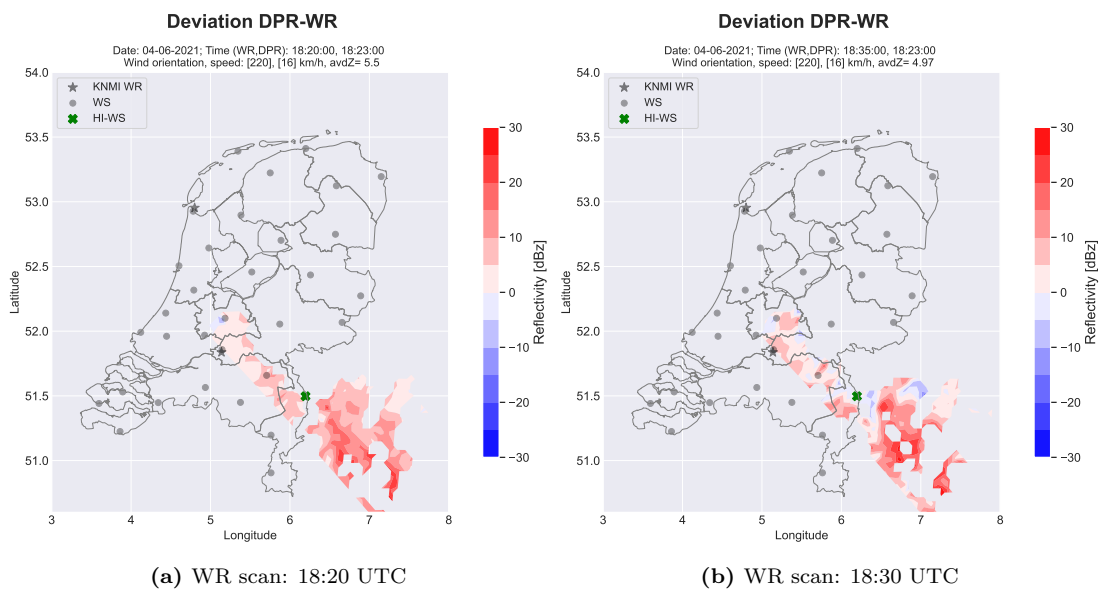


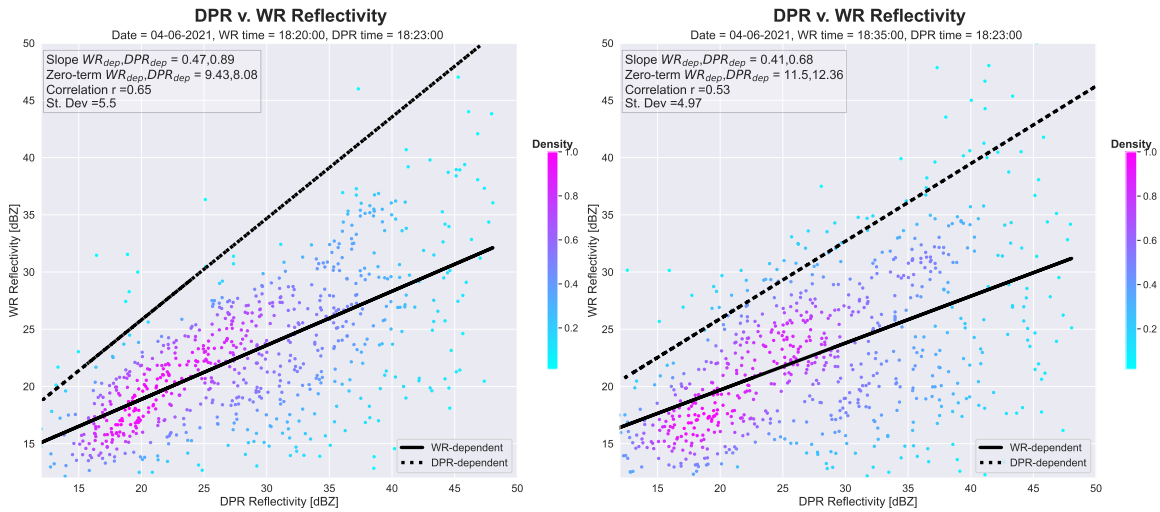
Figure B.42: DPR and WR scan for 04-06-2021



**Figure B.43:** Time series of HI-WS measurements within a range of  $\pm 40$  minutes from DPR scan time on 04-06-2021; the red check indicates the DPR reflectivity



**Figure B.44:** Reflectivity deviation scans of DPR and WR scans on 04-06-2021



(a) WR scan: 18:20 UTC

(b) WR scan: 18:30 UTC

**Figure B.45:** Density scatter plots of  $Z_{DPR}$  and  $Z_{WR}$  on 04-06-2021

### Case Study L

Two HI-WS are found for 28-06-2021: *Ell* observes an intensity of 51.8 mm/h starting 10 minutes before scan time and *Westdorpe* starts measuring an intensity of 34.9 mm/h 39 minutes after scan time. *Ell* is situated in an HR zone, whereas *Westdorpe* is not. *Westdorpe* measures an intensity equal to 0 mm/h during scan time. At 2000 m altitude, the wind orientation at *Westdorpe* is observed to be southeasterly and southwesterly at *Ell*.

The HR zone near *Ell* is assumed to relate to the HI-interval, with regard to its distance to the WS.

Near *Westdorpe*, only moderate HI-zones are visible. Furthermore, those zones aren't aligned with the HI-WS in the direction of the wind. Therefore, those zones are assumed not to relate directly to the HI-interval. It could be assumed that, since the large time difference between the DPR scan and the HI-interval, the storm still has to initiate and thus can't yet be detected by the DPR as such. Regarding the consecutive WR scans, this assumption appears correct: in time, the moderate reflectivity zone detected in the DPR scan expands and larger reflectivity values are measured by the ground radar. Hence, it could be assumed that if a relatively high reflectivity zone is detected near a HI-WS within a 40-minute range of the HI-interval, that particular zone is related to the peak (provided that the wind speed is relatively low, as is the case in this particular example).

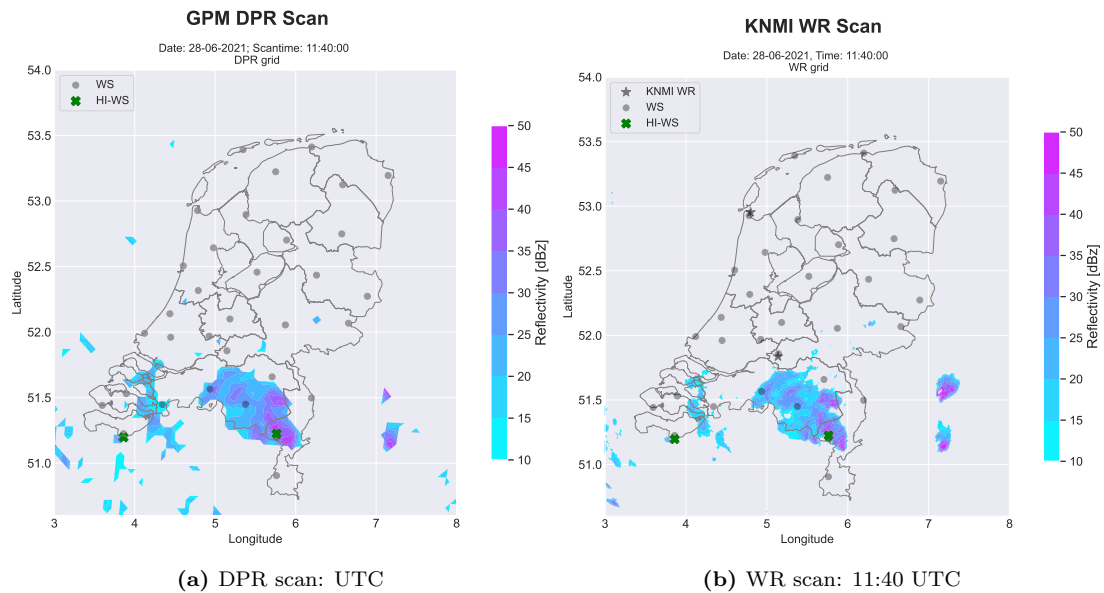
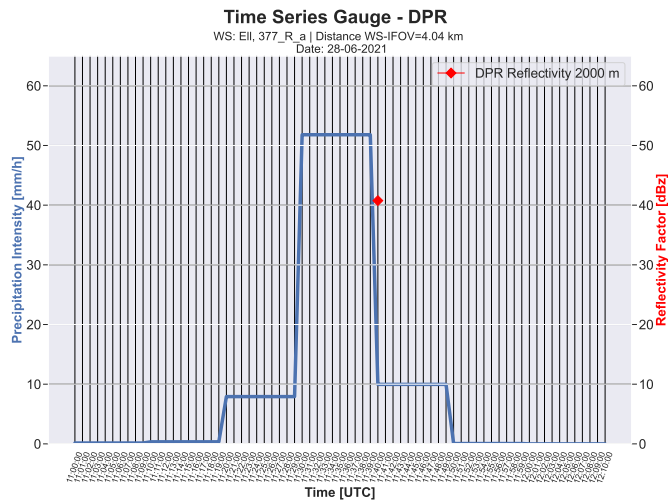
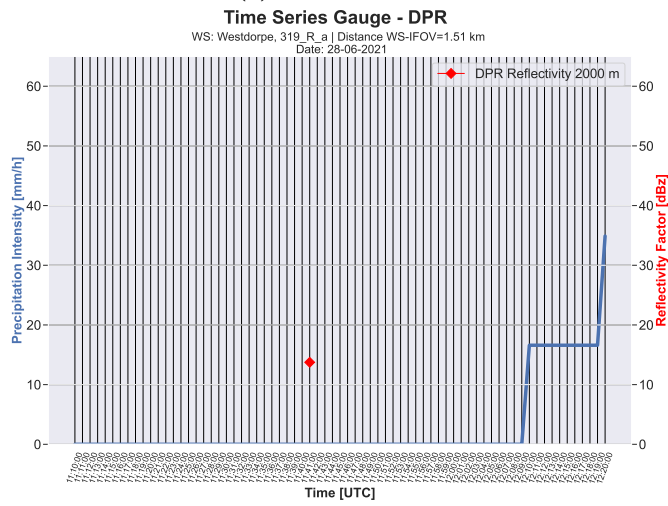


Figure B.46: DPR and WR scan for 28-06-2021



(a) Weather station:



(b) Weather station:

**Figure B.47:** Time series of HI-WS measurements within a range of  $\pm 40$  minutes from DPR scan time on 28-06-2021; the red check indicates the DPR reflectivity

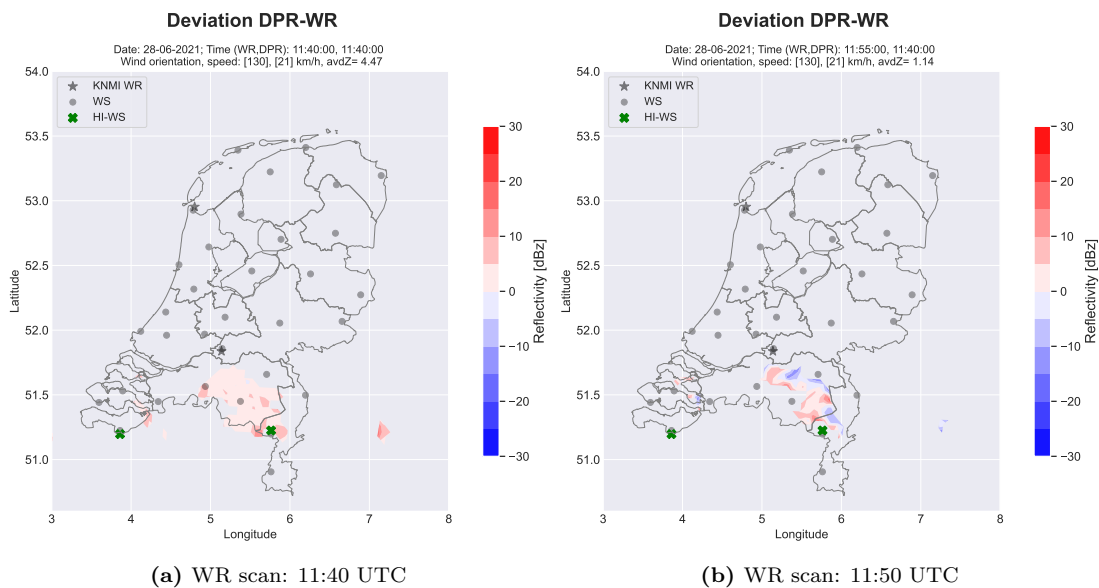


Figure B.48: Reflectivity deviation scans of DPR and WR scans on 04-06-2021

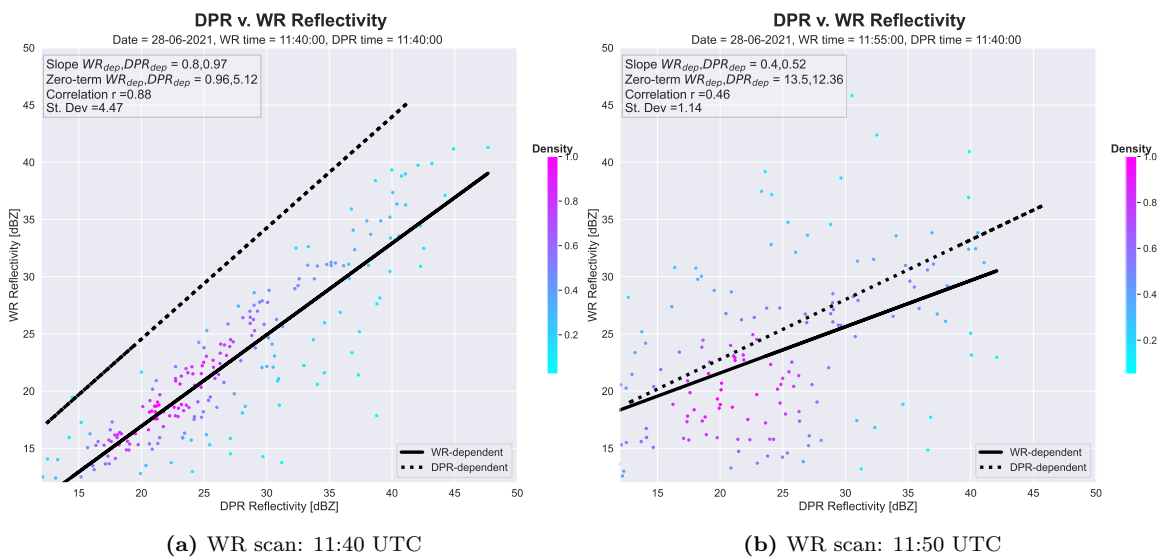


Figure B.49: Density scatter plots of  $Z_{DPR}$  and  $Z_{WR}$  on 04-06-2021

### Case Study M

Two HI-WS are found for 25-07-2021: *Rotterdam locatie 24t* observed an intensity of 20 mm/h during scan time and *De Bilt locatie A* observed an intensity of 24 mm/h 37 minutes prior to scan time. For the latter, an intensity of  $\pm 9$  mm/h is observed during scan time. Both weather stations are situated in high reflectivity zones. **Nog afmaken!**

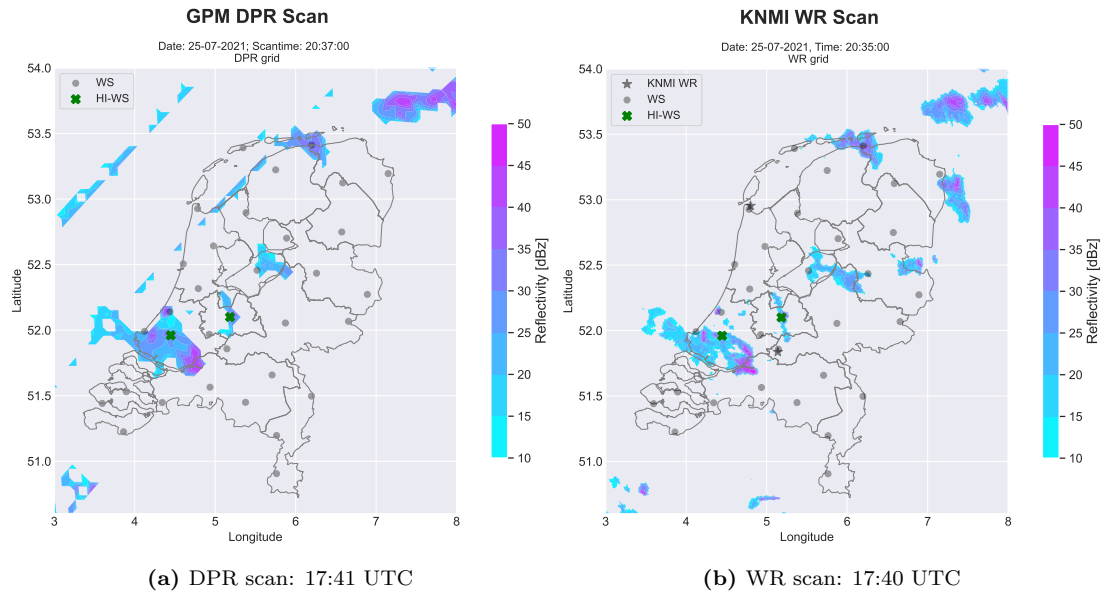
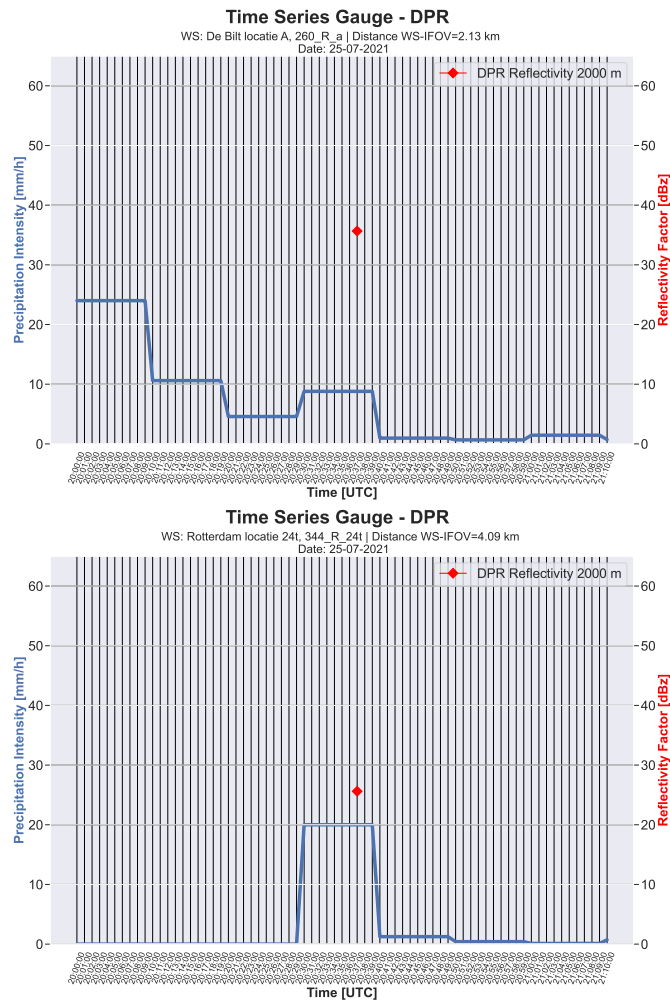


Figure B.50: DPR and WR scan for 25-07-2021



(a) Weather station:

**Figure B.51:** Time series of HI-WS measurements within a range of  $\pm 40$  minutes from DPR scan time on 25-07-2021; the red check indicates the DPR reflectivity

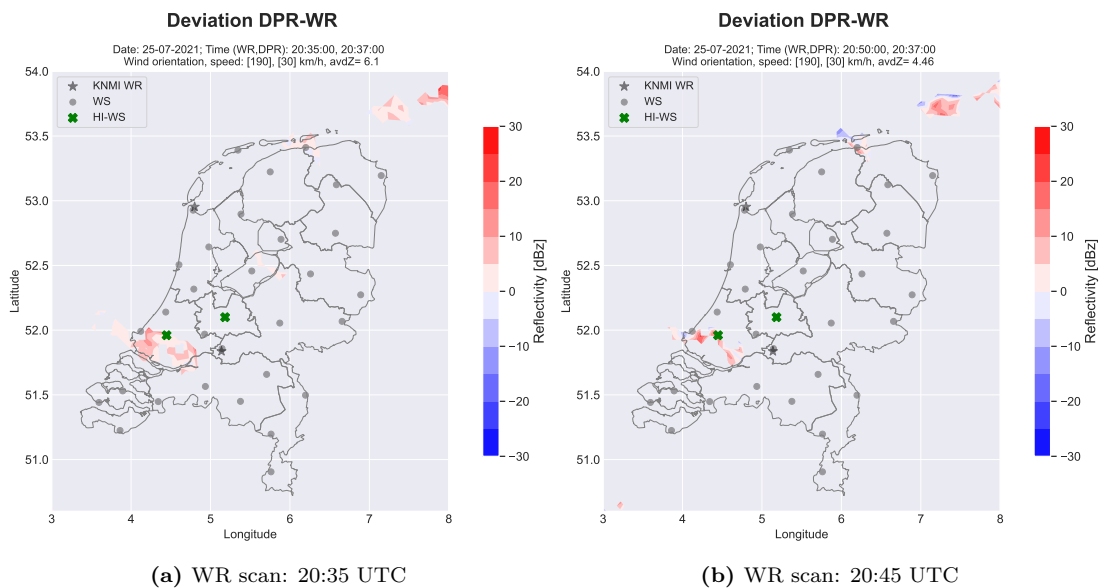


Figure B.52: Reflectivity deviation scans of DPR and WR scans on 25-07-2021

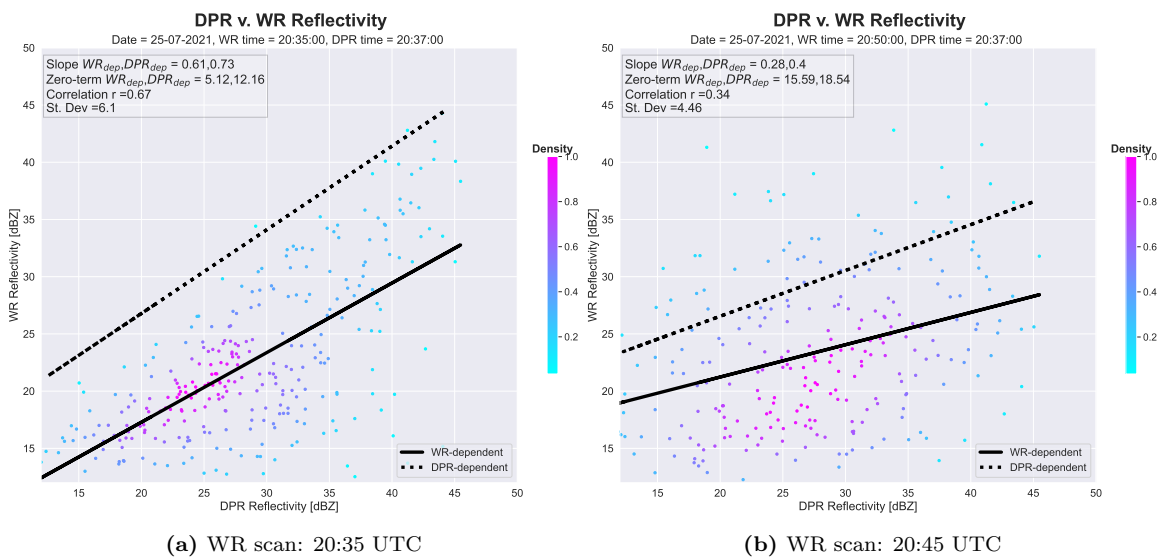
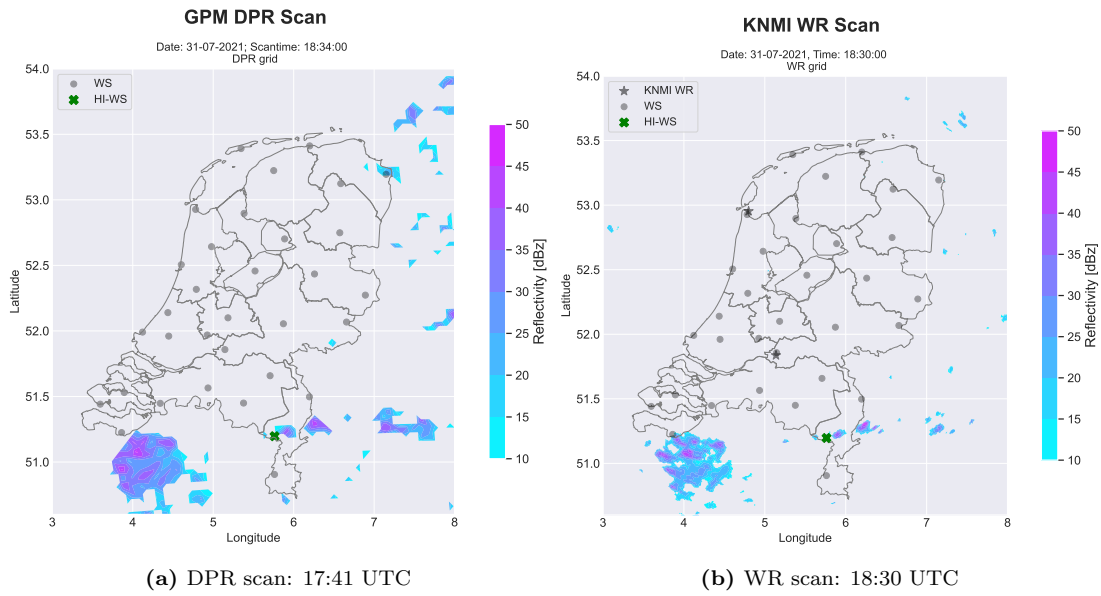


Figure B.53: Density scatter plots of  $Z_{DPR}$  and  $Z_{WR}$  on 25-07-2021

**Case Study N**

WS *Ell* observes an intensity of 23.6 mm/h 34 minutes prior to DPR scan time. During scan time, a marginal intensity is observed and a low reflectivity zone. Multiple high reflectivity zones are visible in the scan, of which the closest ones are located on the east of the HI-WS. A westerly wind is observed, thus it could be assumed that the HR zones in the east are related to the HI-event at *Ell*. The wind speed is moderate and the time lag relatively high, thus presumably the second furthest HR zone corresponds to the HI-peak.



**Figure B.54:** DPR and WR scan for 31-07-2021

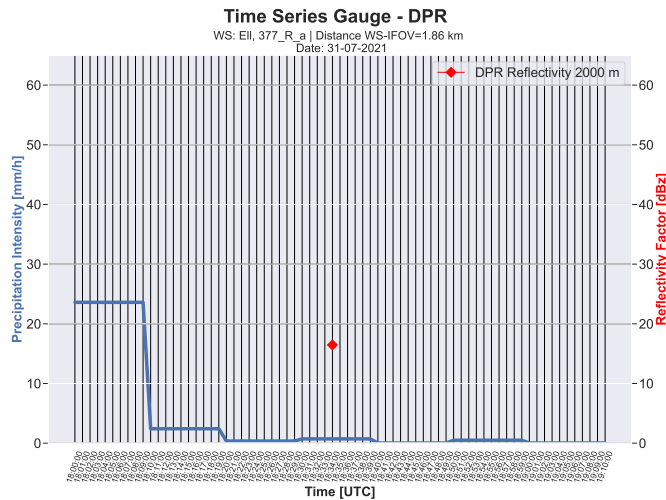


**Figure B.55:** Time series of HI-WS measurements within a range of  $\pm 40$  minutes from DPR scan time on 31-07-2021; the red check indicates the DPR reflectivity

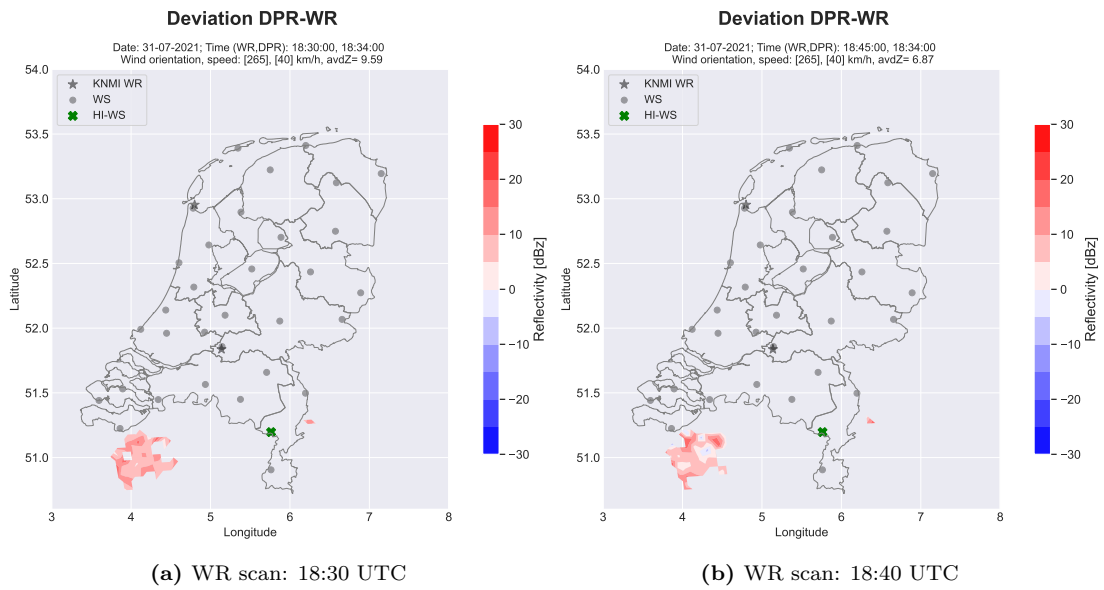


Figure B.56: Reflectivity deviation scans of DPR and WR scans on 31-07-2021

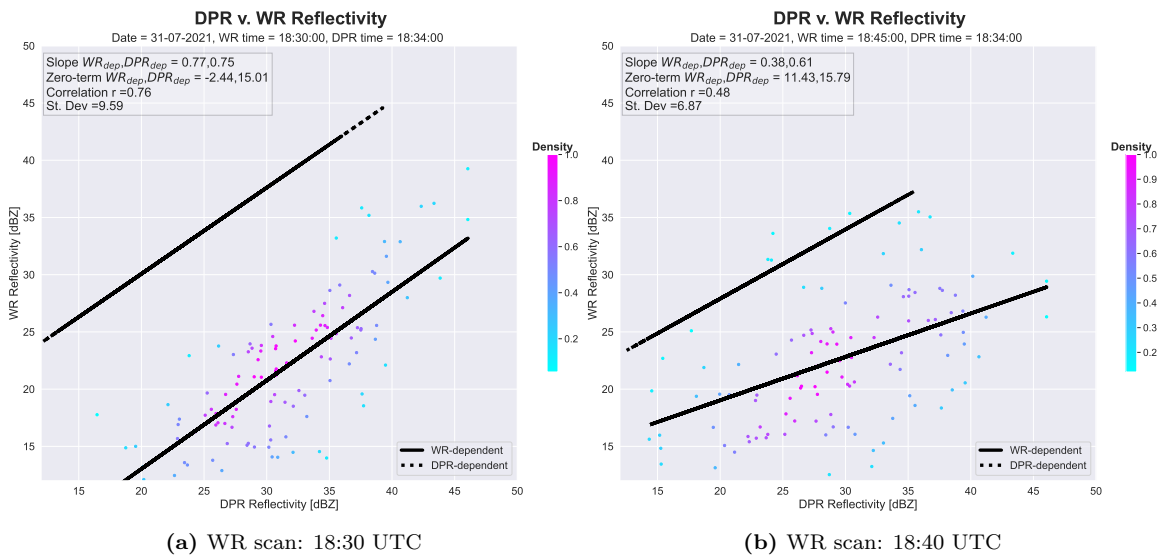


Figure B.57: Density scatter plots of  $Z_{DPR}$  and  $Z_{WR}$  on 31-07-2021



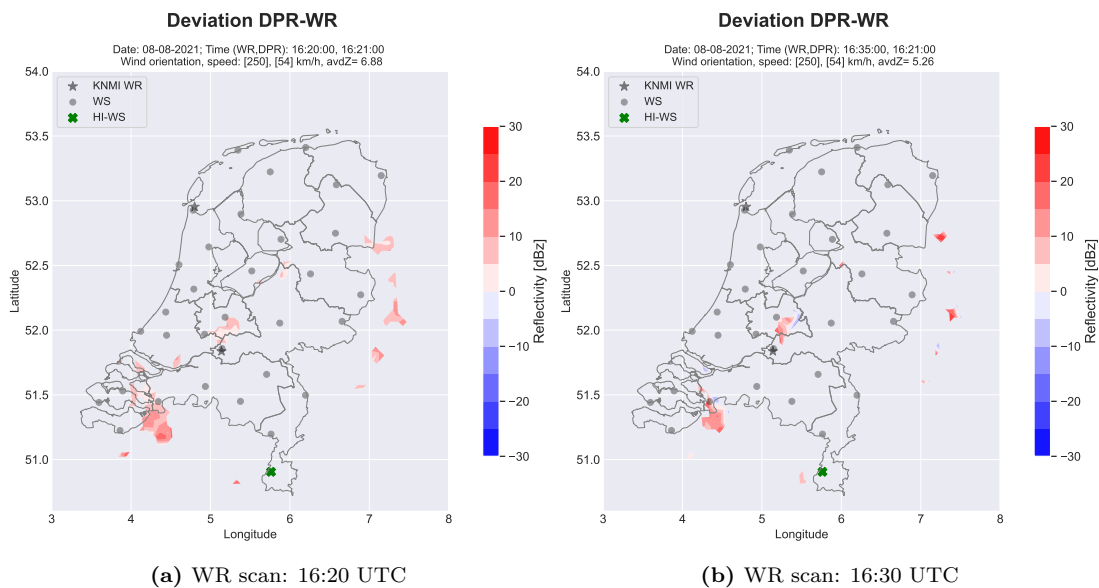


Figure B.60: Reflectivity deviation scans of DPR and WR scans on 31-07-2021

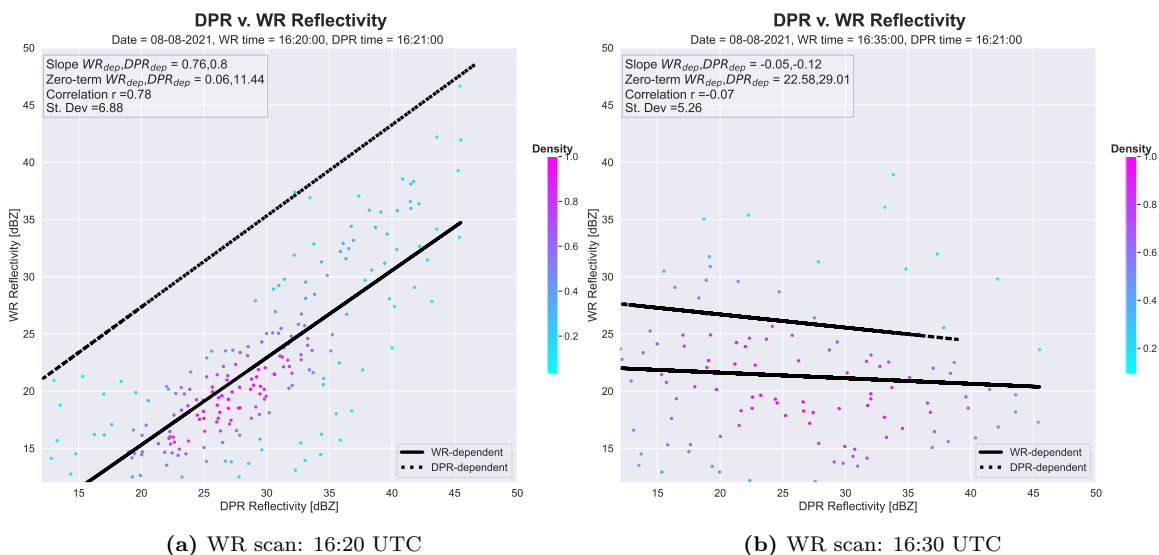
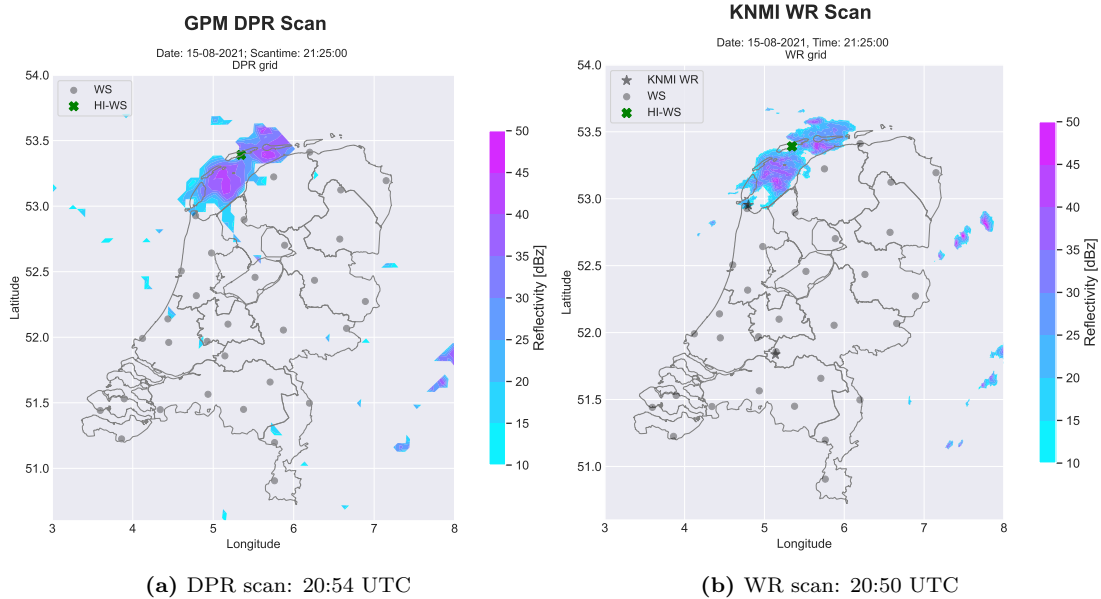


Figure B.61: Density scatter plots of  $Z_{DPR}$  and  $Z_{WR}$  on 31-07-2021

**Case Study P**

One station in the automatic network measured a precipitation intensity  $\geq 15$  mm/h within a range of  $\pm 40$  minutes from DPR scan time: *Hoorn Terschelling* recorded a peak intensity of 52.7 mm/h starting 35 minutes prior to DPR scan time. During scan time, the HI-WS recorded  $\pm 0$  mm/h. The HI-WS is overlapped by a moderate reflectivity zone (the edge of the HR-zone) in the DPR scan. At scantime, the storm has already taken place and, regarding the southwesterly wind, the HR-zone on the northeast side of the HI-WS can be assumed to relate to the HI-interval.



**Figure B.62:** DPR and WR scan for 09-08-2019

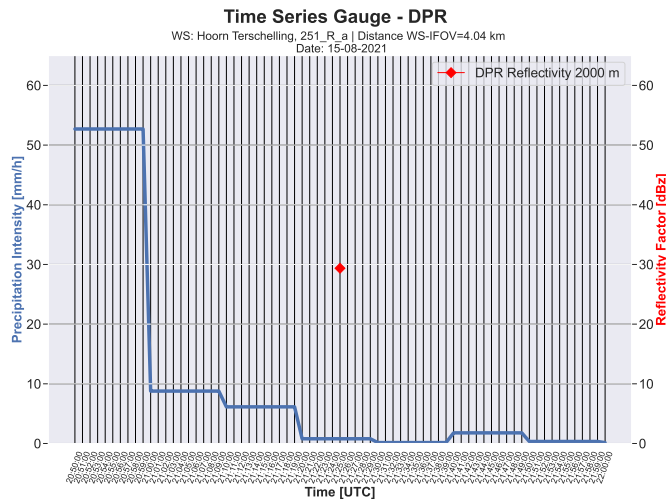


**Figure B.63:** Time series of HI-WS measurements within a range of  $\pm 40$  minutes from DPR scan time on 15-08-2021; the red check indicates the DPR reflectivity

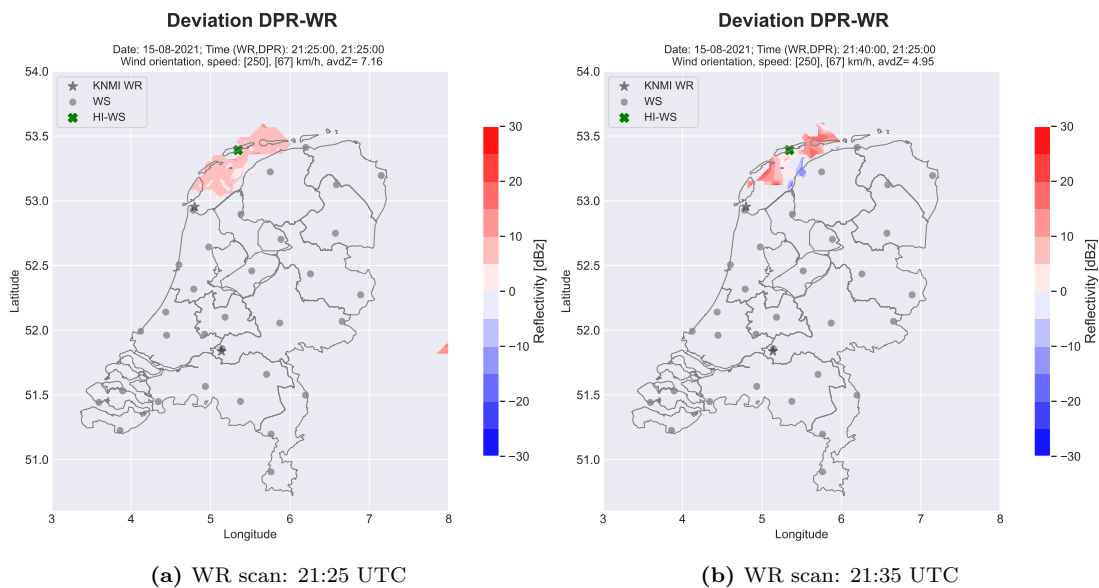


Figure B.64: Reflectivity deviation scans of DPR and WR scans on 09-08-2019

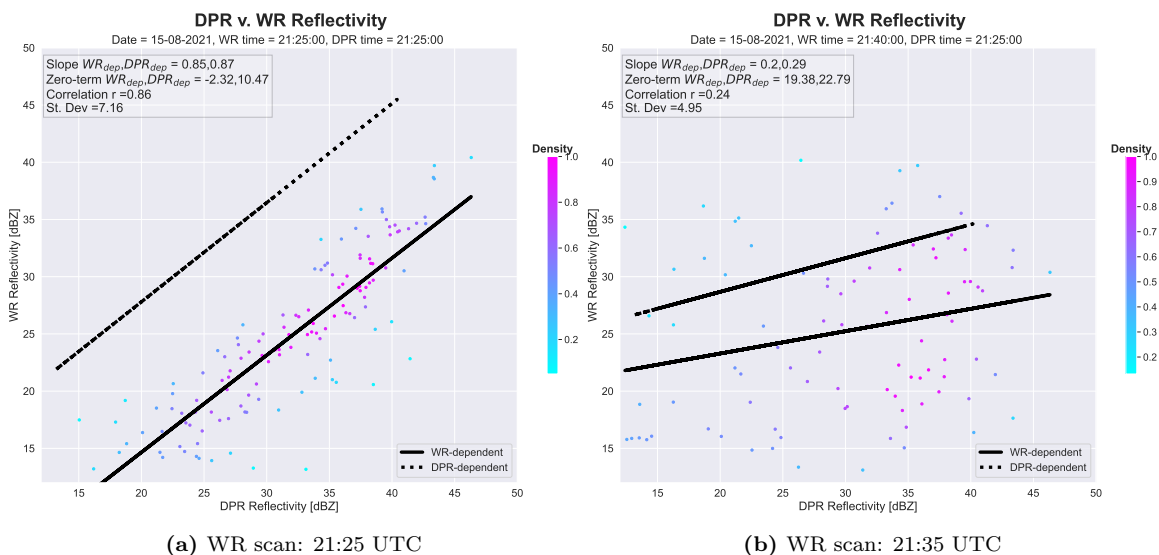
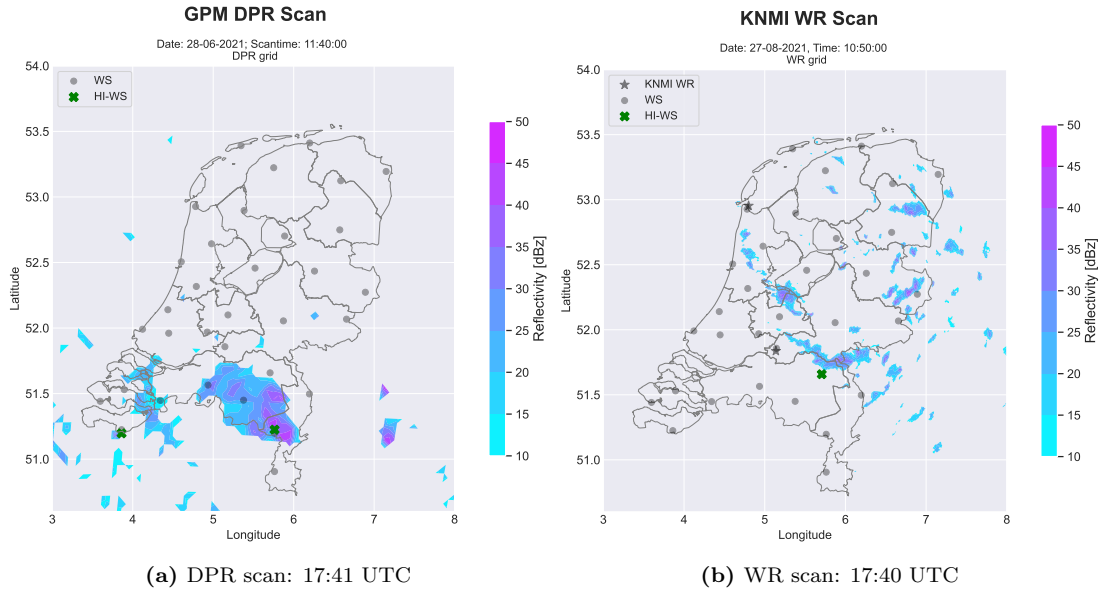


Figure B.65: Density scatter plots of  $Z_{DPR}$  and  $Z_{WR}$  on 09-08-2019

**Case Study Q**

*Volkel locatie A* observed an intensity of 18.1 mm/h 18 minutes after scan time. During scan time, no rainfall is observed. In both the DPR and WR scans, this is not situated in a HR zone. A HR zone is located north of the WS. Considering the observed northerly wind, that particular zone is assumed to relate to the observed HI-interval. The consecutive WR-scans support this assumption: at 11:05 UTC, the HR zone is located exactly over the HI-WS.



**Figure B.66:** DPR and WR scan for 27-08-2021

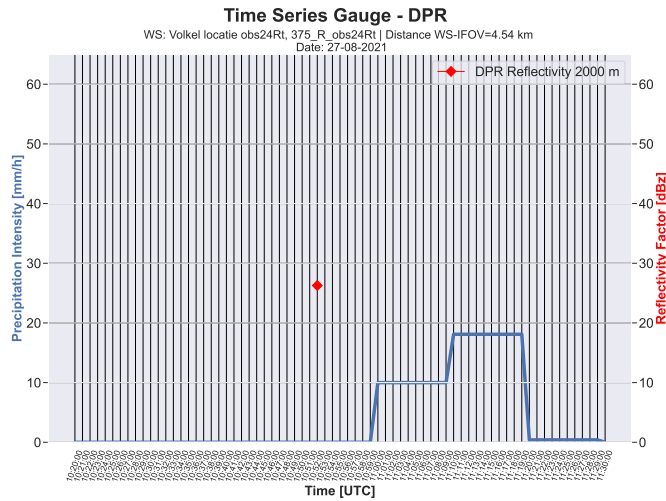


**Figure B.67:** Time series of HI-WS measurements within a range of  $\pm 40$  minutes from DPR scan time on 27-08-2021; the red check indicates the DPR reflectivity

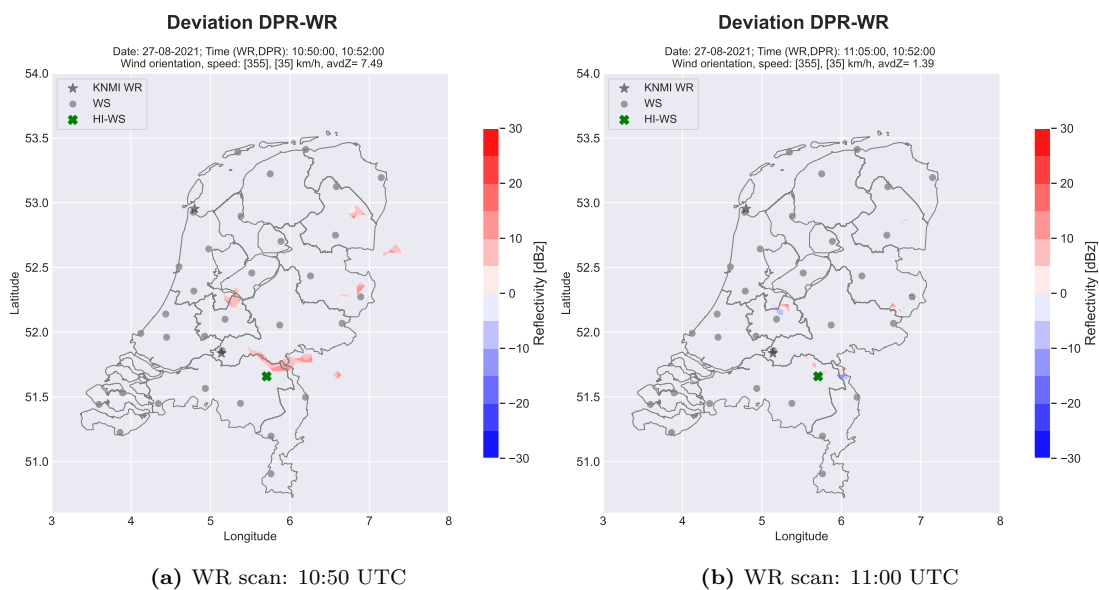


Figure B.68: Reflectivity deviation scans of DPR and WR scans on 27-08-2021

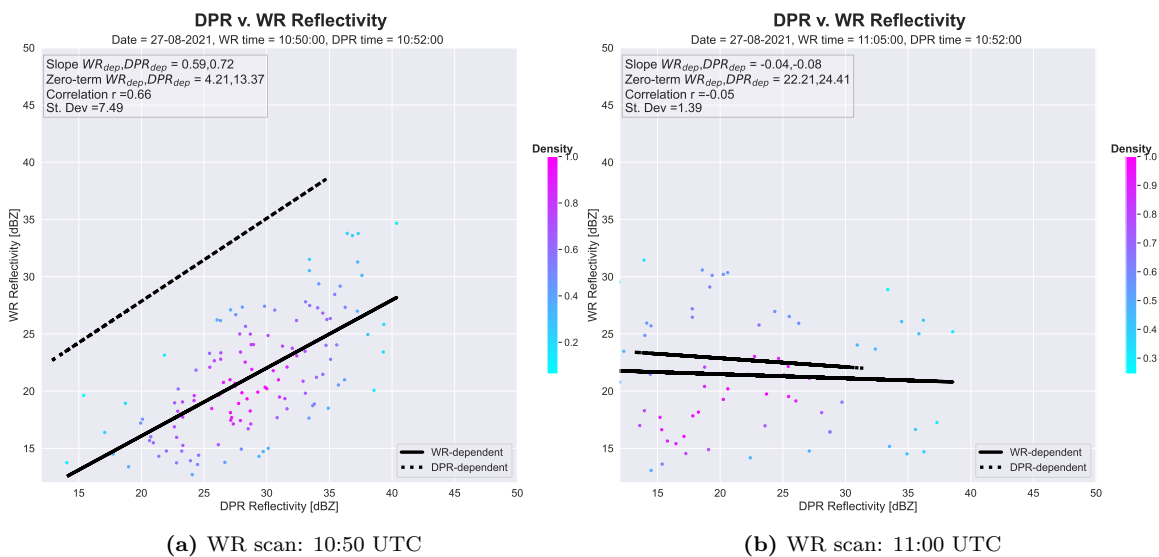


Figure B.69: Density scatter plots of  $Z_{DPR}$  and  $Z_{WR}$  on 27-08-2021

**Case Study R**

Two stations in the automatic network measured precipitation intensities  $\geq 15$  mm/h within a range of  $\pm 40$  minutes from DPR scan time: *Ell* recorded a peak intensity of 29.3 mm/h starting 26 minutes before DPR scan time and *Arcen* measured two HI intervals, with intensities of 17.8 mm/h 36 min before scan time and 16.2 mm/h 14 minutes after scan time, with 4 intervals of low-intensity precipitation in between the two peaks. During scan time, both stations measure low-intensity precipitation.

In both DPR and WR scans, *Arcen* is situated in an HR zone, with a large area expanding towards the northeast. At scan-time, one peak has already occurred and the next will start within the next 14 minutes. A westerly wind is measured at 2000 m altitude, so the first peak could be linked to the HR zone on the east side of *Arcen*. However, when observing the consecutive WR scans, the storm appears to move towards the northeast instead of the east. This corresponds to the wind data at 9000 m altitude, where a wind orientation of  $230^\circ$  is observed. The DPR algorithm found the storm height to range up to approximately 8800 meters. Therefore, the wind orientation at 9000 m can be assumed to still be of influence on the storm's direction and thus it can be assumed that the HR zone on the northeast of *Arcen* corresponds to the first HI-interval.

In both DPR and WR scans, *Ell* is situated in a LR zone. The DPR scan's width ends a few pixels east of *Ell*, causing the reflectivity data presumably relating to the HI-interval to not be visible. Considering the wind direction at 2000 m, one assumption is that that the HR zone that caused the HI-interval has moved towards the east and outside the DPR's scan width. However, when applying the former paragraph's theory relating the storm height to the wind direction, another assumption would be that the storm moved towards the northeast. Since both HI-WS are situated perpendicular to each other in the north-east direction, it could be assumed that the HR zone that passed over *Ell* subsequently moved over *Arcen*. Considering the time lag between the peak at *Ell* and the second peak occurring at *Arcen* (namely,  $\pm 30$  minutes), there is a possibility that the HR zone situated between the two stations in the GPM scan corresponds to both peaks.

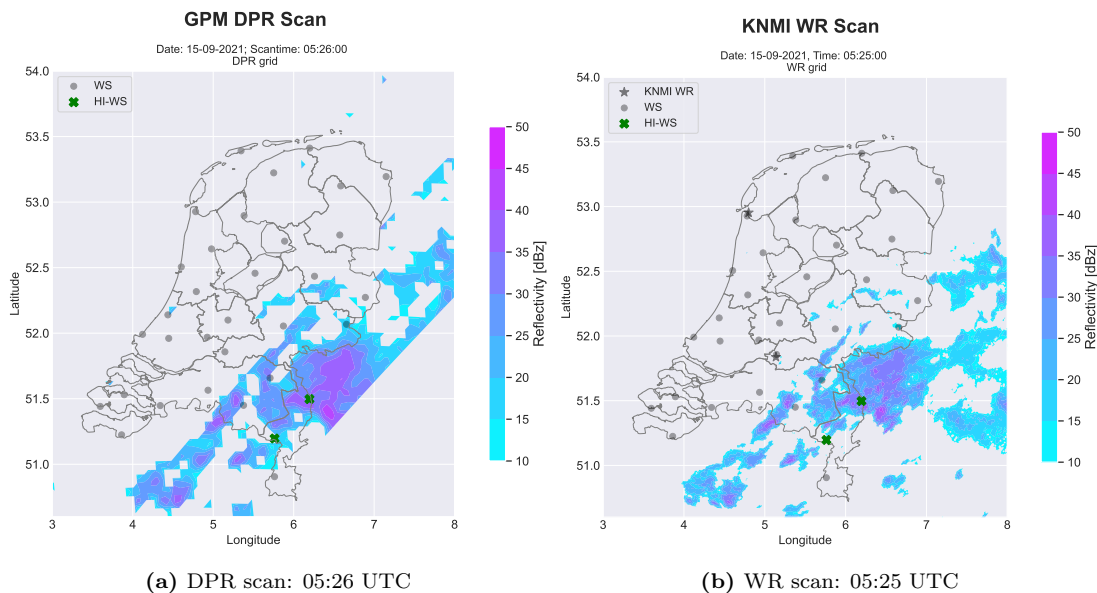
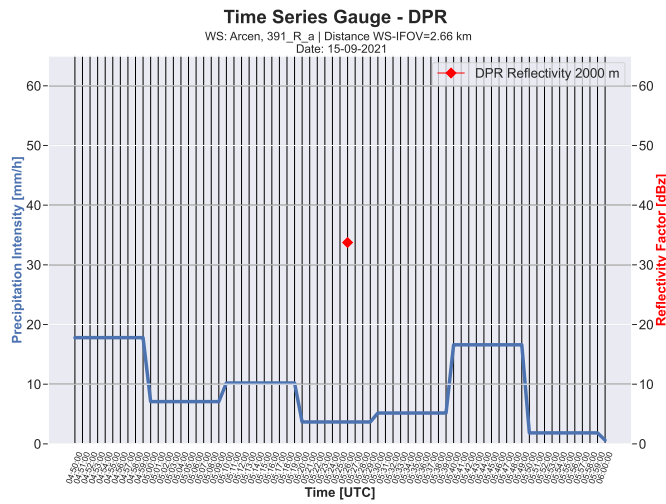
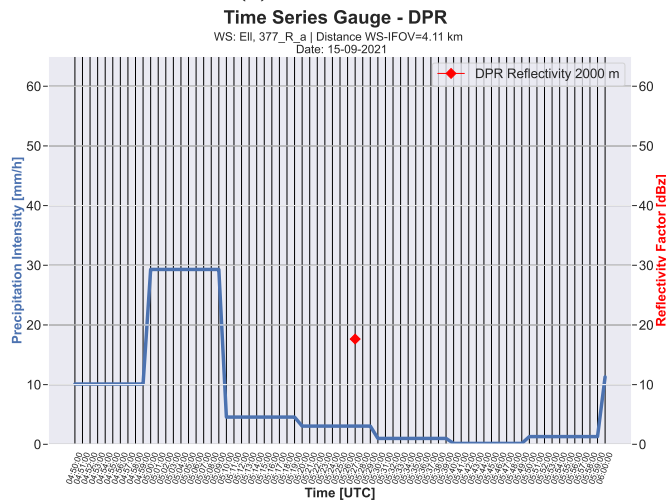


**Figure B.70:** DPR and WR scan for 15-09-2021



(a) Weather station:



(b) Weather station:

**Figure B.71:** Time series of HI-WS measurements within a range of  $\pm 40$  minutes from DPR scan time on 15-09-2021; the red check indicates the DPR reflectivity

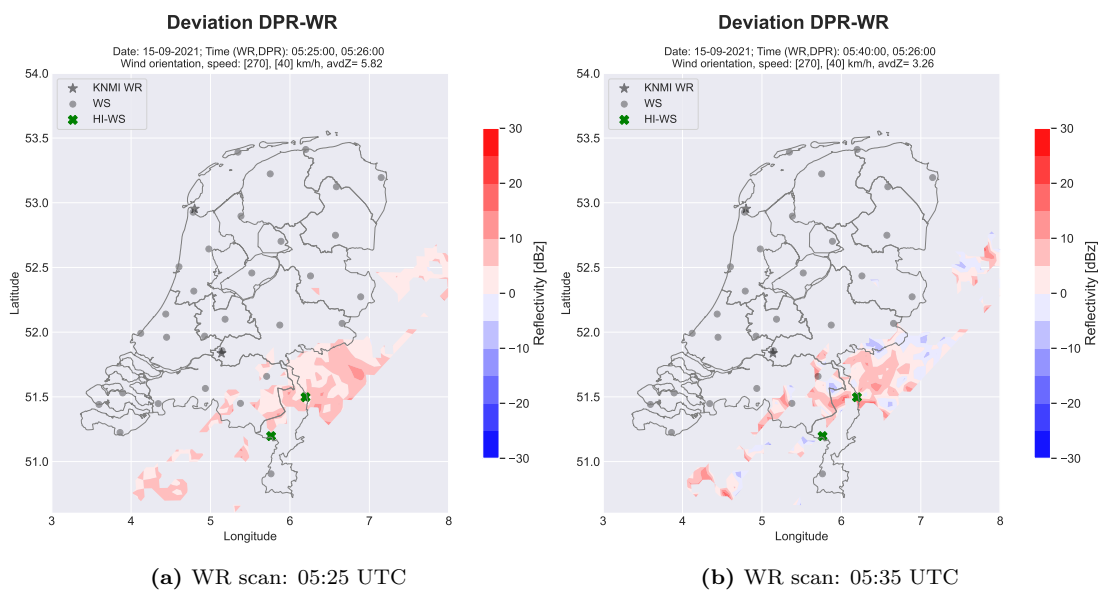


Figure B.72: Reflectivity deviation scans of DPR and WR scans on 15-09-2021

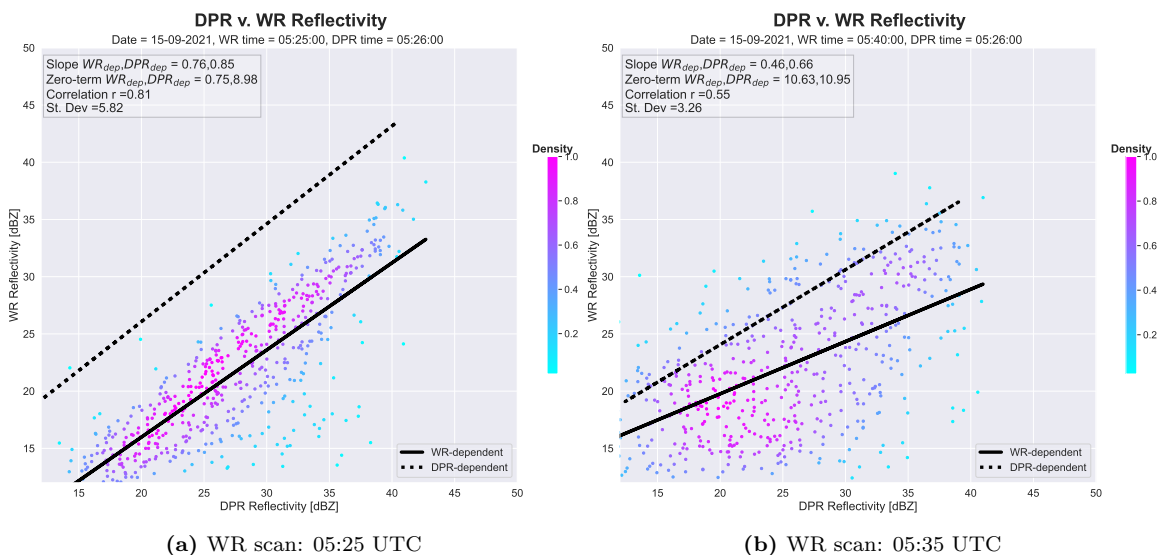
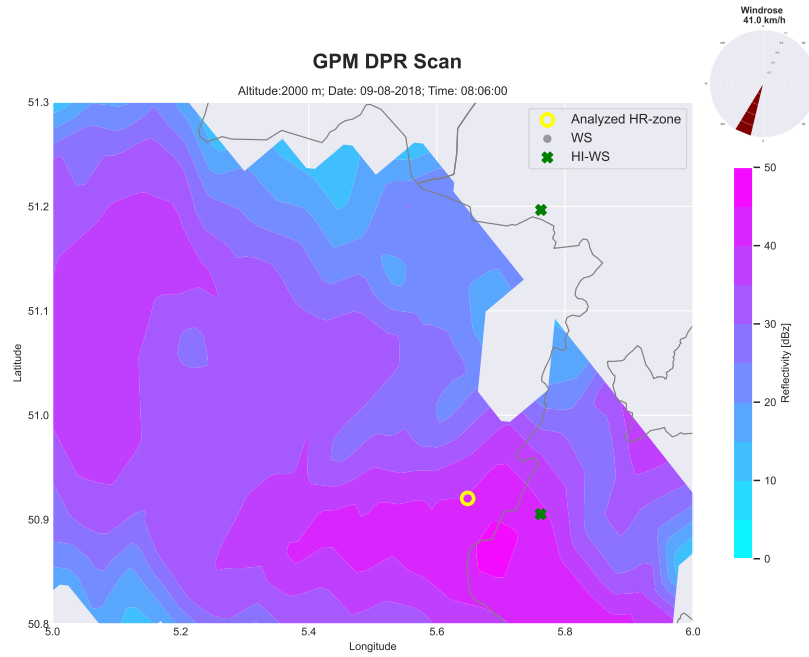


Figure B.73: Density scatter plots of  $Z_{DPR}$  and  $Z_{WR}$  on 15-09-2021

## C Figures Quantitative Analysis

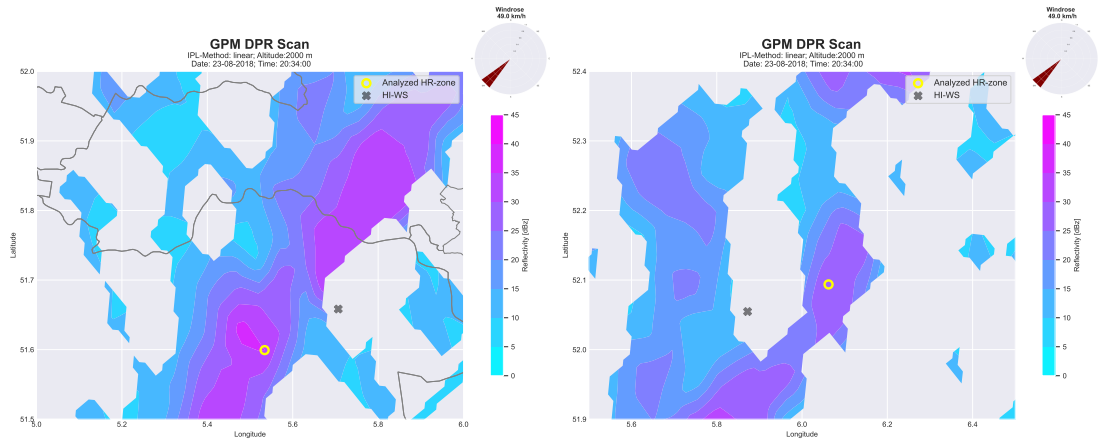
### Case Study A



(a) Weather station: Ell

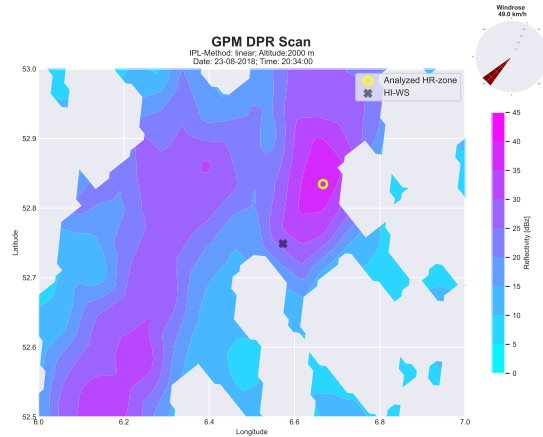
Figure C.1

Case Study B



(a) Weather station: Volkel locatie obs24Rt

(b) Weather station: Deelen locatie obs02t



(c) Weather station: Hoogeveen

Figure C.2

Case Study E

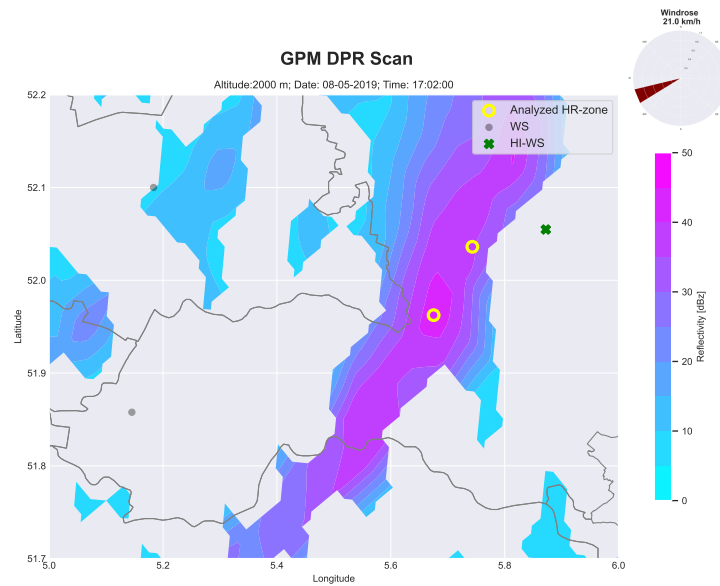


**Figure C.3:** DPR scan of 08-05-2019 20:34 UTC displaying measured reflectivity values at 2000 m. The yellow circles indicate the high reflectivity zones that are assumed to correspond to the high-intensity gauge intervals

Case Study I

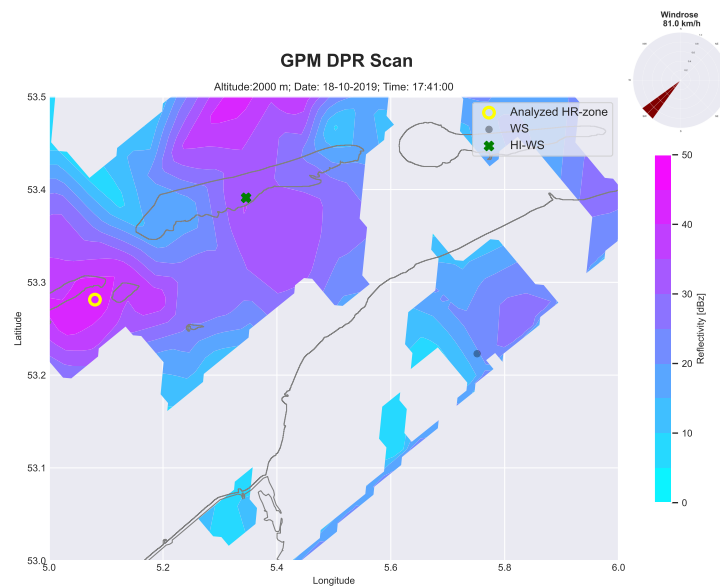


**Figure C.4:** DPR scan of 23-08-2018 20:34 UTC displaying measured reflectivity values at 2000 m. The yellow circles indicate the high reflectivity zones that are assumed to correspond to the high-intensity gauge intervals

Case Study J

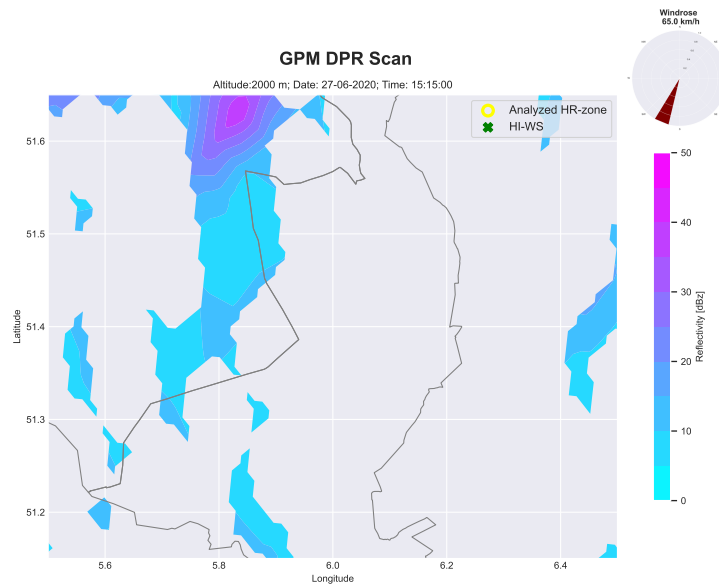


**Figure C.5:** DPR scan of 23-08-2018 20:34 UTC displaying measured reflectivity values at 2000 m. The yellow circles indicate the high reflectivity zones that are assumed to correspond to the high-intensity gauge intervals

Case Study N

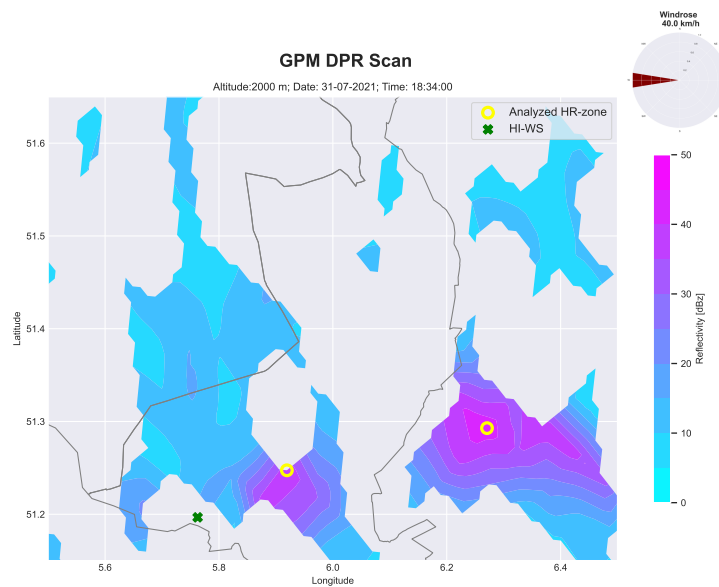


**Figure C.6:** DPR scan of 23-08-2018 20:34 UTC displaying measured reflectivity values at 2000 m. The yellow circles indicate the high reflectivity zones that are assumed to correspond to the high-intensity gauge intervals

Case Study O

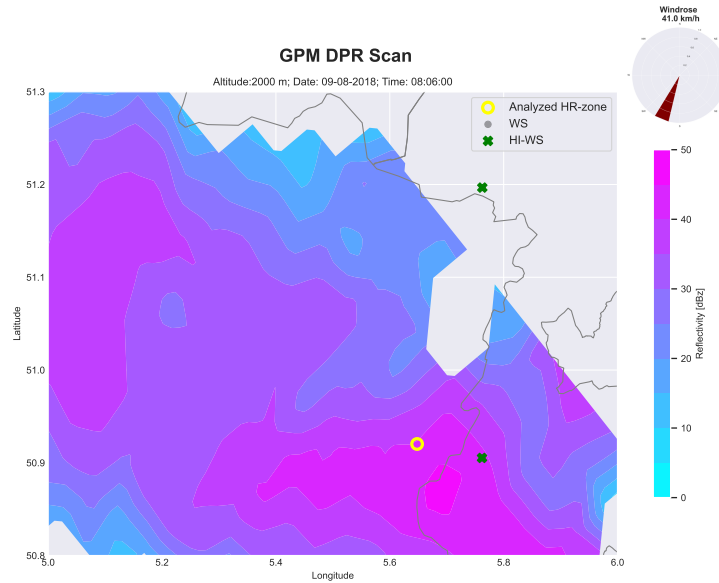


**Figure C.7:** DPR scan of 23-08-2018 20:34 UTC displaying measured reflectivity values at 2000 m. The yellow circles indicate the high reflectivity zones that are assumed to correspond to the high-intensity gauge intervals

Case Study P

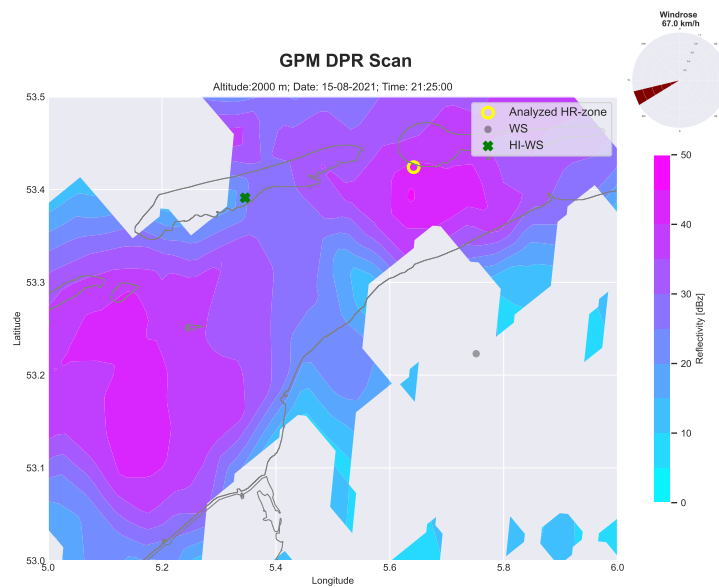


**Figure C.8:** DPR scan of 23-08-2018 20:34 UTC displaying measured reflectivity values at 2000 m. The yellow circles indicate the high reflectivity zones that are assumed to correspond to the high-intensity gauge intervals

Case Study Q

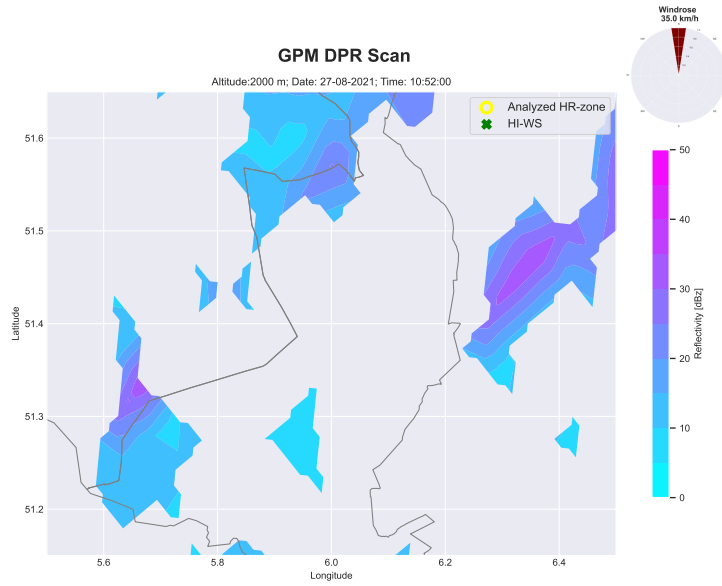
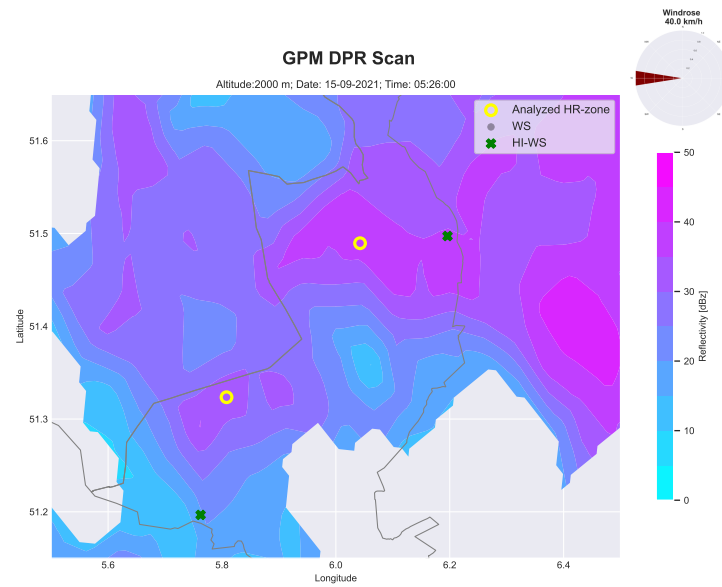


Figure C.9

Case Study R



(a) Weather station: Ell